

COMPACT NUCLEI IN GALAXIES AT MODERATE REDSHIFT

by

Vicki Lynn Sarajedini

A Dissertation Submitted to the Faculty of the

DEPARTMENT OF ASTRONOMY

In Partial Fulfillment of the Requirements

For the Degree of

DOCTOR OF PHILOSOPHY

In the Graduate College

THE UNIVERSITY OF ARIZONA

1 9 9 7

INFORMATION TO USERS

This manuscript has been reproduced from the microfilm master. UMI films the text directly from the original or copy submitted. Thus, some thesis and dissertation copies are in typewriter face, while others may be from any type of computer printer.

The quality of this reproduction is dependent upon the quality of the copy submitted. Broken or indistinct print, colored or poor quality illustrations and photographs, print bleedthrough, substandard margins, and improper alignment can adversely affect reproduction.

In the unlikely event that the author did not send UMI a complete manuscript and there are missing pages, these will be noted. Also, if unauthorized copyright material had to be removed, a note will indicate the deletion.

Oversize materials (e.g., maps, drawings, charts) are reproduced by sectioning the original, beginning at the upper left-hand corner and continuing from left to right in equal sections with small overlaps. Each original is also photographed in one exposure and is included in reduced form at the back of the book.

Photographs included in the original manuscript have been reproduced xerographically in this copy. Higher quality 6" x 9" black and white photographic prints are available for any photographs or illustrations appearing in this copy for an additional charge. Contact UMI directly to order.

UMI

**A Bell & Howell Information Company
300 North Zeeb Road, Ann Arbor MI 48106-1346 USA
313/761-4700 800/521-0600**

COMPACT NUCLEI IN GALAXIES AT MODERATE REDSHIFT

by

Vicki Lynn Sarajedini

A Dissertation Submitted to the Faculty of the

DEPARTMENT OF ASTRONOMY

In Partial Fulfillment of the Requirements

For the Degree of

DOCTOR OF PHILOSOPHY

In the Graduate College

THE UNIVERSITY OF ARIZONA

1 9 9 7

UMI Number: 9806791

UMI Microform 9806791
Copyright 1997, by UMI Company. All rights reserved.

**This microform edition is protected against unauthorized
copying under Title 17, United States Code.**

UMI
300 North Zeeb Road
Ann Arbor, MI 48103

THE UNIVERSITY OF ARIZONA ©
GRADUATE COLLEGE

As members of the Final Examination Committee, we certify that we have
read the dissertation prepared by Vicki Lynn Sarajedini
entitled Compact Nuclei in Galaxies at Moderate Redshift

and recommend that it be accepted as fulfilling the dissertation
requirement for the Degree of Doctor of Philosophy

Richard Green

Dr. Richard Green

Marcia Rieke

Dr. Marcia Rieke

George Rieke

Dr. George Rieke

Jill Bechtold

Dr. Jill Bechtold

7/18/97

Date

7/18/97

Date

7/18/97

Date

7/18/97

Date

Date

Final approval and acceptance of this dissertation is contingent upon
the candidate's submission of the final copy of the dissertation to the
Graduate College.

I hereby certify that I have read this dissertation prepared under my
direction and recommend that it be accepted as fulfilling the dissertation
requirement.

Richard Green

Dissertation Director

Dr. Richard Green

8/11/97

Date

STATEMENT BY AUTHOR

This dissertation has been submitted in partial fulfillment of requirements for an advanced degree at The University of Arizona and is deposited in the University Library to be made available to borrowers under rules of the Library.

Brief quotations from this dissertation are allowable without special permission, provided that accurate acknowledgment of source is made. Requests for permission for extended quotation from or reproduction of this manuscript in whole or in part may be granted by the head of the major department or the Dean of the Graduate College when in his or her judgment the proposed use of the material is in the interests of scholarship. In all other instances, however, permission must be obtained from the author.

SIGNED: Vicki Lynn Seigedun

ACKNOWLEDGMENTS

I would like to acknowledge the immense support and scientific guidance of my advisor Richard Green. Richard's enthusiasm for astronomy has been an inspiration to me and his insight has broadened my interests in the field. His support of my research has made this thesis possible.

I would like to thank and acknowledge several people associated with the Medium Deep Survey Key Project. Richard Griffiths made it possible for me to take part in this exciting endeavor with the Hubble Space Telescope. He provided continual support for my research within the Medium Deep Survey. I would like to thank Kavan Ratnatunga for his unending help and patience while teaching me about his software and allowing me to use and alter it for the purposes of this project. I would also like to thank Eric Ostrander who provided me with the processed HST images through the MDS pipeline and aided me in the selection of MDS fields for this project.

Finally, there are several other people I would like to thank who provided me with information or data which was extremely important to this dissertation. Caryl Gronwall allowed me to use her software to estimate K-corrections for the galaxies in my survey. Yichen Pei provided me with his QSO luminosity function models and model fitting software. Judy Cohen provided me with the redshift list from her study of the Hubble Deep Field. I am grateful to these people for their valuable help. I would also like to thank Ata Sarajedini and Joe Shields for many helpful conversations concerning the analysis of this data.

DEDICATION

This dissertation is dedicated to my husband, Ata Sarajedini, who gave me constant support and encouragement as I pursued my degree.

“I can do all things through Him who gives me strength” - Phillipians 4:13

TABLE OF CONTENTS

LIST OF FIGURES	8
LIST OF TABLES	14
ABSTRACT	15
1 INTRODUCTION	17
2 Hubble Space Telescope Images: Reduction and Galaxy Modeling	23
2.1 Fields Selected from the Survey	23
2.2 Reduction of HST WFPC2 images	24
2.3 Galaxy Fitting Software	26
2.4 Selection of Galaxies Containing Nuclear Point Sources	30
2.4.1 Spurious Point Source Detections in Simulated Galaxies	31
2.4.2 Measurement of Detected Point Source Nuclei	32
2.5 Accuracy of the Host Galaxy Bulge Measurements	41
2.6 Completeness	45
2.7 Application to the Survey Data	48
2.7.1 Determining the Limiting SNRIL value	48
2.7.2 Selected Galaxies Containing Nuclear Point Sources	52
3 Spectroscopy and Redshifts	72
3.1 Spectroscopy and Data Reduction	73
3.2 Redshift Determination	75
3.3 Spectroscopic Identifications for Nuclear Point Source Galaxies	96
3.4 Photometric Redshifts	97
4 Compact Nuclei Galaxies: Host Galaxies and Nuclear Colors	114
4.1 Properties of The Host Galaxies	114

Table of Contents — *Continued*

4.1.1	Host Galaxy Types	114
4.1.2	Comparison with Other Survey Galaxies	122
4.1.3	Host Galaxy Absolute Magnitudes	129
4.2	The Colors of the Point Source Nuclei: Clues to Their Nature	131
4.3	Synthetic V-I colors for AGN and Star Clusters: Comparison with the Nuclear Colors	136
5	The Number Density and Luminosity Function for Unresolved Nuclei . . .	148
5.1	The Upper Limit Luminosity Function for LLAGN	151
5.1.1	LF Calculation	151
5.1.2	Comparison with the Local Luminosity Function for Seyferts .	155
5.1.3	Comparison with QSO Luminosity Functions	162
5.2	The Number of LLAGN in Local Spiral Galaxies	168
5.3	Implications For the X-Ray Source Surface Density	169
6	CONCLUSIONS	175
6.1	Summary of Results	175
6.2	Future Work	179
	REFERENCES	182

LIST OF FIGURES

1.1	The diameter of an unresolved region in a WFPC2 image as a function of the object's redshift. The lines represent values of $H_0 = 50, 75$, and 100 km/s/Mpc	20
2.1	Output from the 2-dimensional modeling software. From left to right the boxes are: 1) the observed 64×64 pixel area around the galaxy, 2) the selected region for analysis, 3) the PSF convolved maximum likelihood model image, 4) the maximum likelihood model image, 5) the residual image (model subtracted from real image), 6) the sigma image, 7) the object mask image.	29
2.2	Fitting parameters for spurious point source detections in simulated galaxies. The likelihood ratio represents the degree to which the model with a point source component is better than the model without a point source component in fitting the simulated galaxies. .	33
2.3	Histogram of the number of spurious point source detections as a function of the point source-to-total luminosity ratio.	34
2.4	Fitting parameters for spurious point source detections in simulated galaxies. All point source detections less than 1% of the total galaxy light have been removed	35
2.5	Parameters of galaxies used in the Monte-Carlo simulation. The galaxies cover a range of Bulge-to-Total luminosity ratios, magnitudes and SNRIL values. SNRIL is the integrated signal-to-noise measurement described in the text.	37
2.6	The input vs. the measured magnitude for the point source nuclei detected in the Monte-Carlo simulation.	39
2.7	The input vs. the measured magnitude for the point source nuclei detected in the Monte-Carlo simulation after applying the selection criteria outlined in the text.	42
2.8	a) The histogram of $\text{mag}_{\text{obs}} - \text{mag}_{\text{real}}$ for point sources at 23 ± 0.25 . The dotted line represents the gaussian curve with $\sigma = 0.26$. b) Same histogram for point sources at 24 ± 0.25 magnitudes. The gaussian represents $\sigma = 0.56$	43

List of Figures — *Continued*

- 2.9 a) The Bulge-to-Bulge+Disk measured in galaxies within which point source nuclei were detected in the simulations vs. the input Bulge-to-Bulge+Disk for the host galaxy. b) The measured Bulge-to-Bulge+Disk as a function of the point source-to-total luminosity ratio for galaxies in the simulations in which point source nuclei were detected. 44
- 2.10 a) The histogram of galaxies in the simulation containing no bulge component as a function of the point source-to-total luminosity ratio. The solid line represents all galaxies in the simulation with no bulge component and the hatched region represents those galaxies in which the nuclear point source was detected. b) The fractional completeness or success rate in detecting point source nuclei in galaxies containing no bulge component. The errorbars are the Poisson statistics based on the number of objects in each bin. 47
- 2.11 a) The histogram of galaxies in the simulation containing bulge components with $0 < (B/B+D) \leq 0.4$ as a function of the point source-to-total luminosity ratio. The hatched region represents those in which the point source nucleus was detected. The panel to the right is the fractional completeness or success rate in detecting point source nuclei for these galaxies. b) Same as above except for galaxies with $0.4 < (B/B+D) \leq 0.8$. c) Same as above except for galaxies with $0.8 < (B/B+D) \leq 1.0$ 49
- 2.12 a) The histogram of all galaxies in the simulation containing no bulge component as a function of the SNR_{IL} value. The hatched region represents those galaxies where a 2-component point source+disk model was the best fit thereby detecting the point source nucleus. b) The histogram of all galaxies in the simulation containing some bulge component as a function of the SNR_{IL} value. The hatched region represents those galaxies where a 2-component point source+disk model or a 3-component point source+disk+bulge model was the best fit. The cross-hatched region represents those galaxies where the 3-component model was the best fit. 51
- 2.13 I band image of galaxies containing unresolved nuclear point sources down to 1% of the total galaxies light. The galaxies are arranged in descending order from the greatest point source-to-total luminosity ratio from left to right, top to bottom. The ID number is used to indentify each object throughout the paper. 55

List of Figures — *Continued*

- 2.14 The point source nucleus magnitude vs. the integrated galaxy magnitude in a) I and b) V. The dashed line represents the locus where the point source is 1% of the total galaxy light. 58
- 2.15 The overall completeness estimate for detecting nuclei in the survey galaxies as a function of the point source-to-total luminosity ratio. . . 60
- 2.16 a) The fraction of total survey galaxies containing unresolved nuclei as a function of the limiting point source-to-total luminosity ratio. The dashed line represents this fraction after correcting for completeness according to Figure 2.15. b) The completeness adjustment factor as a function of the limiting point source-to-total luminosity ratio. This is the amount by which the fraction must be multiplied to correct for incompleteness. 62
- 3.1 Spectra of galaxies containing compact nuclei obtained at the Kitt Peak 4-meter telescope. The spectra are not flux calibrated and are in units of flux (electrons) vs. wavelength (angstroms). Prominent emission and absorption features are indicated. The object name and redshift is in the upper left corner and an ID number corresponding to the ID number for the galaxy image in Figure 2.13 is in the upper right corner. The dashed line is the arbitrarily scaled error spectrum. 78
- 3.2 a) The I magnitude for galaxies in our survey vs. the measured redshift. b) The V-I color vs. the redshift. c) The Bulge/Total luminosity ratio vs. the redshift. 99
- 3.3 a) The I magnitude for galaxies in our survey with Bulge/Total ≤ 0.2 vs. the measured redshift. b) The V-I color vs. the redshift. c) The estimated redshift based on fits to the color and magnitude vs. the true redshift. d) The residual of the fit ($z_{\text{measured}} - z_{\text{est}}$) vs. the measured redshift. The standard deviation of the fit is indicated. . . . 101
- 3.4 a) The I magnitude for galaxies in our survey with Bulge/Total ≤ 0.5 vs. the measured redshift. b) The V-I color vs. the redshift. c) The estimated redshift based on fits to the color and magnitude vs. the true redshift. d) The residual of the fit ($z_{\text{measured}} - z_{\text{est}}$) vs. the measured redshift. The standard deviation of the fit is indicated. . . . 102

List of Figures — *Continued*

- 3.5 a) The I magnitude for galaxies in our survey with Bulge/Total>0.5 vs. the measured redshift. b) The V-I color vs. the redshift. c) The estimated redshift based on fits to the color and magnitude vs. the true redshift. d) The residual of the fit ($z_{\text{measured}} - z_{\text{est}}$) vs. the measured redshift. The standard deviation of the fit is indicated. . . . 103
- 3.6 a) The I magnitude for galaxies in our survey with Bulge/Total>0.8 vs. the measured redshift. b) The V-I color vs. the redshift. c) The estimated redshift based on fits to the color and magnitude vs. the true redshift. d) The residual of the fit ($z_{\text{measured}} - z_{\text{est}}$) vs. the measured redshift. The standard deviation of the fit is indicated. . . . 104
- 3.7 The photometric redshift vs. their measured spectroscopic redshift for those galaxies used in the empirical fit. 105
- 3.8 The histogram of redshifts for the compact nuclei galaxies. The hatched region represents those galaxies where the redshift was determined spectroscopically. 108
- 4.1 The fraction of galaxies in the Monte-Carlo simulation where the measured Bulge/Total is zero as a function of the input Bulge/Total for the galaxy. The errorbars are the Poisson statistics based on the number of galaxies in each bin. 116
- 4.2 The distribution of Bulge/Bulge+Disk measurements for galaxies containing compact nuclei. The solid line is the actual number distribution. The two dashed lines represent two extremes of the distribution after statistically correcting for bulge misclassification as described in the text. 119
- 4.3 Histogram of measured Bulge/Total values for the 1033 galaxies in our survey (hatched region) normalized to 1=500. The dotted line represents the total fraction of galaxies in each Bulge/Total bin. . . . 123
- 4.4 a) The galaxy I magnitude vs. the natural log of the half-light radius of the galaxy for all survey galaxies (open circles) and those galaxies containing compact nuclei (filled circles). b) The normalized distribution of half-light radii for all survey galaxies (solid line) and those containing compact nuclei (hatched region). 125
- 4.5 Histogram of the axis ratios for galaxies containing compact nuclei. The histogram is normalized by the dividing by the axis ratio histogram for all spiral survey galaxies. 127

List of Figures — *Continued*

- 4.6 a) The color-magnitude diagram for galaxies in our survey where open circles represent non-host galaxies and filled circles represent those galaxies hosting a compact nucleus. b) The normalized histogram of galaxy V-I colors for the host galaxies (hatched region) compared with the normalized histogram of galaxy colors for a representative group of non-host galaxies of similar morphological type (solid line) . 130
- 4.7 a) Histogram of rest-frame B absolute magnitudes for the host galaxies in our sample. b) Absolute B magnitudes from Ho et al. (1997a) of dwarf Seyfert nuclei hosts. c) Absolute B magnitudes from Ho et al. (1997b) of HII nuclei hosts. 132
- 4.8 a) The point source V-I color vs. the host galaxies V-I color. Points measured in only one filter are shown as color limits. b) The generalized histogram of the color difference between the host galaxy and the point source. 140
- 4.9 a) The point source V-I color vs. the bulge V-I color for the 17 galaxies containing a measureable bulge and point source color. b) The generalized histogram of the color difference between the bulge and the point source nucleus. 141
- 4.10 The redshift vs. the V-I color of the unresolved nuclei. The open circles are those nuclei with color limits. 142
- 4.11 a) Seyfert 1 spectrum produced by averaging several reliably classified Seyfert 1 galaxies (Kalinkov et al. 1993). b) Seyfert 1.5 galaxy spectrum. c) Seyfert 2 galaxy spectrum. 143
- 4.12 a) HII nucleus. b) age \simeq 10 Myr star cluster with $[Z/Z_{\odot}]\simeq$ -0.25. c) age \simeq 25 Myr star cluster with $[Z/Z_{\odot}]\simeq$ -0.4. d) age \simeq 80 Myr star cluster with $[Z/Z_{\odot}]\simeq$ -0.5. e) age \simeq 200-500 Myr star cluster with $[Z/Z_{\odot}]\simeq$ -0.6. f) age \simeq 1-2 Gyr star cluster with $[Z/Z_{\odot}]\simeq$ -0.5. All spectra are from E. Bica in Leitherer et al. (1996). 144
- 4.13 V-I colors for the 3 types of Seyfert galaxies as a function of redshift. The solid line is the Seyfert 2 color, the short dashed line is the Seyfert 1.5 and the long dashed line is the Seyfert 1. 146

List of Figures — *Continued*

- 4.14 V-I colors for the various star cluster spectra shown in Figure 4.12 as a function of redshift. The solid line is the integrated HII region color, the short dashed line is the 10 Myr cluster, the long dashed line is the 25 Myr cluster, the dot-short dashed line is the 80 Myr cluster, the dot-long dashed line is the 200-500 Myr cluster, and the dotted line is the 1-2 Gyr cluster. 147
- 5.1 Distribution of weights as a function of σ_z for galaxies with photometrically determined redshifts. Each galaxy is treated as a distribution centered on its estimated redshift but distributed over $\pm 3\sigma$ 154
- 5.2 The luminosity function of compact nuclei $\geq 3\%$ of the total galaxy light. The solid line represents the LF for nuclei at $0 < z \leq 0.4$ and the dashed line is the LF at $0.4 < z \leq 0.8$. The dot-dashed line is the LF for Seyfert galaxies from the CfA redshift survey (Huchra & Burg 1992). Here we have assumed $H_0 = 100 \text{ km s}^{-1} \text{ Mpc}^{-1}$, $q_0 = 0.5$ and $\alpha = -1.0$. . 156
- 5.3 The bulge diameter in parsecs based on the bulge half-light radius for spiral galaxies in our survey with spectroscopic redshifts (filled circles) and photometric redshifts (open circles). The solid line is the resolving limit of HST assuming $H_0 = 75 \text{ km/s/Mpc}$ 161
- 5.4 The luminosity function of compact nuclei $\geq 3\%$ of the total galaxy light. The solid line represents nuclei at $0 < z \leq 0.4$ and the dashed line is for $0.4 < z \leq 0.8$. At higher luminosities we show the LF for QSO's from the compilation by Hartwick and Schade (1990) for $0.16 < z \leq 0.4$ (solid line at $M_B \leq -22$) and $0.4 < z \leq 0.7$ (dashed line at $M_B \leq -22$). Here we have assumed $H_0 = 50 \text{ km s}^{-1} \text{ Mpc}^{-1}$, $q_0 = 0.5$ and $\alpha = -0.5$ 163
- 5.5 a) The double power-law model fitted to the bright quasar LFs (dotted line) using parameters from Pei (1995). b) The same model fitted to both the bright LF and the faint LF (this data). We assume $H_0 = 50 \text{ km s}^{-1} \text{ Mpc}^{-1}$, $q_0 = 0.5$ and $\alpha = -0.5$ 165

LIST OF TABLES

2.1	MDS Fields	64
2.1	MDS Fields	65
2.1	MDS Fields	66
2.2	Field Limiting Magnitude	67
2.2	Field Limiting Magnitude	68
2.2	Field Limiting Magnitude	69
2.3	Model Parameters for Galaxies Containing Unresolved Nuclei	70
2.3	Model Parameters for Galaxies Containing Unresolved Nuclei	71
2.3	Model Parameters for Galaxies Containing Unresolved Nuclei	72
3.1	Spectroscopic Observing Run Summary	75
3.2	Redshift Estimation Coefficients	106
3.3	Redshift List	110
3.3	Redshift List	111
3.3	Redshift List	112
3.3	Redshift List	113
3.3	Redshift List	114
5.1	Luminosity Functions ($H_o=100$, $q_o=0.5$ and $\alpha=-1.0$)	174
5.2	Luminosity Functions ($H_o=50$, $q_o=0.5$ and $\alpha=-0.5$)	175

ABSTRACT

The purpose of this study is to understand the space density and properties of active galaxies to $z \simeq 0.8$. We have investigated the frequency and nature of unresolved nuclei in galaxies at moderate redshift as indicators of nuclear activity such as Active Galactic Nuclei (AGN) or starbursts. Candidates are selected by fitting imaged galaxies with multi-component models using maximum likelihood estimate techniques to determine the best model fit. We select those galaxies requiring an unresolved, point source component in the galaxy nucleus, in addition to a disk and/or bulge component, to adequately model the galaxy light.

We have searched 70 WFPC2 images primarily from the Medium Deep Survey for galaxies containing compact nuclei. In our survey of 1033 galaxies, the fraction containing an unresolved nuclear component $\geq 3\%$ of the total galaxy light is $16 \pm 3\%$ corrected for incompleteness and $9 \pm 1\%$ for nuclei $\geq 5\%$ of the galaxy light. Most of the nuclei are $\lesssim 20\%$ of the total galaxy light. The majority of the host galaxies are spirals with little or no bulge component. The V-I colors of the nuclei are compared with synthetic colors for Seyferts and starburst nuclei to help differentiate between AGNs and starbursts in our sample. Spectroscopic redshifts have been obtained for 35 of our AGN/starburst candidates and photometric redshifts are estimated to an accuracy of $\sigma_z \simeq 0.1$ for the remaining sample.

We present the upper limit luminosity function (LF) for low-luminosity AGN (LLAGN) in two redshift bins to $z=0.8$. We detect mild number density evolution of the form $\phi \propto (1+z)^{1.9}$ for nuclei at $-18 \lesssim M_B \lesssim -14$. The LFs appear to flatten at $M_B \geq -16$ and this flatness, combined with the increase in number density, is inconsistent with pure luminosity evolution. Based on the amount of density

evolution observed for these objects, we find that almost all present-day spiral galaxies could have hosted a LLAGN at some point in their lives. We estimate the likely contribution of these compact nuclei to the soft X-ray background to be as much as $\sim 15\%$ or all of the X-ray background depending on assumptions about their X-ray nature.

CHAPTER 1

INTRODUCTION

Accurate knowledge of the luminosity function (LF) of active galactic nuclei over a wide range of absolute magnitudes is necessary to understand the nature and evolution of these objects. The faint end of the AGN LF ($M_B \geq -23$) has been determined using Seyfert galaxy nuclei which are considered to be the intrinsically fainter counterparts of more distant, brighter AGNs (Cheng et al. 1985; Huchra & Burg 1992). It is difficult, however, to obtain a Seyfert sample which is free from biases. Seyferts selected by UV or X-ray excess are likely to favor type 1 nuclei. Selection based on IR properties are biased toward galaxies with high star formation rates. The Huchra & Burg (1992) Seyfert sample from the CfA redshift survey was obtained through spectroscopic selection of galaxies based on the presence of broad emission lines, indicative of Seyfert 1 activity, or emission line flux ratios indicating Seyfert 2 or LINER activity. The presence of such emission lines differentiates between a thermal and non-thermal energy source in the nucleus. This selection technique, however, requires that the nucleus dominate the galaxy light or have adequate spatial resolution for subtraction of the galaxy light from the nucleus. Maiolino & Rieke (1995) show that the CfA Seyfert nuclei

luminosities are closely related to the integrated galaxy luminosities indicating a bias towards brighter, nucleus-dominated Seyferts. For this reason, the local AGN LF does not extend below $M_B \simeq -17.5$.

Even more interesting is the behavior of the LF as a function of redshift enabling us to derive the manner in which AGNs evolve. Understanding how the faint end of the AGN LF evolves is necessary to determine the frequency and total space density of these objects at earlier epochs. There are several models for quasar evolution which can be much better constrained with accurate knowledge of the shape at the faint end. Koo (1986) explains how many of the models are difficult to discriminate when only bright quasars are included. The bright end LF shape is close to that of a power-law with a slope that is almost identical at all redshifts.

Additionally, AGN are likely contributors to the X-ray background and several studies have determined the contribution by bright quasars to the diffuse background (e.g. Schmidt & Green 1986). How the low luminosity AGNs (LLAGNs) contribute to the diffuse X-ray background has been a question of interest for some time (Elvis et al. 1984; Koratkar et al. 1995). An accurate understanding of the behavior of the faint AGN LF and its evolution would help us to determine the global significance of their contribution to the soft X-ray background.

Little is currently known about how the faint end of the LF evolves because it is difficult to measure. Even at modest redshifts, LLAGNs become virtually impossible to observe from the ground. In ground-based images the unresolved nuclei cannot be distinguished from central regions of enhanced star formation or finite central density cusps of spheroidal components. For the first time, the Hubble Space Telescope eliminates this problem with its unique high resolution

imaging capabilities.

The Medium Deep Survey (MDS) (Griffiths et al. 1994) yields 2 to 4 parallel WFPC2 exposures per week, each containing ~ 300 galaxies down to $V \sim 23.5$ mag. This survey provides an ideal sample of distant field galaxies for which morphology and galaxy light profiles can be studied for the first time at sub-kiloparsec resolution. Typical galaxy redshifts are within $z \leq 0.6$ (Mutz et al. 1994). The set of Cycle 4, 5 and 6 images consists of ~ 150 fields with both V(F606W) and I(F814W) exposures.

This database provides a unique opportunity to search for morphological evidence of AGN or other compact nuclear activity such as starbursts. The nuclear activity of Seyfert galaxies manifests itself morphologically as an unresolved stellar-like point source in the nucleus of the galaxy. This is due to the fact that most of the emission is originating from a small region typically a few parsecs in diameter. For Seyfert 2 nuclei the emission is probably originating over the broader narrow-line region but is still highly concentrated at the nucleus having nuclear $\text{FWHM} \lesssim 200$ pc (Nelson et al. 1996). The physical size of an unresolved region in a WFPC2 image varies with redshift according to Figure 1.1. The unresolved region at redshifts less than 0.8 obviously encompasses that for Seyfert-like nuclei. Other enhancements of this size in a galaxy profile would include starburst regions and nuclear HII regions. Nuclear starbursts typically have sizes of a few hundred parsecs (e.g. Weedman et al. 1981 for NGC 7714) and nuclear HII regions may be even smaller. These stellar enhancements in a galaxy light profile would appear unresolved over the redshift range of interest ($0.2 \lesssim z \lesssim 0.8$) unless H_0 is very high. The typical late-type spiral bulge, however, has a diameter of ~ 1 kpc (Boroson 1981) which is resolved in the HST images.

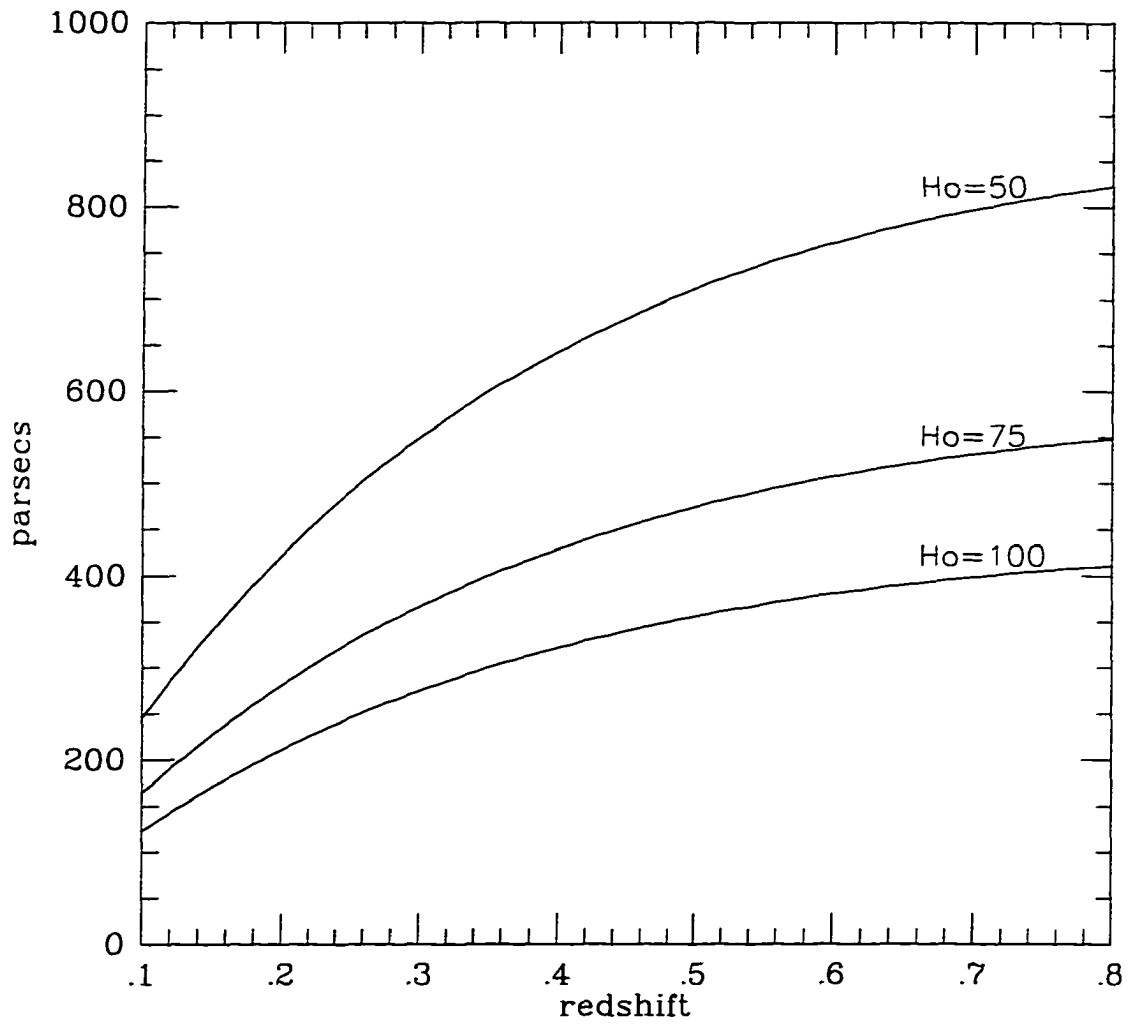


Figure 1.1 The diameter of an unresolved region in a WFPC2 image as a function of the object's redshift. The lines represent values of $H_0 = 50, 75$, and 100 km/s/Mpc .

In this study, all galaxies in 70 WFPC2 fields have been modeled to search for unresolved nuclei likely to be AGN or compact regions of star formation, i.e. starbursts. The galaxy modeling is based on maximum likelihood estimates used to extract quantitative morphological and structural parameters of the faint galaxy images. All galaxies to $I_{\lesssim 21.5}$ in 64 MDS fields and 5 Groth survey strip fields (Groth et al. 1997) as well as the Hubble Deep Field to $I_{\lesssim 23.5}$ (Williams et al. 1996) have been modeled in this way to reveal an unresolved nuclear component when present. Selection of AGN using this technique results in a magnitude-limited sample which is not biased towards galaxies dominated by the nucleus. Many other selection techniques, such as spectroscopic selection, require the nucleus to be the dominant galaxy component. In this way, we probe the intrinsically fainter population of AGN and starbursts out to intermediate redshifts for the first look at how this population of objects evolves.

In this thesis, the population of intermediate redshift galaxies containing unresolved nuclei is investigated. Chapter 2 discusses the process of selecting galaxies containing a significant nuclear component. The details of processing HST images and issues concerning incompleteness in the sample are also discussed. In Chapter 3 we discuss the ground-based spectroscopic follow-up for the selected galaxies and present the spectra. We also outline a photometric redshift technique used to estimate redshifts for selected galaxies without spectroscopic redshifts. Chapter 4 discusses the properties of the host galaxies and nuclei themselves such as colors, magnitudes, sizes, and Hubble types. We compare these properties with those of local Seyferts and starburst galaxies. We use the colors of the nuclei to differentiate between Seyfert-like nuclei and young starburst nuclei based on colors from representative spectra of these objects. Finally, Chapter 5 discusses the space density of galaxies containing compact nuclei. We present the upper

limit luminosity function for LLAGN in the magnitude range $-20 \leq M_B \leq -14$ in two redshift bins out to $z=0.8$ and compare it with the LFs of local Seyferts and moderate redshift QSOs. We also comment on the likely contribution of these nuclei to the soft X-ray background. Chapter 6 outlines the basic conclusions and possible future projects to be explored with this dataset.

CHAPTER 2

HUBBLE SPACE TELESCOPE IMAGES: REDUCTION AND GALAXY MODELING

The images used in this study were obtained with the Hubble Space Telescope Wide Field Camera-2 (WFPC2). Here we describe the procedure for processing the images and detecting galaxies in the fields. The galaxy light profile fitting procedure is also discussed as well as the criteria for detecting galaxies containing an unresolved nuclear component. We estimate completeness levels for the survey based on Monte-Carlo simulations of the data and apply these to the selected galaxies to estimate the fraction of all galaxies that contain an unresolved nuclear component.

2.1. Fields Selected from the Survey

The Medium Deep Survey (MDS) is composed of images obtained in parallel while HST observed a primary target with one of the other instruments. The fields were observed in the I (F814W) and V (F606W) filters primarily, with some fields

also being imaged with the B (F450W) filter. The data used for this study are comprised entirely of post-refurbishment HST images obtained with the WFPC2 camera from 1994, January to 1996, July. The fields were chosen to lie at a range of high galactic latitudes away from known nearby galaxy clusters and other bright objects.

During this timeframe, the MDS obtained images of 209 survey fields. From these data the fields for this study were chosen to have images in both the V and I filters so that color information would be available. Each field contained at least one exposure in both V and I with total exposure times ranging from 2000 to 23100 seconds in I and 300 to 16500 seconds in V with a median exposure time at ~ 5000 seconds. The number of exposures per field ranges from 1 to 12 with a median number of exposures at ~ 3 . Table 2.1 lists the field name, RA and DEC, Galactic latitude, number of exposures and total exposure time in seconds in the V and I filters for each field selected from the MDS for this study. Also included in this table are the six additional non-MDS HST fields used in this study; five fields from the Groth Survey strip (Groth et al. 1997) and the Hubble Deep Field (Williams et al. 1996).

2.2. Reduction of HST WFPC2 images

Many of the details of the calibration process can be found in Ratnatunga et al. (1997) and references therein. Here we will summarize the basic information regarding calibration and reduction of the HST images. The WFPC2 images are calibrated using the STScI static mask, super-Bias, super-Dark and flat field calibration files. These were created by STScI to calibrate the Hubble Deep Field. Pixel flux is corrected when necessary using the hot pixel tables from STScI over

the time when each observation was taken. Hot pixels which cannot be corrected to the same accuracy are rejected.

The stacking procedure is described in detail in Ratnatunga et al. (1994). A corrected version of the IRAF/STSDAS COMBINE task is used to combine the images and generate a “sigma” image from the statistical errors. This sigma image is an estimate of the rms error of every pixel in the calibrated stack and reflects the cosmic ray pixels rejected in the stacking procedure, the flat field response, and any subtracted background sky gradient or scattered Earth light. The amount of shifting necessary between images is determined from “jitter files”, i.e. the HST aspect solution for the WFPC2. Exposures are stacked with shifts corresponding to the nearest integer number of pixels without any rotation. We allow a maximum 50 pixel shift. The orientation usually remains constant although a maximum difference in rotation of less than 0.03 degrees is allowed, ensuring a 1-to-1 mapping of the pixels.

Cosmic rays affect about 7 pixels per second per CCD chip during the length of the exposure time. When three or more exposures in the same filter are available along the same direction with the same orientation, cosmic rays can be effectively removed by stacking the images with a 3-sigma clip. When only two images were available, the stacking operation will leave the fainter cosmic rays on the output image which could be mistakenly detected as faint objects. Cosmic rays can be rejected in images with only one exposure per filter when at least one exposure has been obtained in the other filter.

Once the images are stacked, objects are located independently on each image using an algorithm developed for HST-WFPC data. It is based on finding local maxima and mapping nearby pixels to the central object and selecting the

detections which are significantly above the noise. Any significant gradient in the sky background, caused by a nearby bright object or scattered Earth light, is subtracted from the stacked image. After the initial finding algorithm has been applied, the exposure is examined to confirm that it satisfies being part of the Medium Deep Survey and does not contain parts of bright, resolved galaxy fields or globular clusters. Object detections in the two filters are matched by software to create a single catalog with a revised mask for each image so that corresponding pixels in different filters are associated with the same object.

2.3. Galaxy Fitting Software

The software for modeling the galaxy light profile has been developed by K. Ratnatunga (Ratnatunga et al. 1997). The empirical model used is scale free and axisymmetric with an exponential, power-law profile. Such models have been shown to fit the broad distribution of normal galaxies. The galaxy components modeled with this software are an exponential disk, an $r^{1/4}$ bulge, and an $\exp(-r^2)$ Gaussian profile for a point source.

For each galaxy imaged in the HST WFPC2 field, a contour is defined around the object by selecting those pixels which are greater than one-sigma above the estimated local sky level. The integrated signal-to-noise ratio of these pixels is a good measure of the information content of the image. The decimal logarithm of this integral, called SNRIL, is linearly correlated with the galaxy magnitude. These pixels within the one-sigma contour are used to estimate each galaxy's center, magnitude, size, orientation, and axis ratio using simple moments of the flux above the mean. An elliptical annular region around the object is selected to define the mean sky background to 0.5% accuracy.

The maximum likelihood parameter estimation starts by using these moments to estimate initially the model parameters. The software creates a model image of the object, convolves this model with the WFPC2 stellar Point Spread Function (PSF) and compares it with the observations within the selected region. The likelihood function is defined as the probability for each model pixel value with respect to the observed pixel value and its error distribution. The function is evaluated as the integral sum of the logarithm of these probabilities. The likelihood function is maximized using the modified IMSL minimization routine (Ratnatunga & Casertano 1991).

The number and choice of parameters fitted to an image is clearly important and defines the light profile model. In this study, each galaxy is fit down to a limiting SNRIL with 3 different model choices to determine the best fit to the data. The first model is a 2-component disk+bulge model. This version of the fitting software is flexible so that a pure disk, pure bulge, pure Gaussian point source, or bulge+disk model can be output as the best fit to the data. The parameters which can be fit in this model are: 1) sky magnitude, 2) x-position, 3) y-position, 4) total magnitude, 5) half-light radius of the bulge+disk model (the radius within which half the light of the unconvolved model would be contained if it were radially symmetric), 6) disk axis ratio, 7) orientation of the galaxy, 8) bulge/(disk+bulge) luminosity ratio, 9) bulge axis ratio and 10) bulge/disk half-light radius ratio.

The first step utilizes a special quick mode of the minimization routine which attempts a 10-parameter disk+bulge fit. It does not check for full convergence but does reach a point in the multi-dimensional parameter space which is close enough to the final answer to investigate the likelihood function and make some intelligent decisions. If the half-light radius of the object is less than one pixel, a 5-parameter

Gaussian model is tested to see if the object is point-like. If the point source model does not improve the fit, a single-component disk or bulge model is attempted. Significant improvement in a model is achieved if the difference in the likelihood function values (the likelihood ratio) is greater than 6.0. This likelihood ratio (LR) is used throughout the modeling process to determine if significant improvements are made with new model fits. The 2-component bulge+disk model is then checked to see if it improves upon the single model bulge or disk fit. Sub-pixellation in the center of the galaxy is tried to see whether a high resolution center will change the likelihood function significantly. The best fit parameters for the chosen model are determined through an iterative process using the model IMSL minimization routine.

The software creates an output FITS data image for each object. The image is a grid with a row of 7 images for each filter shown in Figure 2.1. The images in each row are: 1) the observed full area for each galaxy from the stack, 2) the selected region for analysis, 3) the PSF convolved maximum likelihood model image, 4) the maximum likelihood model image, 5) the residual image (model subtracted from real image), 6) the sigma image, 7) the object mask image.

A second version of the software was produced which allows for a disk+point source fit. This version is very similar to the 2 component disk+bulge version. The main difference is that the second component is a Gaussian point source instead of an $r^{1/4}$ bulge component. The parameters for this model are: 1) sky magnitude, 2) x-position, 3) y-position, 4) total magnitude, 5) half-light radius of the disk, 6) disk axis ratio, 7) orientation of the galaxy, 8) point source/(disk+point source) luminosity ratio, 9) x difference in position between the disk and point source and 10) y difference in position between the disk and point source.

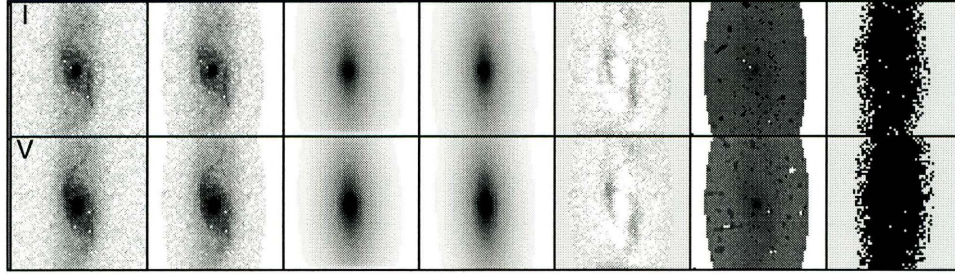


Figure 2.1 Output from the 2-dimensional modeling software. From left to right the boxes are: 1) the observed 64 x 64 pixel area around the galaxy, 2) the selected region for analysis, 3) the PSF convolved maximum likelihood model image, 4) the maximum likelihood model image, 5) the residual image (model subtracted from real image), 6) the sigma image, 7) the object mask image.

The point source is allowed to be at a different origin from that of the disk component. This technique avoids the problem of not converging on a real point source because it is not at the precise center of the disk. Later in the selection process, restrictions can be placed on how far off-center the point source nucleus can be and still be considered a “nucleus”. These restrictions are described in section 2.7.2. The half-light radius of the Gaussian shape representing the point source is held constant at 0.0183 arcsec, before convolution with the point spread function. This is consistent with that measured for stars in the WFPC2 fields and is essentially a measurement of the telescope “jitter”. The axis ratio for this component is set at 1.0.

A third version of the software allows for a 3-component disk+bulge+point source fit to the galaxy light profile. This model is somewhat more complicated than the previous versions due to the third component. The parameters fit for this

model are: 1) sky magnitude, 2) x-position, 3) y-position, 4) total magnitude, 5) half-light radius of the disk+bulge portion of the model without regard to light from the point source nucleus, 6) disk axis ratio, 7) orientation of the galaxy, 8) bulge/(disk+bulge+point source) luminosity ratio, 9) bulge axis ratio, 10) bulge/(bulge+disk) half light radius ratio, 11) point source/(disk+bulge+point source) luminosity ratio, 12) x difference in position, 13) y difference in position. Parameters 12 and 13 reflect the fact that the point source is allowed to have a different origin from the remainder of the galaxy model. The half light radius of the Gaussian shape is constant at 0.0183 arcsec and the axis ratio for this component is 1.0.

2.4. Selection of Galaxies Containing Nuclear Point Sources

Each galaxy is fitted with all three versions of the fitting software. The model with the lowest likelihood function value indicates the best fit or the closest model to the real data. Those galaxies best fit with either the disk+point source model or the disk+bulge+point source model are initially selected as nuclear point source candidates. It is important, however, to understand whether or not the model containing a point source component is substantially better than one without the point source component. In the following sections we describe various simulations and tests designed to determine the criteria for selecting a galaxy containing a nuclear point source.

2.4.1. Spurious Point Source Detections in Simulated Galaxies

To determine the uniqueness of a fit with a galaxy model containing a point source, simulated galaxies with no point source component were fit in the same way as galaxies in the survey. These simulated galaxies have a range of magnitudes, signal-to-noise ratios, bulge-to-total light ratios and half light radii and were produced in both V and I images where the V magnitude of each galaxy is one magnitude fainter than the I magnitude. Each of the 1152 galaxies in this simulation were fit with a disk+bulge model, disk+point source model, and a disk+bulge+point source model.

The model with the lowest likelihood function value is chosen as the best fit. The simulations are used to determine what minimum likelihood ratio must be met by the model containing a point source over the model not containing a point source. The simulated galaxies, which do not contain any nuclear point source component, were found to have a best fit model which did include a point source nucleus 30% of the time. The likelihood ratio between the non-point source component model and the point source component model for these fits determines the range in likelihood ratios for spurious point source detections.

Figure 2.2 shows the log of the likelihood ratio (LR) between the non-point source component model and the point source component model as a function of various parameters of the galaxy: measured magnitude, bulge-to-total luminosity ratio, and point source-to-total luminosity ratio as well as a histogram of the LR values. This diagram includes all spurious point source detections in the simulated galaxies, i.e. all instances where the point source component model was the best fit to the simulated galaxies. The LR values do not appear to vary with bulge-to-total measurement but a weak trend is detected with galaxy magnitude, where the

brighter galaxies tend to have a larger LR for spurious nuclear detections. The frame plotting log likelihood ratio vs. point source-to-total luminosity ratio reveals that many of the spurious detections occur at small point source-to-total values.

A histogram of the point source-to-total luminosity values is shown in Figure 2.3. The bulk of spurious point source detections occur at ratios less than 1%. If a point source-to-total luminosity ratio cut-off is applied to these data at 1%, we can re-examine how the LR varies with these galaxy parameters (Figure 2.4). We find that we have eliminated most of the spurious detections (75%) and the trend with LR to galaxy magnitude is no longer apparent. The histogram of the remaining spurious detections indicates that an LR cut-off of 50 (log likelihood ratio of 1.7) will remove almost all points.

The simulations indicate that choosing a best fit galaxy model where the point source-to-total luminosity ratio is greater than 1% and the LR value is greater than 50 will avoid almost all spurious point source detections. Of the 1152 galaxies in this simulation, only 4 would still be selected after applying these criteria resulting in 0.3% of fitted galaxies which could contain spurious point source detections.

2.4.2. Measurement of Detected Point Source Nuclei

Not only is it important to determine how often spurious detections will occur in our galaxy sample using simulated galaxies, we also need to define when and how often inaccurately measured point source nuclei are detected in the sample. For the purposes of determining completeness and to quantify the frequency of inaccurately measured point source nuclei, a partially simulated galaxy dataset was produced. The dataset consists of real galaxy images from several MDS fields where simulated point sources of various magnitudes were added at the nucleus.

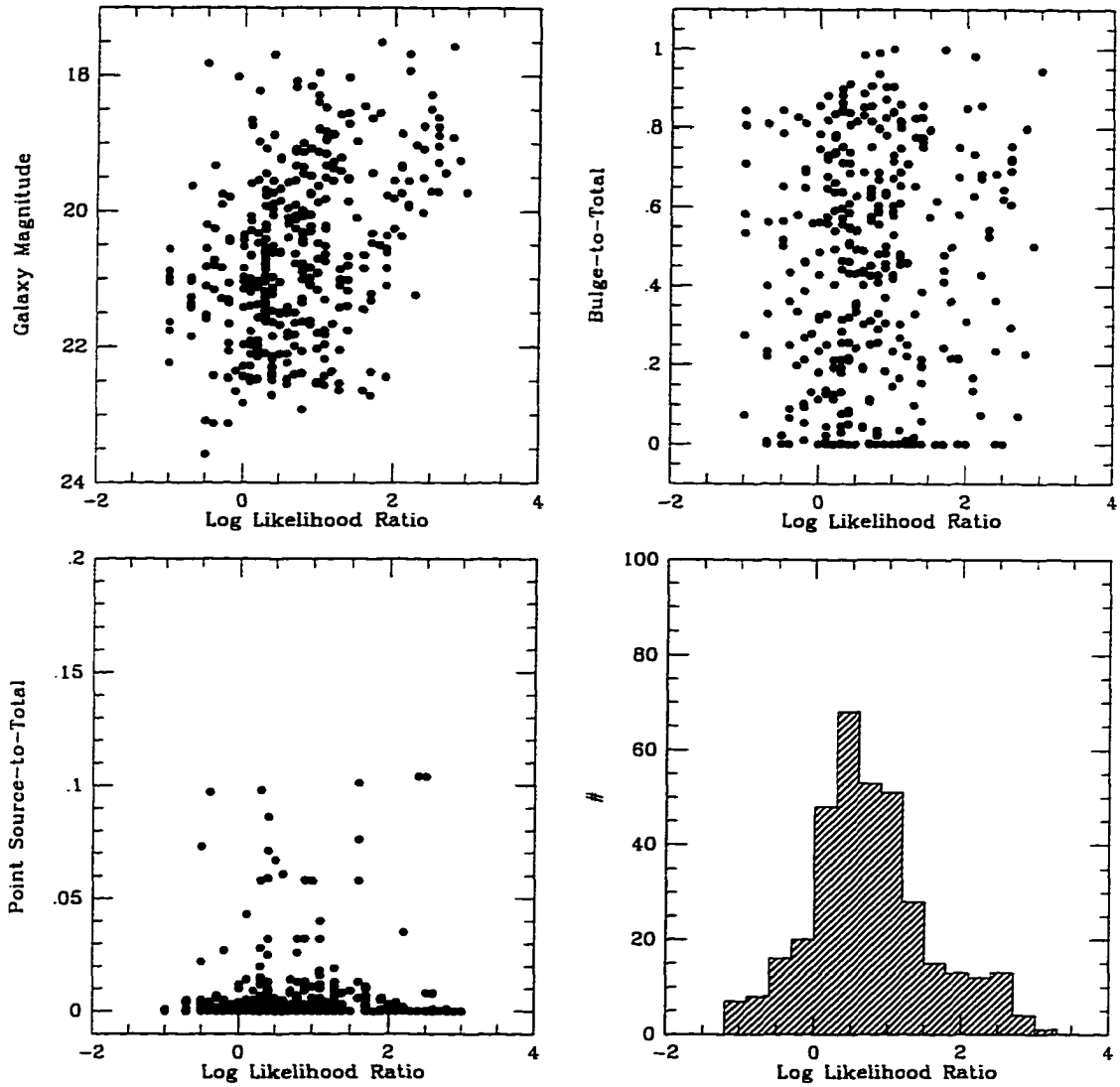


Figure 2.2 Fitting parameters for spurious point source detections in simulated galaxies. The likelihood ratio represents the degree to which the model with a point source component is better than the model without a point source component in fitting the simulated galaxies.

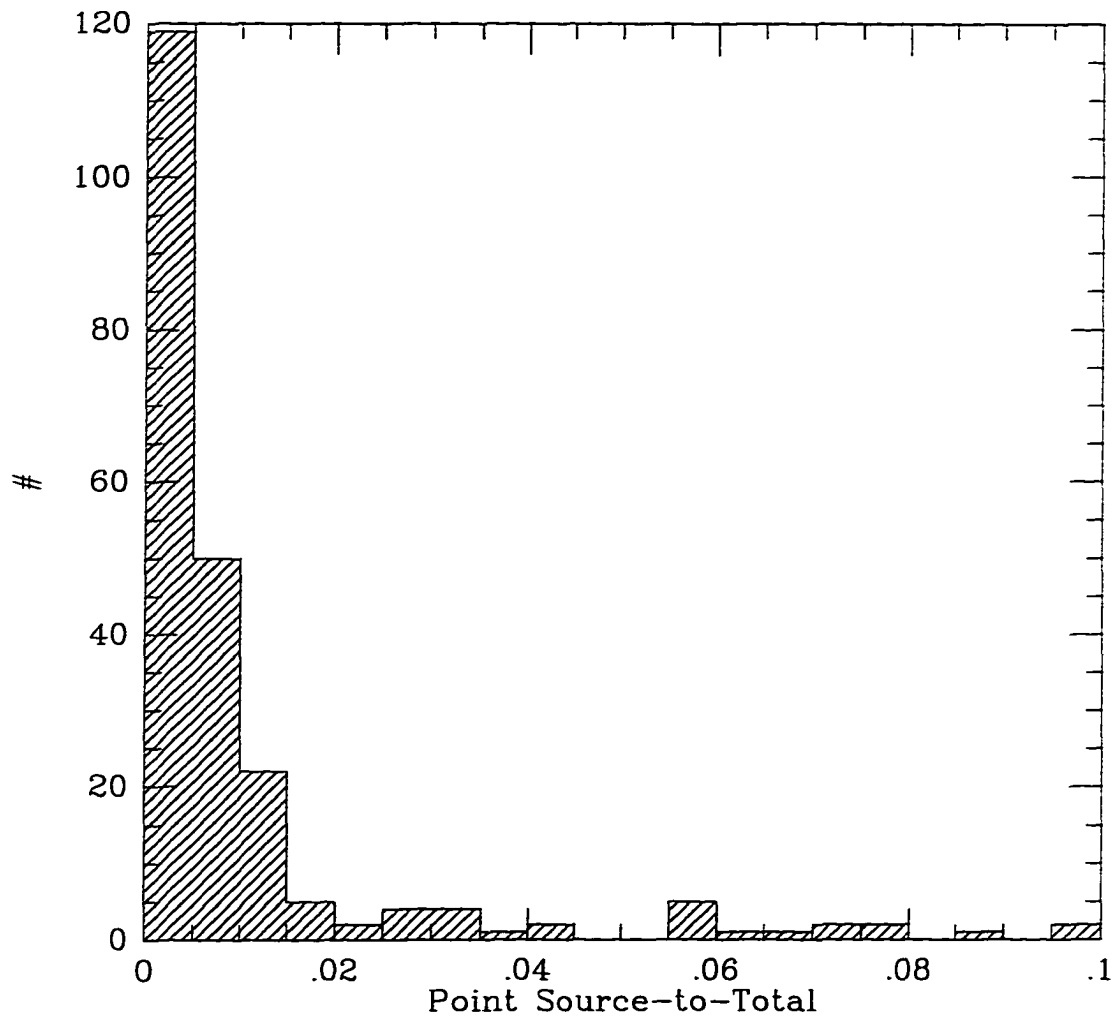


Figure 2.3 Histogram of the number of spurious point source detections as a function of the point source-to-total luminosity ratio.

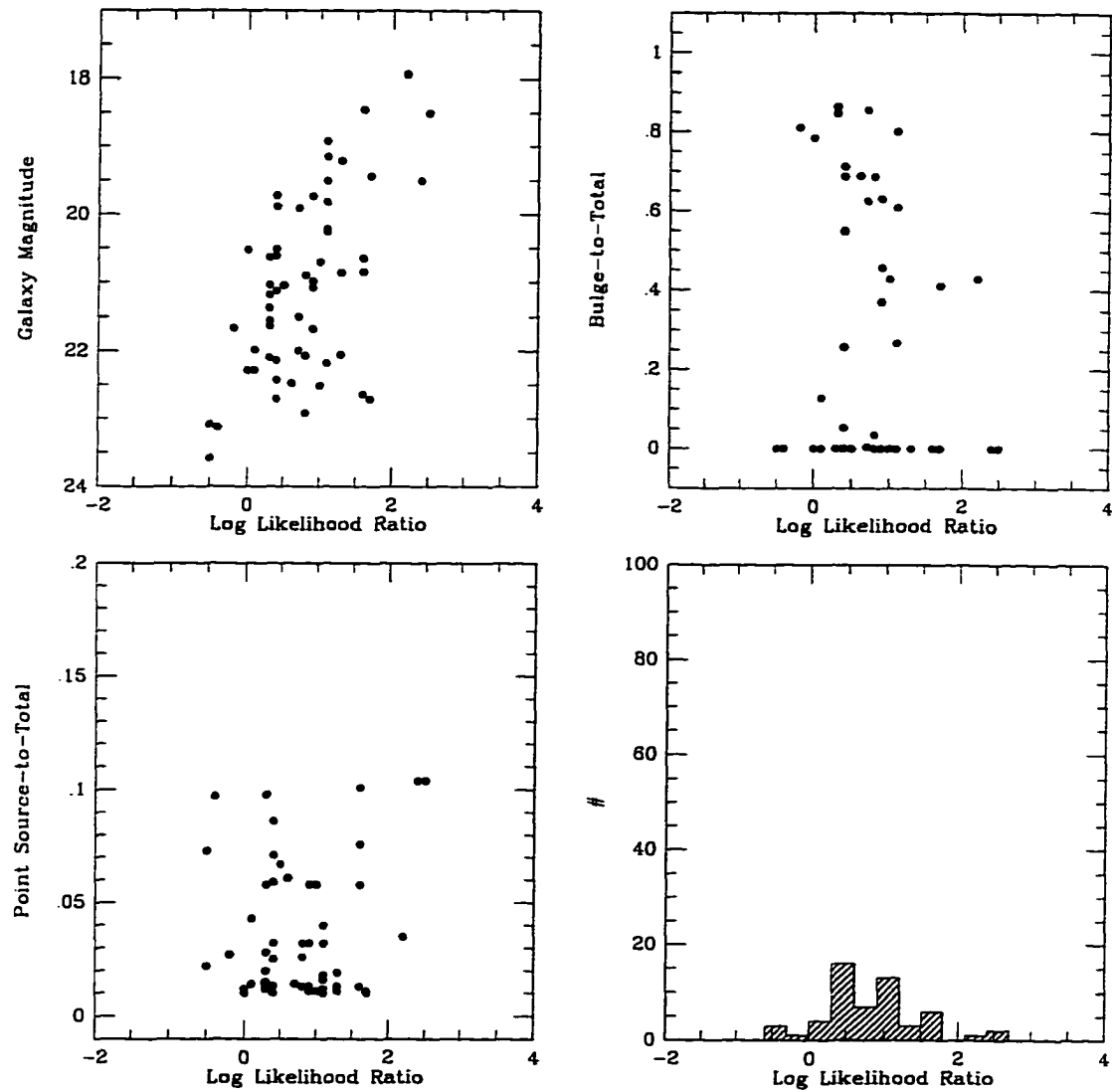


Figure 2.4 Fitting parameters for spurious point source detections in simulated galaxies. All point source detections less than 1% of the total galaxy light have been removed

A total of 98 galaxies from 10 MDS fields were used in this Monte-Carlo type simulation. Each galaxy image was reproduced 10 times and had added to it point sources of apparent magnitudes evenly spaced between $I=21.5$ to 26.0 and $V=22.5$ to 27.0 . This simulation created a total of 1960 galaxy images (98 galaxies \times 10 point source magnitudes \times 2 filters (V and I)).

The galaxies with simulated point source nuclei had a variety of bulge-to-total ratios, apparent magnitudes, and SNRIL values (Figure 2.5). The 2-component disk+bulge model, the 2-component disk+point source model, and the 3-component disk+bulge+point source model were applied to each of the simulated galaxies. The best fit model was determined as that with the lowest likelihood function value. To be selected as a galaxy containing a nuclear point source component, we required that the point source be at least 1% of the galaxy light and that the likelihood ratio for the model containing the point source component be lower by a value of 50 than the model without a point source component. These criteria were applied to avoid spurious point source detections as described above and will also be applied to the real galaxy sample. To provide a check on our likelihood ratio requirement, we examined the increase in detected real point sources in this set of simulations as compared to the increase in spurious detections made with a lower likelihood ratio requirement. We find that the increase in detected real point sources is negligible (\sim few%) compared to the doubling of spurious detections when the likelihood ratio is lowered from 50 to 30 and therefore maintain the current likelihood ratio requirements for detecting nuclear point sources.

Based on the results from this simulation, we determined how well the input nuclear point source is detected and how accurately its magnitude is measured. Figure 2.6 shows how the measured magnitude of every detected point source in

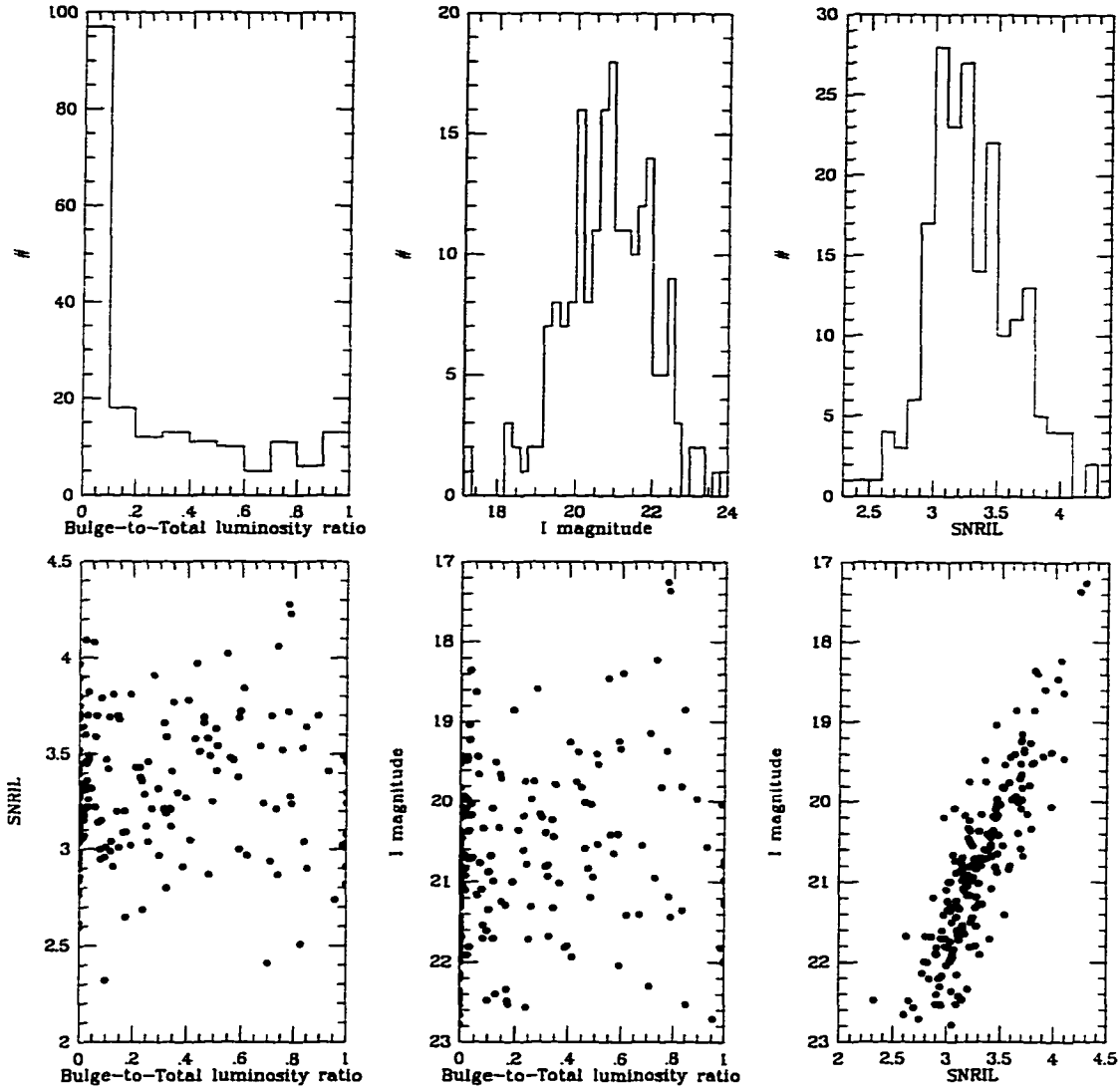


Figure 2.5 Parameters of galaxies used in the Monte-Carlo simulation. The galaxies cover a range of Bulge-to-Total luminosity ratios, magnitudes and SNRIL values. SNRIL is the integrated signal-to-noise measurement described in the text.

the simulated data compares with its input V and I magnitudes. Although many of the points fall near the input magnitude values, a large number are measured brighter than the input magnitude. Careful examination of the model fits for these cases indicate that they are galaxies containing significant bulge contributions. The bulge appears to often confuse the magnitude measurement of the point source component. For this reason, it is necessary to set additional selection criteria for point source detections to avoid inaccurately measuring point source magnitudes.

Because our data contain information in both the V and I filters, we can compare the model in the two different filters and note any oddities. First, many of the poorly measured point source nuclei were detected in one filter while going undetected in the other filter. This result is not unacceptable unless the measurement of the bulge is very different in the two filters. It is clear that the bulge is affecting the point source measurement in the case where a large bulge contribution is measured in one filter while a point source is detected with no bulge component in the other filter. To avoid these point sources measured too bright because the bulge light is included in the point source, we note all the cases in the simulated data where the bulge is measured much larger in one filter (bulge-to-total difference in the 2 filters is greater than 0.25) and a point source with no bulge component is measured in the other filter. In the simulated dataset, 69 point sources are detected in galaxies fulfilling this criterion. Removing these points as candidates eliminates many of the points in Figure 2.6 measured as too bright.

These simulations also show that if the galaxy contains a large bulge component in both filters and the point source is the same color in (V-I) as the galaxy, it is often measuring the point source magnitude incorrectly. We also know that many elliptical galaxies have “cuspy” luminosity profiles (Lauer et al.

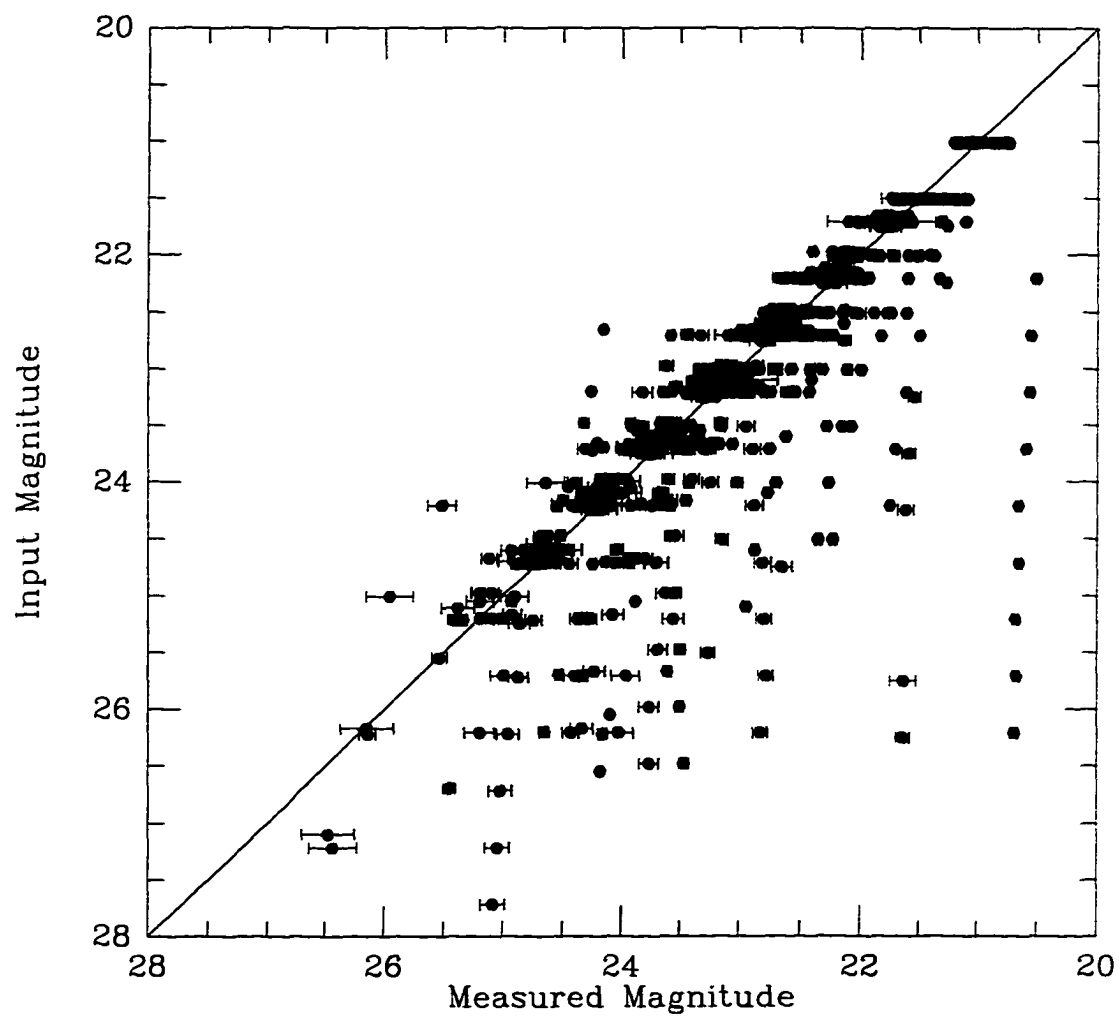


Figure 2.6 The input vs. the measured magnitude for the point source nuclei detected in the Monte-Carlo simulation.

1995) which can easily be mistaken for unresolved nuclei in moderately redshifted galaxies. If a small point source is placed in these galaxies in our simulations, a bright point source may be measured due to the inclusion of the cuspy light from the galaxy itself. In these cases, we would expect that the color of the point source be the same as the galaxy, within the errors. This occurs for 77 of the point sources in this simulation.

Finally, each galaxy model in which a point source is detected must be checked for proper convergence. This check is done by examining the matrix solution of the light profile model. A total of 56 galaxies best fit with a point source model were removed due to the non-convergence of the point source component in the model.

Figure 2.7 shows the measured magnitude vs. the input magnitude for the remaining 597 selected point source galaxies after removing the subsets of systematically inaccurate and non-converging point source models described above. These additional selection criteria have successfully removed the majority of poorly measured point source nuclei. The solid line represents the one-to-one relationship between input and output magnitudes. The dashed vertical errorbars are the standard deviation error in the real point source nucleus magnitude as a function of the measured magnitude based on the spread of the points in the figure. We show in Figure 2.8 histograms of $\text{mag}_{\text{obs}} - \text{mag}_{\text{real}}$ for point sources at 23 ± 0.25 and 24 ± 0.25 magnitudes. The dashed line is the normalized Gaussian distribution for the calculated σ_{mag} of each distribution. We note that the distribution is narrower than the normalized Gaussian distribution and therefore the adopted errors are conservative and are may overestimate the actual error in magnitude for many of the measured point sources. A least squares fit to these 1σ errors as a function of

observed magnitude yields the following equation,

$$\sigma_{mag} = 0.324 - 0.0685 \times (23 - mag) + 0.0075 \times (23 - mag)^2 \quad (2.1)$$

which gives the error in magnitude determination as a function of the measured magnitude. This equation is later applied to the real point source nuclei detected in the sample to obtain a true magnitude error.

2.5. Accuracy of the Host Galaxy Bulge Measurements

Figure 2.7 shows that the point source nuclei can be accurately measured to ± 0.40 magnitude for faint (24th magnitude) nuclei and ± 0.26 magnitude for bright (22nd magnitude) nuclei. In spite of fairly accurate nuclear magnitude determinations, we find that the bulge component is often misfit in our simulations. Figure 2.9a reveals how the bulge-to-bulge+disk luminosity ratio ($B/B+D$) in the simulation galaxies differs from that measured for these galaxies once a point source nucleus has been added and detected. It is clear that the bulge component is often not measured at all when a point source is present. This is most likely caused by the tendency of the modeling software to chose a model with fewer parameters and therefore fewer components as the best fit unless the fit is greatly improved by additional parameters. When a prominent point source is present, even a large bulge component can go undetected.

Figure 2.9b reveals how the measured bulge-to-bulge+disk ($B/B+D$) varies with the point source-to-total luminosity ratio. For point source nuclei greater than $\simeq 20\%$ of the total galaxy light, the bulge is almost always undetected. Above 20% the bulge is obviously dominated by the point source component and it becomes impossible for the software to detect the bulge component. Only where the point

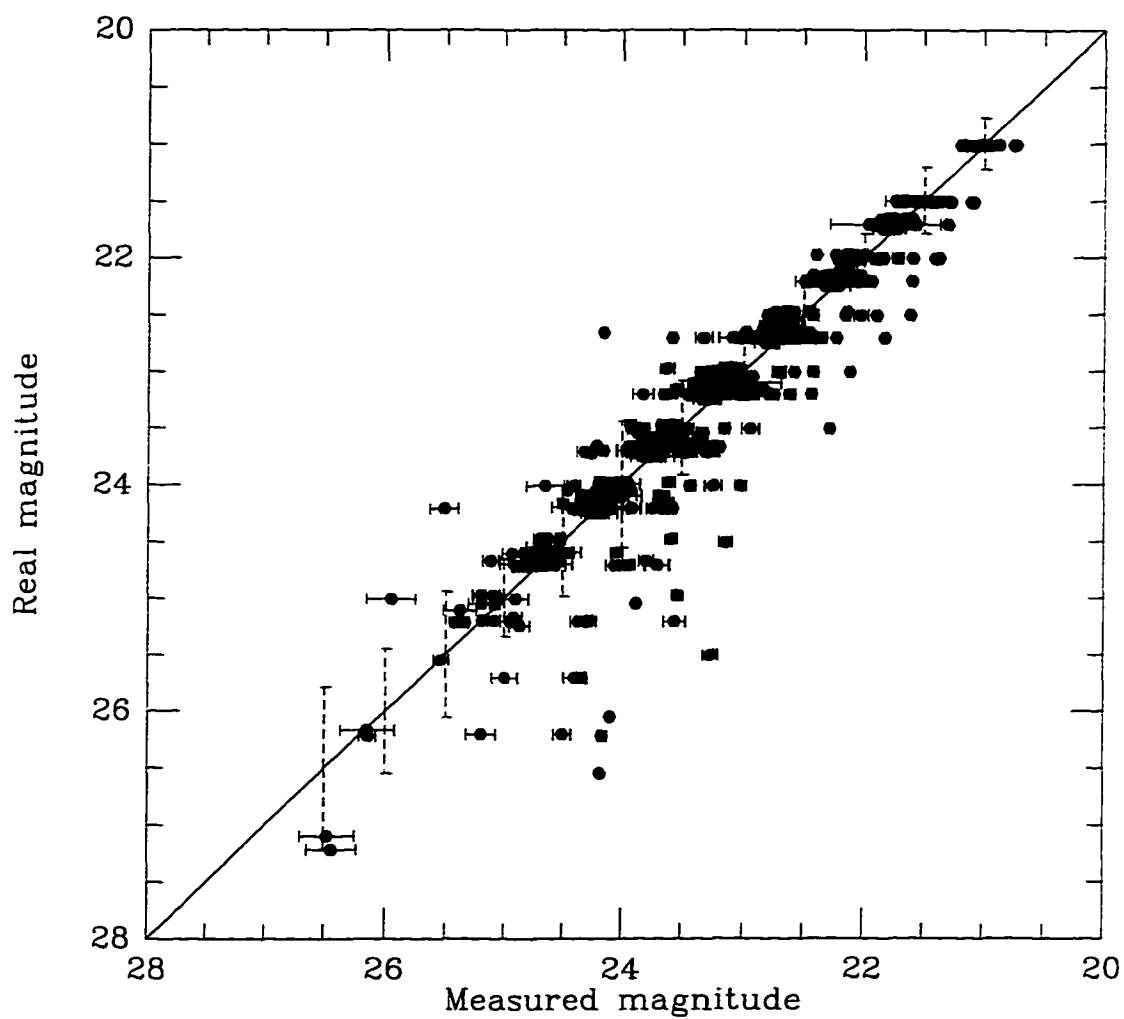


Figure 2.7 The input vs. the measured magnitude for the point source nuclei detected in the Monte-Carlo simulation after applying the selection criteria outlined in the text.

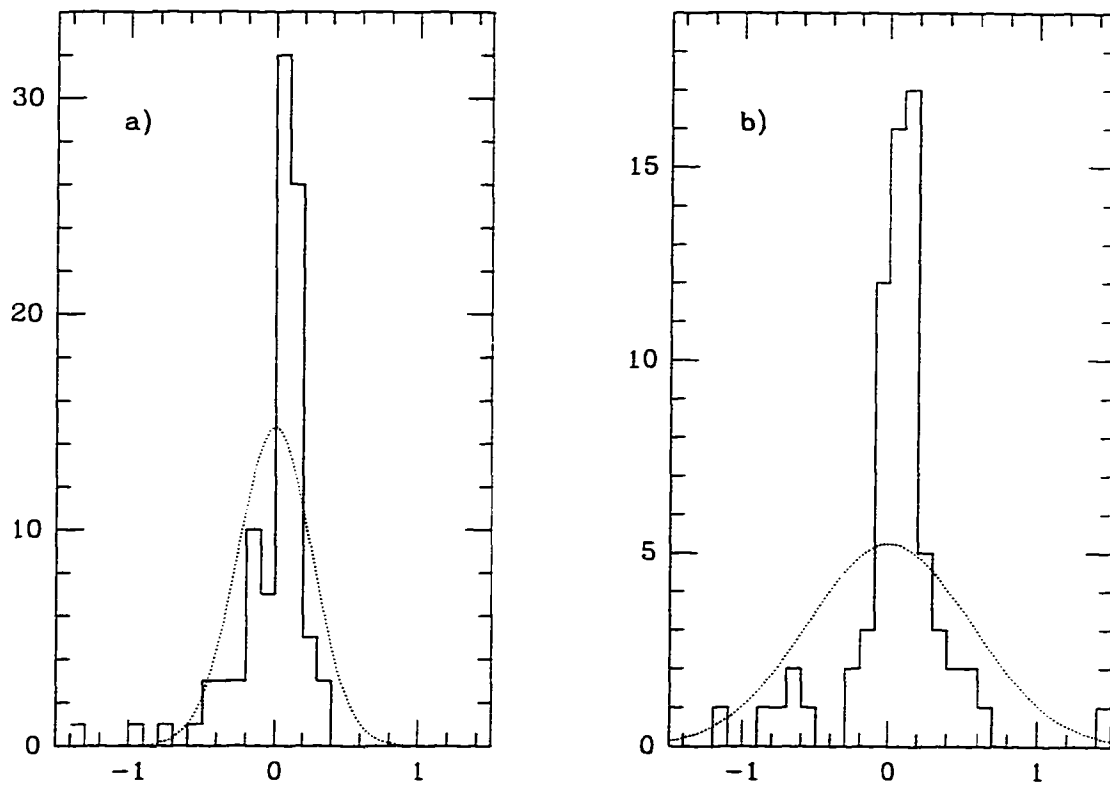


Figure 2.8 a) The histogram of $\text{mag}_{\text{obs}} - \text{mag}_{\text{real}}$ for point sources at 23 ± 0.25 . The dotted line represents the gaussian curve with $\sigma = 0.26$. b) Same histogram for point sources at 24 ± 0.25 magnitudes. The gaussian represents $\sigma = 0.56$.

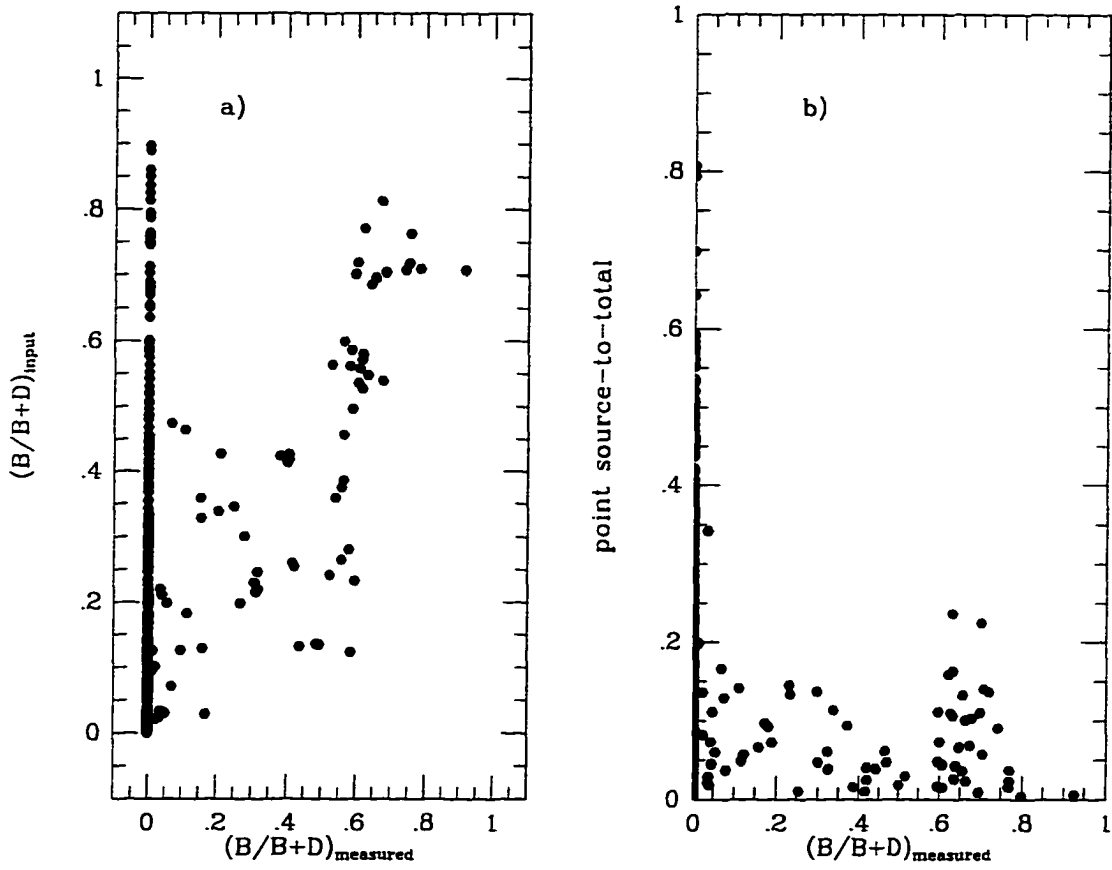


Figure 2.9 a) The Bulge-to-Bulge+Disk measured in galaxies within which point source nuclei were detected in the simulations vs. the input Bulge-to-Bulge+Disk for the host galaxy. b) The measured Bulge-to-Bulge+Disk as a function of the point source-to-total luminosity ratio for galaxies in the simulations in which point source nuclei were detected.

source is below 20% of the galaxy light can we adequately measure the bulge component of the galaxy in addition to the point source component.

The results of these simulations suggest that although the bulge is often measured incorrectly when a point source is detected, the magnitude of the detected point source is correct within the determined errors. For this reason, our main goals of determining nuclear magnitudes and colors are unaffected by these errors in measuring the bulge contribution. We discuss in Chapter 4 how these results effect the determination of the host galaxy types and colors and attempt to statistically correct for errors in the bulge measurement in our sample.

2.6. Completeness

To determine the level of completeness in this survey, a Monte-Carlo simulation was performed. The dataset used for this experiment is that described above, where real galaxy images are combined with point source nuclei of varying magnitudes. The fitting software is then used to determine the best fit model to the data. After applying the criteria to ensure accurately measured, real nuclear point source components, we determine the number of galaxies in which the unresolved nucleus is detected. Since each galaxy in the simulation contains a point source for which the input apparent magnitude is known, the level of completeness in detecting nuclei as a function of the point source brightness can be determined.

To eliminate spurious point source detections, each detected point source must be at least 1% of the total galaxy light based on modeling of simulated galaxies described in section 2.4.1. For this reason, very faint nuclei are not detected in bright galaxies but a nucleus of the same magnitude might be detected in a fainter galaxy if it is above the 1% limit. Because of the related nature of detected nuclei

and the magnitude of the host galaxy, we cannot address the issue of completeness in terms of limiting magnitudes. Instead, the level of completeness in detecting point source nuclei is based on the percentage of galaxy light that the point source comprises.

We begin by estimating completeness for those galaxies in which no bulge component is detected. These galaxies are adequately modeled in our sample with a pure exponential disk. The galaxies, which contain simulated point source nuclei of varying point source-to-total luminosity ratios, were fitted with the fitting software and those containing accurately measured point source components were selected. Figure 2.10a shows a histogram of the number of galaxies in the simulation for which there was no input bulge component as a function of the input point source-to-total luminosity ratio (solid line). The hatched region represents the histogram of galaxies in which the point source nucleus was detected and no bulge component was measured, consistent with the input bulge parameter value. Figure 2.10b is the fraction of galaxies as a function of input point source-to-total luminosity ratio in which the point source was accurately modeled. The error bars are the Poisson 1σ error based on the number of points in each bin. These fractional values can be applied to those galaxies in the real survey sample containing no measured bulge component to determine the level of completeness in detecting point sources.

Estimating completeness for the galaxies containing a bulge component is somewhat more complicated. For the rest of this discussion we define the bulge component in terms of bulge-to-bulge+disk ($B/B+D$) luminosity ratio so that a galaxy with no disk has a luminosity ratio of 1.0. Figure 2.9 indicates that when a point source is detected, the galaxy $B/B+D$ may be quite inaccurate, especially

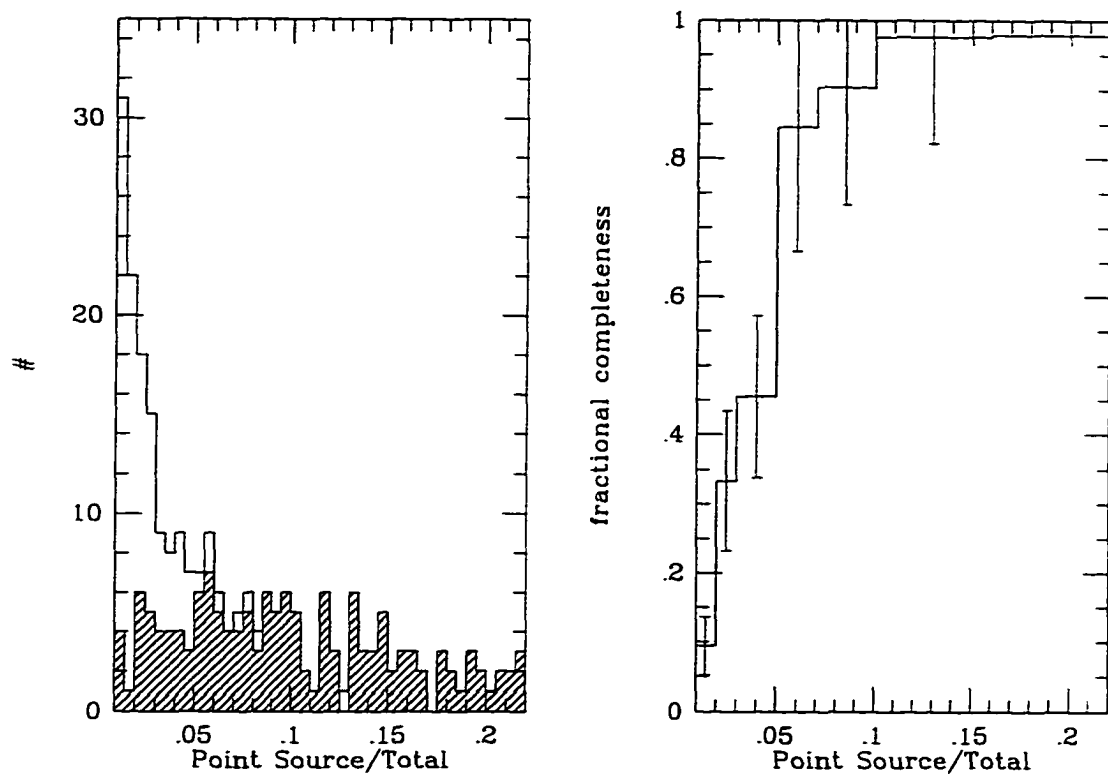


Figure 2.10 a) The histogram of galaxies in the simulation containing no bulge component as a function of the point source-to-total luminosity ratio. The solid line represents all galaxies in the simulation with no bulge component and the hatched region represents those galaxies in which the nuclear point source was detected. b) The fractional completeness or success rate in detecting point source nuclei in galaxies containing no bulge component. The errorbars are the Poisson statistics based on the number of objects in each bin.

if the point source-to-total luminosity ratio is greater than 20%. For this reason, to estimate completeness for the galaxies in our sample containing some bulge component, it is best to separate our simulation results into bins of different *input* $B/B+D$ values as opposed to using the measured $B/B+D$ values. This is consistent with the null hypothesis approach we have adopted for modeling the galaxy light profile: we assume that each galaxy does not contain a point source and the galaxy light profile model must be significantly improved with the point source component for the nucleus to be detected.

Figure 2.11 is plotted similarly to Figure 2.10. The three left panels show the histogram of galaxies in the simulation (solid line) and those for which the point source nucleus was detected (hatched region) for different input $B/B+D$ galaxy types. The Figure 2.11a represents galaxies with $0 < (B/B+D) \leq 0.4$, 11b is for galaxies with $0.4 < (B/B+D) \leq 0.8$ and 11c is for $0.8 < (B/B+D) \leq 1.0$. The adjacent panels on the right indicate the percentage of point sources detected as a function of the point source-to-total luminosity ratio and is an estimate of the completeness. These percentage estimates can be applied to the real sample galaxy $B/B+D$ distribution to estimate completeness as a function of point source -to-total luminosity ratio for the entire survey. An estimate of the total completeness in detecting point source nuclei for the survey data is calculated in the next section based upon the outcome of this simulation.

2.7. Application to the Survey Data

2.7.1. Determining the Limiting SNRIL value

Every galaxy in each of the fields listed in Table 2.1 was fitted down to an apparent magnitude limit corresponding to a SNRIL value of 2.5. This limit is typically

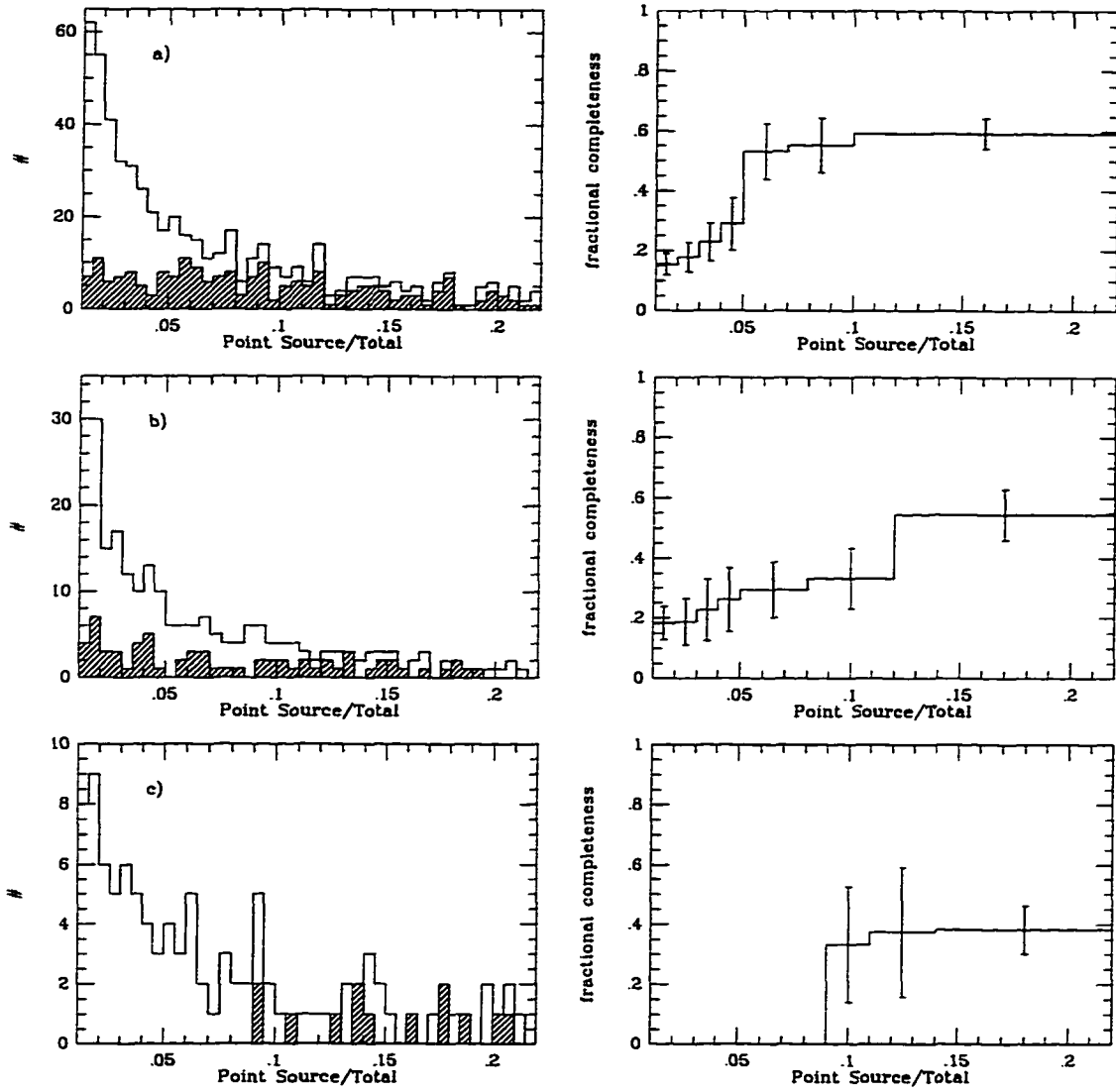


Figure 2.11 a) The histogram of galaxies in the simulation containing bulge components with $0 < (B/B+D) \leq 0.4$ as a function of the point source-to-total luminosity ratio. The hatched region represents those in which the point source nucleus was detected. The panel to the right is the fractional completeness or success rate in detecting point source nuclei for these galaxies. b) Same as above except for galaxies with $0.4 < (B/B+D) \leq 0.8$. c) Same as above except for galaxies with $0.8 < (B/B+D) \leq 1.0$.

around $I \simeq 22.0$ for the average MDS field. This SNRIL value was chosen since it appears to be the signal-to-noise level required for accurate fitting of the simple disk+bulge model (Ratnatunga et al. 1997). For the model requiring an additional point source component, the SNRIL cut-off should be higher.

To determine the SNRIL cut-off for the data, we again use the simulated dataset consisting of real galaxies with added simulated point source nuclei. As shown in Figure 2.5, these galaxies cover a range of SNRIL values. These data can be used to determine at what SNRIL value for the galaxy the point source nucleus is no longer detected. Figure 2.12 is the histogram of galaxies as a function of their measured SNRIL value. To avoid some of the incompleteness based on faint point sources as described in the preceding section, this histogram includes only points measuring greater than 3% of the total galaxy light. In Figure 2.12a and 2.12b the solid line is the total number of galaxies as a function of SNRIL and the hatched region is the number of galaxies where the added point source component was detected. The solid line in Figure 2.12a represents all galaxies in the simulation where the galaxy contained no initial bulge component and the hatched region is the number of galaxies in this set where the 2-component disk+point source model was the best fit. Figure 2.12b represents all of the galaxies which did contain an initial bulge component. The hatched region represents the galaxies in this set best fit with a 2-component disk+point source model or a 3-component disk+bulge+point source model. The cross hatched region represents those galaxies for which the 3-component model was the best fit.

It is clear that the 2-component disk+point source model detects point sources in galaxies with lower SNRIL values than the 3-component model. This result is expected since this model requires fewer fitted parameters than the 3-component

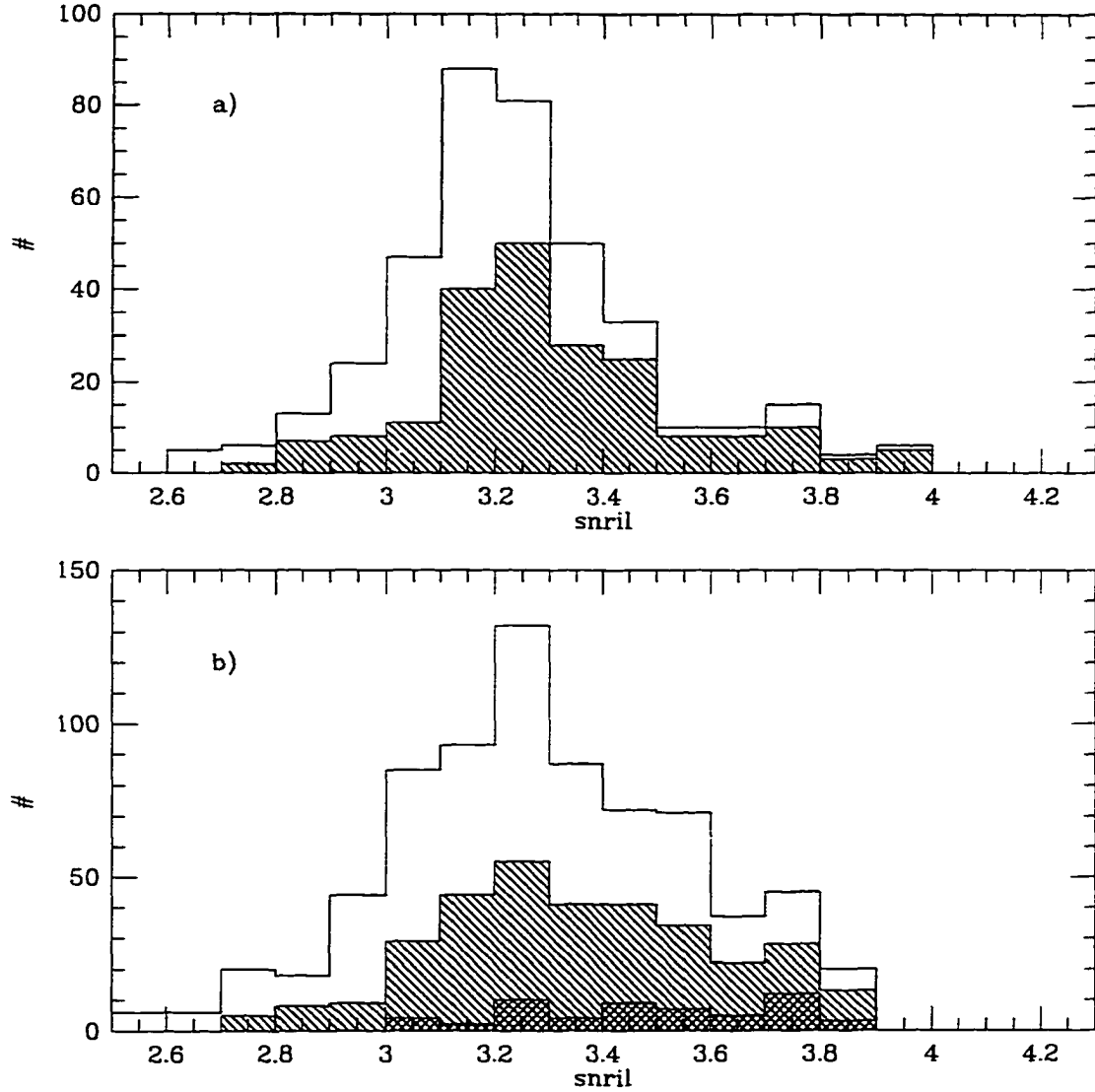


Figure 2.12 a) The histogram of all galaxies in the simulation containing no bulge component as a function of the SNRIL value. The hatched region represents those galaxies where a 2-component point source+disk model was the best fit thereby detecting the point source nucleus. b) The histogram of all galaxies in the simulation containing some bulge component as a function of the SNRIL value. The hatched region represents those galaxies where a 2-component point source+disk model or a 3-component point source+disk+bulge model was the best fit. The cross-hatched region represents those galaxies where the 3-component model was the best fit.

model. The 3-component model is much more incomplete overall than the 2-component disk+point source model. The 3-component model fits some galaxies down to $\text{SNRIL}=3.0$ while the 2-component disk+point source fits some down to $\text{SNRIL}=2.7$. To ensure that all galaxies in the sample can be fit with either the 2 or 3-component model, the limiting SNRIL value required for galaxies to be included in this study is 3.0. Setting the SNRIL value lower would introduce a bias against detecting point source nuclei in galaxies with significant bulge components and $\text{SNRIL}<3.0$.

The total number of galaxies in each of the 70 fields which have SNRIL values greater than or equal to 3.0 in one or both filters is 1033, an average of 13.5 galaxies per typical WFPC2 field (106 galaxies lie above this limit in the HDF). Table 2.2 shows the limiting apparent I magnitude and V magnitude corresponding to this SNRIL value in each field and the number of galaxies in each field in I above this limiting value.

2.7.2. Selected Galaxies Containing Nuclear Point Sources

The output image containing the model and residual for every galaxy in the survey was visually inspected to ensure that the model is correct and no obvious errors have occurred in the fitting process. The best fit model is then determined as the one with the lowest likelihood ratio value. The criteria for selecting a galaxy where the best model fit contains a point source component have been discussed in detail in the preceding section. Initially, the model must be the best fit, having a likelihood ratio between the point source and non-point source model greater than 50. The point source component must also comprise at least 1% of the total galaxy light to avoid spurious point source detections. After applying these criteria to the data, the galaxies in each field which are best fit with an additional point source

component are re-examined to determine if the point source location is near the nucleus of the host galaxy. This procedure is done to avoid fitting bright knots of star formation in the arms and disks of spiral galaxies or other noisy features. The point source is usually within $\simeq 0.2''$ (2 pixels in the WF chip) of the host galaxy center. Some, however, lie further from the galaxy center if the galaxy is very asymmetric. Occasionally, a galaxy is so irregular that it is difficult to determine the location of the nucleus and these galaxies were never selected as having point source nuclei because of this difficulty. A total of 10 galaxies in the Hubble Deep Field and 20 in the remaining 69 fields fall into this latter category.

We next apply the criteria for accurately measured nuclear point source components determined from the simulations in section 2.4.2. The following is a summary of the number of galaxies which contained a point source component in their best fit model but were rejected based on these criteria. Eight galaxies were removed because of non-convergence of the point source component in the model. Twenty-one were removed because the point source was detected in one filter while the other filter measured no point source (or a much smaller one) and the bulge/total luminosity ratio was greater by 0.25 than that measured in the other filter. Forty-nine were removed because the galaxy appeared to be elliptical-like (bulge-to-total ≥ 0.8) and the point source component had the same V-I color as the galaxy, indicating that the measured point source is likely a cuspy portion of the bulge.

After removing these galaxies from the selected sample we have a total of 8 galaxies in the Hubble Deep Field and 93 in the remaining 69 WFPC2 fields which are best fit with a galaxy model containing a nuclear point source component and meet all of the criteria described above. This selection results in direct detection

of $7.5\% \pm 2.7\%$ of the galaxies in the Hubble Deep Field and $10.0\% \pm 1\%$ of the galaxies in the remaining fields with nuclear point source components. Seventy-two of the point source nuclei were detected in both the V and I filter images, 8 were detected in the V image alone, and 21 were detected in the I image alone. Usually, the reason for non-detection in one filter is because the nucleus is too faint in that filter. However, in six cases the point source component did not converge properly in the other filter and the magnitude was therefore considered unreliable.

Figure 2.13 is a gray-scale I filter image of the selected galaxies sorted by magnitude of the point source component. The images are scaled in nuclear flux and are sorted in descending order of point source-to-total luminosity ratio so that the galaxies with the brightest relative point source nuclei are first. The spiral structure in many of the larger galaxies is clearly visible. Some of the nuclei are too faint to be detected by eye in this image; however, the range of sizes and galaxy types of the host galaxies can be seen. Figure 2.14 shows the point source magnitude vs. the integrated magnitude of the galaxy in I (a) and V (b)). The unresolved nuclear point sources range in magnitude from $27 \lesssim I \lesssim 21$. The faintest galaxies (fainter than $I \simeq 21.5$) are from the HDF. The error in the point source magnitude has been adjusted to reflect the expected error based on simulations in section 2.4.2. Most of the nuclei (87%) comprise less than 20% of the total galaxy light with 59% comprising less than 5%.

Table 2.3 lists the important fitted parameters for the 101 galaxies containing nuclear point sources. The table lists the ID number (1), the object name (2), the I magnitude of the galaxy model (3) and its error (4), natural log of the I filter half-light radius in arcseconds (5) and its error (6), the V-I galaxy color (7) and its error (8), the I Bulge-to-Total measurement (9), the I Point source-to-Total

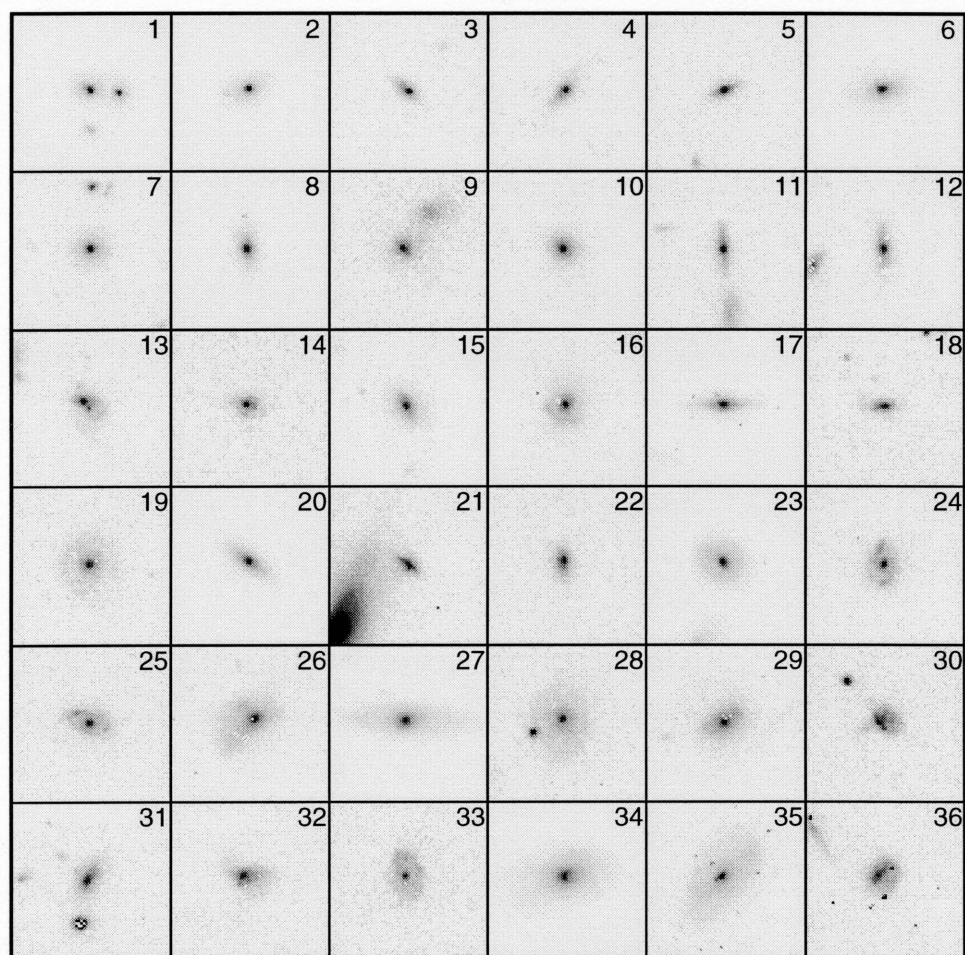
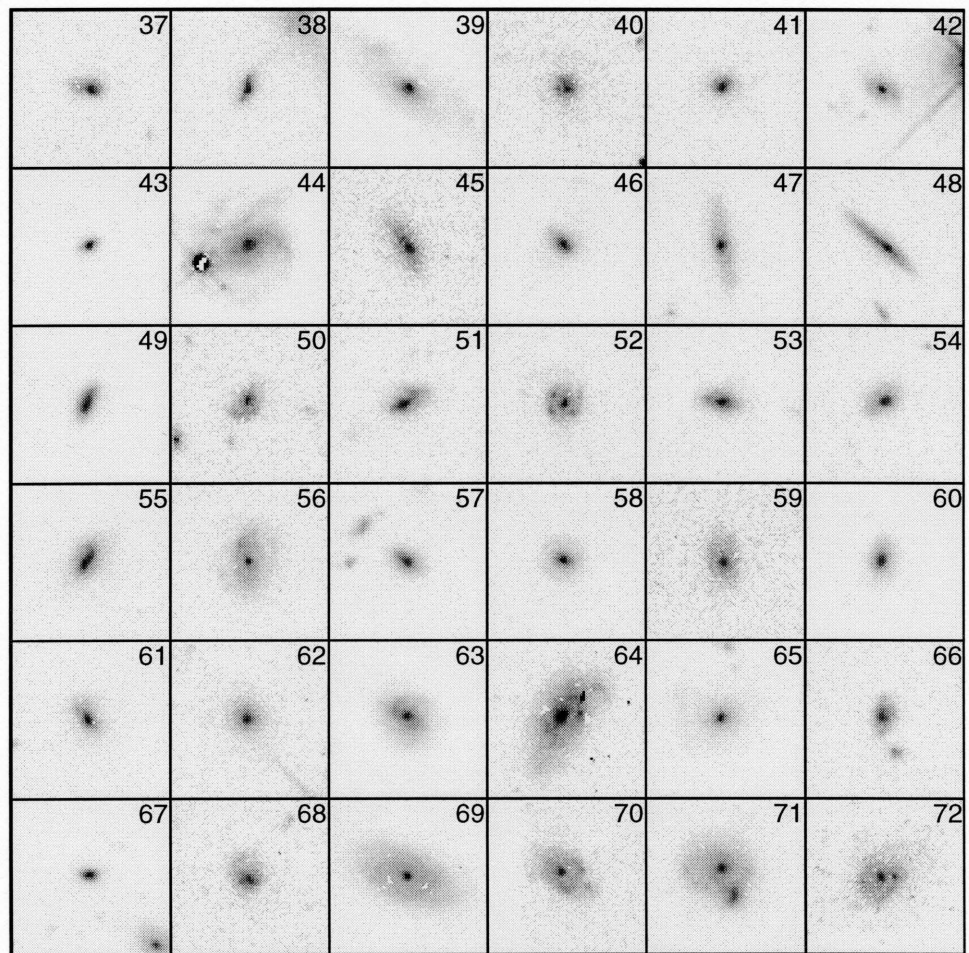
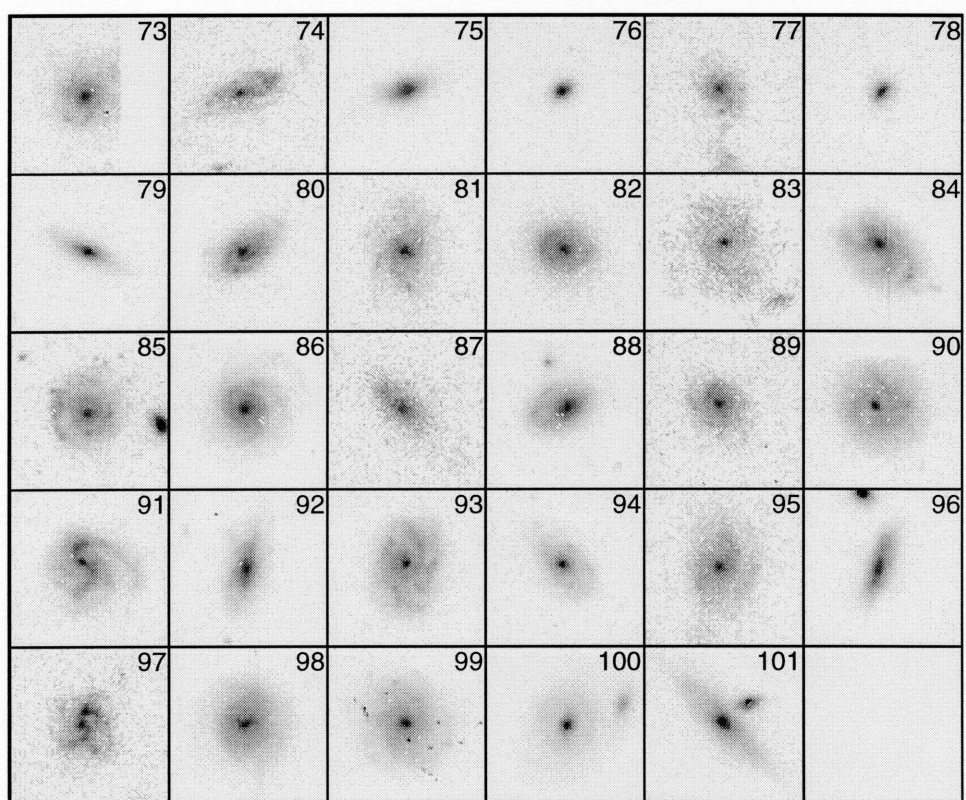


Figure 2.13 I band image of galaxies containing unresolved nuclear point sources down to 1% of the total galaxies light. The galaxies are arranged in descending order from the greatest point source-to-total luminosity ratio from left to right, top to bottom. The ID number is used to indentify each object throughout the paper.





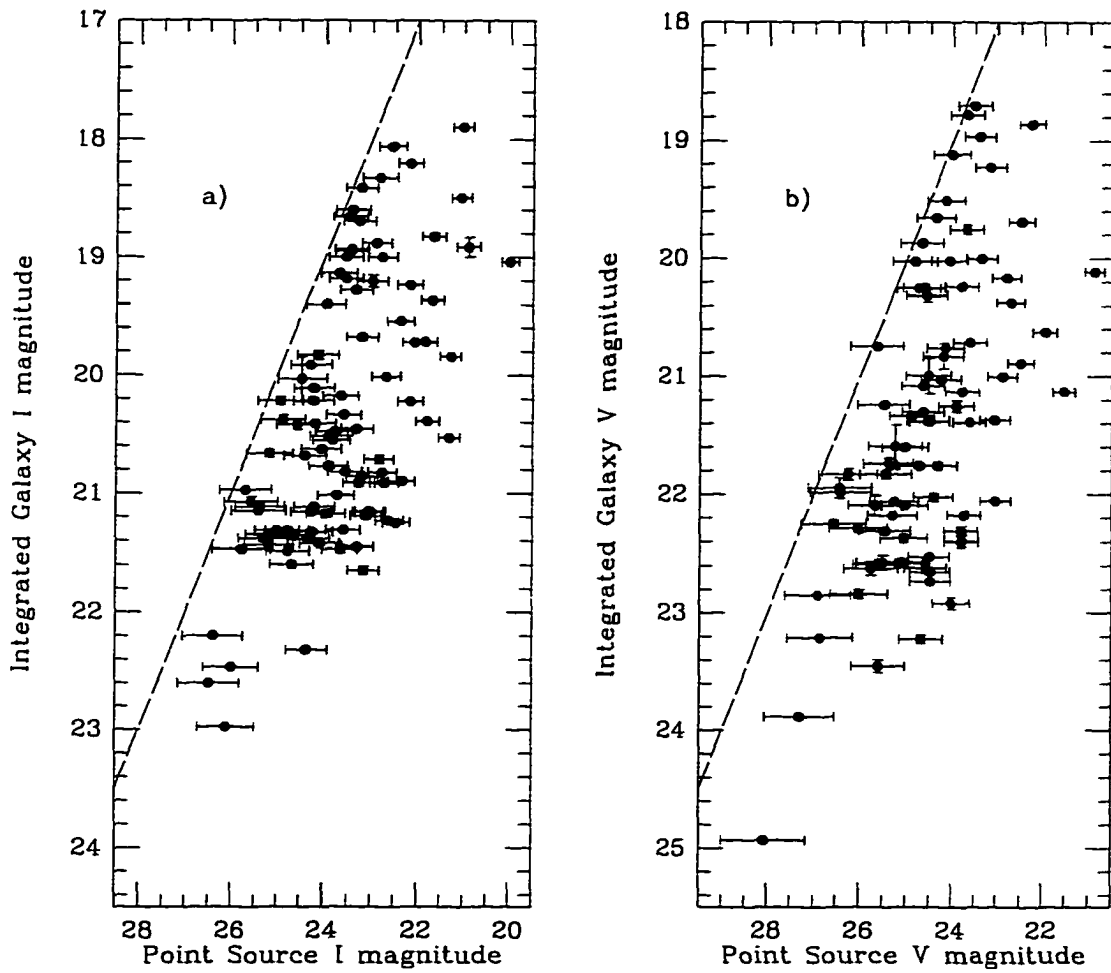


Figure 2.14 The point source nucleus magnitude vs. the integrated galaxy magnitude in a) I and b) V. The dashed line represents the locus where the point source is 1% of the total galaxy light.

measurement (10), the V Point source-to-Total measurement (11), and the V-I color of the point source (12) with its error (13). The error in the point source color reflects the empirically determined error of the point source magnitude from the simulations described in section 2.4.2. The object coordinates are given in Table.3.3.

The completeness in detecting point source galaxies can be determined based on the simulations of the previous section. Figures 2.10 and 2.11 give the completeness as a function of the point source-to-total luminosity ratio for galaxies with various $B/B+D$ measurements. These completeness estimates can be combined to determine the overall completeness of the survey in detecting point source nuclei as a function of the point source-to-total luminosity ratio. To do this, we weight the completeness estimates by the number of galaxies in the total survey with the corresponding $B/B+D$ measurement. Of the 1033 galaxies in the survey, 282 have $B/B+D=0$, 409 have $0 < (B/B+D) \leq 0.4$, 194 have $0.4 < (B/B+D) \leq 0.8$, and 148 have $0.8 < (B/B+D) \leq 1.0$. Combining the completeness estimates in Figures 2.10 and 2.11 weighted by the numbers of survey galaxies in each bin yields the overall completeness estimate for the survey illustrated in Figure 2.15. For nuclei comprising only a few percent of the galaxy light, we are $\sim 25\%$ complete in detecting these over the full range of galaxy types in our sample. For nuclei greater than 10% of the galaxy light, we are $\gtrsim 60\%$ complete. Most of the incompleteness stems from the inability to detect faint nuclei in galaxies with large or medium sized bulge components.

We can correct for the apparent incompleteness by applying these estimates to the number of point sources detected in each point source-to-total luminosity bin. For example, the total number of point source nuclei in our sample comprising

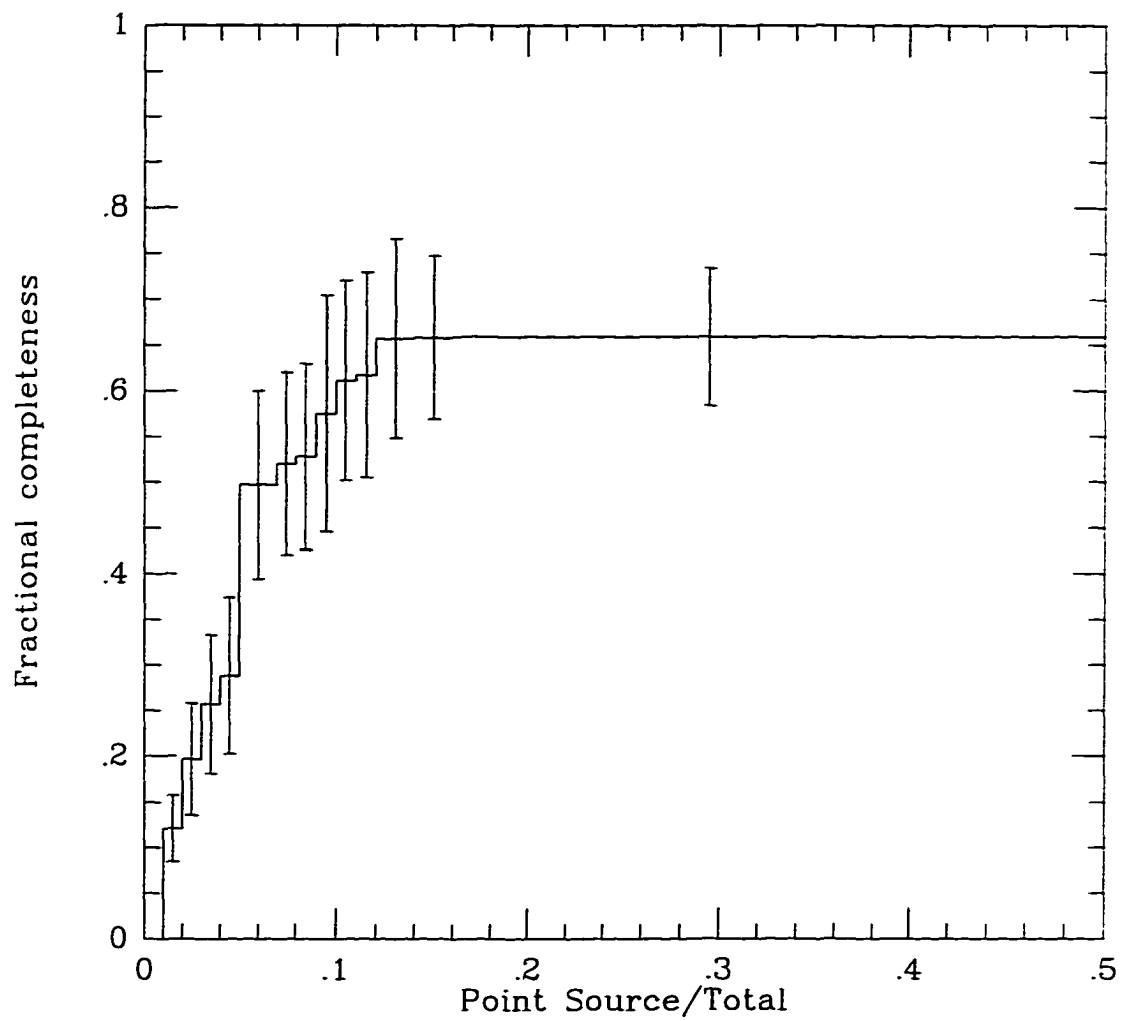


Figure 2.15 The overall completeness estimate for detecting nuclei in the survey galaxies as a function of the point source-to-total luminosity ratio.

between 1% and 2% of the total galaxy light is 19 ± 4.4 . The apparent completeness in this bin, according to Figure 2.15, is $12.1 \pm 3.6\%$. If we adjust our sample for this level of incompleteness, the total number of nuclear point sources in our survey could be as high as 157 ± 59 having point source-to-total luminosity ratios between 1% and 2%. If each bin is adjusted for incompleteness in this way, the fraction of all galaxies which contain nuclear point sources down to 1% of the galaxy light could be as high as $36.4 \pm 6.7\%$. Figure 2.16a illustrates how the fraction of galaxies containing unresolved nuclei varies as the limiting point source-to-total luminosity ratio changes. The solid line represents the uncorrected counts and the dashed line represents the corrected number counts according to the incompleteness estimates described above. The high level of incompleteness at the faint end (where the point source is 1-2% of the total galaxy light) causes the adjusted fraction of galaxies to increase sharply when extending the survey to these faint limits. Figure 2.16b shows the completeness adjustment factor as a function of point source-to-total luminosity ratio limit. At a limit of 5% this factor appears to level off at about 0.6. The behavior of the completeness adjustment factor indicates that the statistically significant point source-to-total luminosity ratio limit appears to be from $\sim 3\%$ to 5%. According to Figure 2.16a at this limit the total fraction of galaxies containing a nuclear point source component is $\sim 9\%$ to 16% corrected for incompleteness.

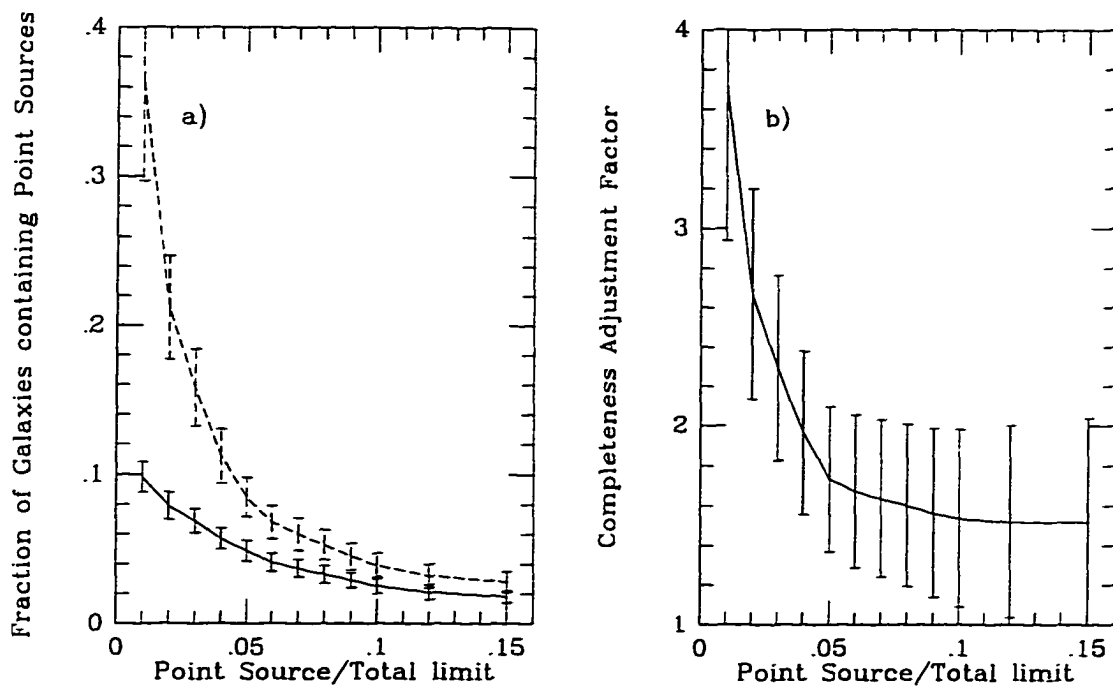


Figure 2.16 a) The fraction of total survey galaxies containing unresolved nuclei as a function of the limiting point source-to-total luminosity ratio. The dashed line represents this fraction after correcting for completeness according to Figure 2.15. b) The completeness adjustment factor as a function of the limiting point source-to-total luminosity ratio. This is the amount by which the fraction must be multiplied to correct for incompleteness.

Table 2.1. MDS Fields

Field Name	RA(J2000)	DEC(J2000)	Gal. lat.	V _#	V _{exp} (s)	I _#	I _{exp} (s)
uad01	0 15 47.76	-16 19 4.91	-76.40	2	1200	2	2000
uad00	0 15 55.35	-16 18 6.20	-76.40	2	1200	2	2000
ua400	0 24 53.64	-27 16 23.41	-84.10	4	8000	4	8000
ubz01	0 50 32.51	-52 7 25.29	-65.00	2	1200	2	2000
ueh00	0 53 23.16	12 33 57.72	-50.30	3	5400	3	6300
ueh02	0 53 36.60	12 49 49.36	-50.04	2	3300	2	4200
ua-30	0 58 6.77	-28 11 40.68	-88.18	3	3900	5	4900
ua-00	1 2 26.49	-27 11 52.82	-87.55	2	2100	2	4200
ua-01	1 4 36.03	-27 5 17.14	-87.07	3	8700	4	10700
ujh01	1 9 3.47	35 36 25.18	-27.13	1	1200	2	4200
ubi01	1 9 59.79	-2 27 23.78	-64.93	2	3300	3	6300
ubi00	1 10 3.01	-2 26 22.81	-64.91	1	1200	2	4200
uci10	1 24 42.43	3 51 27.63	-57.99	3	4800	4	10800
ufj00	2 7 5.82	15 25 18.34	-43.66	1	1200	2	4200
ugk00	2 38 51.59	16 44 38.24	-38.97	1	2700	2	5400
udm00	2 42 39.46	0 48 49.31	-51.32	1	1200	2	3000
udm10	2 42 51.73	0 4 25.04	-51.95	4	4000	3	5400
ucs01	2 56 22.03	-33 22 25.38	-62.42	2	1500	2	4200
uem00	3 5 3.21	0 11 13.07	-48.11	2	2400	5	6600
uim01	3 55 31.39	9 43 31.97	-32.15	6	3600	10	6600
uko01	4 56 45.47	3 52 40.82	-23.28	1	1200	2	4200
uqk11	7 24 46.55	60 31 2.33	27.41	1	1000	5	3100
uop00	7 50 47.13	14 40 44.23	19.63	5	7200	2	4200
urp03	8 47 21.45	17 57 29.81	33.42	1	1200	2	3000
urp01	8 47 24.09	17 56 22.90	33.42	1	600	1	2400
usp00	8 54 16.12	20 3 41.88	35.68	2	3300	2	4200

Table 2.1—Continued

Field Name	RA(J2000)	DEC(J2000)	Gal. lat.	V _#	V _{exp} (s)	I _#	I _{exp} (s)
ust01	10 5 16.93	-7 47 35.05	36.74	1	1200	3	2380
ust00	10 5 46.34	-7 41 30.32	36.90	10	16500	11	23100
uui00	11 42 4.74	71 37 43.89	44.47	3	5400	3	6300
uzp01	11 50 29.79	28 48 29.63	76.45	2	3300	3	6300
uyj00	11 53 25.21	49 31 12.91	64.98	1	300	3	2700
uzk02	12 11 13.10	39 26 56.01	75.11	1	600	3	7200
uzx00	12 30 16.46	12 21 47.28	74.42	3	4500	1	2100
uzx07	12 30 51.00	12 19 2.95	74.42	4	5200	3	2700
uzx01	12 30 54.20	12 19 5.56	74.43	5	3480	4	6200
uxy00	12 32 31.57	-2 21 48.59	60.16	1	1200	2	4200
uxy10	12 36 38.87	0 41 54.92	61.95	3	980	5	3780
HDF	12 36 49.40	62 12 58.00	54.83	103	1051	58	2137
uzy00	12 38 14.09	11 52 30.62	74.44	1	1200	2	2700
uzy01	12 38 15.75	11 51 18.24	74.42	2	3000	2	2700
uwy02	12 40 22.82	-11 31 29.74	51.25	6	11700	5	9600
urz00	12 53 1.85	-29 14 21.44	33.63	3	5400	4	8400
uz-00	13 0 23.61	28 20 13.19	87.68	2	1200	2	2000
uzd10	13 55 18.34	40 20 30.58	71.33	1	3500	2	6100
uy000	14 16 18.08	11 32 22.72	64.70	4	6000	4	6900
u26x9	14 17 23.69	52 25 13.01	59.77	4	700	4	1000
u26x8	14 17 30.22	52 26 22.81	59.79	4	700	4	1000
u26x7	14 17 36.76	52 27 32.69	59.82	4	700	4	1000
u26x6	14 17 49.85	52 29 52.30	59.87	4	700	4	1000
u26x5	14 17 56.40	52 31 2.10	59.89	4	700	4	1000
uy400	14 34 57.79	25 11 45.41	66.73	6	5200	6	6000
uy402	14 35 16.92	24 59 4.00	66.62	2	1400	3	5400

Table 2.1—Continued

Field Name	RA(J2000)	DEC(J2000)	Gal. lat.	V _#	V _{exp} (s)	I _#	I _{exp} (s)
uy401	14 35 33.07	25 18 15.87	66.62	4	2400	8	8000
ux400	15 19 41.20	23 52 5.45	56.51	2	3300	4	7500
ux401	15 19 54.97	23 44 46.01	56.43	2	3300	3	6000
uvd01	15 43 23.69	53 52 46.40	48.77	3	9000	2	6000
ut201	16 1 12.34	5 36 2.81	40.06	6	3600	12	12000
ut200	16 1 27.39	5 23 55.60	39.90	6	5200	6	6000
usa02	17 12 23.15	33 35 49.31	34.25	3	5400	3	6300
usa01	17 12 23.94	33 36 3.92	34.25	3	5400	3	6300
usa00	17 12 24.63	33 36 15.75	34.25	3	5400	3	6300
uqa02	17 36 22.50	28 0 58.69	27.84	2	1200	2	2000
uqa01	17 36 38.64	28 4 8.78	27.80	2	1200	4	2280
uj000	19 39 22.86	-46 13 46.18	-27.20	1	1200	2	4500
uj700	19 40 40.22	-69 16 1.80	-29.58	3	5400	3	6300
umd08	21 50 34.86	28 49 41.63	-19.23	4	1200	1	2400
umd09	21 50 38.45	28 55 56.53	-19.16	2	2400	2	4200
umd05	21 51 7.21	29 0 0.46	-19.18	1	1200	2	3900
umd0a	21 51 13.08	29 0 4.57	-19.20	2	3300	3	8700
uec00	23 4 28.61	3 4 38.17	-50.28	1	1200	2	3000

Table 2.2. Field Limiting Magnitude

Field Name	I_{lim}	V_{lim}	# of Galaxies Above Limit
u26x5	21.23	22.03	13
u26x6	21.38	22.07	12
u26x7	21.33	21.82	16
u26x8	21.38	21.90	22
u26x9	21.60	22.04	21
ua400	21.93	22.58	24
ua-00	21.55	21.74	27
ua-01	21.98	22.78	22
ua-30	22.03	22.49	19
uad00	20.13	21.09	3
uad01	20.68	20.06	4
ubi00	20.85	20.78	6
ubi01	21.01	21.45	20
ubz01	20.83	21.20	8
uci10	21.88	22.15	18
ucs01	21.25	21.50	13
udm00	21.06	22.09	3
udm10	21.65	21.78	14
uec00	21.08	21.40	9
ueh00	20.99	21.59	15
ueh02	21.31	22.23	23
uem00	21.37	21.79	14
ufj00	21.37	21.40	23
ugk00	21.02	21.43	8
uhdfk	23.47	24.16	106
uim01	20.98	21.51	14

Table 2.2—Continued

Field Name	I_{lim}	V_{lim}	# of Galaxies Above Limit
uj000	21.41	21.20	11
uj700	21.55	22.13	9
ujh01	21.24	21.33	10
uko01	21.35	21.36	12
umd05	21.51	21.51	6
umd08	21.02	21.41	12
umd09	21.20	22.00	12
umd0a	21.95	22.10	22
uop00	21.34	22.05	9
uqa01	20.71	21.33	4
uqa02	21.23	21.27	3
uqk11	21.15	21.30	16
urp01	21.13	20.43	8
urp03	20.81	21.45	12
urz00	22.15	22.34	24
usa00	21.88	22.74	11
usa01	21.76	22.39	7
usa02	21.73	22.58	9
usp00	21.20	21.84	8
ust00	22.21	23.12	17
ust01	20.44	21.55	8
ut200	21.70	22.32	15
ut201	21.80	22.22	21
uui00	21.57	22.52	32
uvd01	21.77	23.00	18
uwy02	22.10	23.01	21

Table 2.2—Continued

Field Name	I_{lim}	V_{lim}	# of Galaxies Above Limit
ux400	21.61	21.91	24
ux401	21.49	21.95	11
uxy00	21.43	21.67	11
uxy10	21.08	21.03	7
uy000	21.59	22.32	16
uy400	21.47	22.13	8
uy401	21.90	21.88	15
uy402	21.53	21.47	2
uyj00	21.02	20.19	15
uz-00	20.76	21.30	4
uzd10	21.45	22.12	21
uzk02	21.83	21.17	17
uzp01	21.72	22.03	22
uzx00	20.87	22.24	22
uzx01	21.38	22.01	8
uzx07	20.54	22.10	8
uzy00	20.69	21.19	4
uzy01	20.72	21.89	4

Table 2.3. Model Parameters for Galaxies Containing Unresolved Nuclei

ID#	Name	I_{mag}	σ_I	hlr	σ_{hlr}	V-I	σ_{V-I}	B/ T_I	P/ T_I	P/ T_V	V- I_P	σ_{V-I}
1	ua400-7	20.530	0.008	-0.767	0.020	0.602	0.011	0.000	0.485	0.687	0.224	0.333
2	uwy02-4	19.041	0.003	-0.367	0.006	1.071	0.004	0.000	0.414	0.489	0.890	0.285
3	ua-30-13	21.249	0.012	-1.016	0.024	0.810	0.016	0.000	0.333	0.410	0.584	0.436
4	ust01-11	19.760	0.017	-0.937	0.039	0.867	0.021	1.000	0.000	0.293
5	u26x9-20	21.231	0.011	-1.049	0.019	1.995	0.035	0.000	0.285	0.262	2.086	0.555
6	uy401-12	20.390	0.007	-0.605	0.013	0.980	0.017	0.000	0.276	0.214	1.256	0.413
7	ut200-28	20.897	0.017	-0.687	0.026	1.416	0.039	0.000	0.264	0.256	1.449	0.478
8	ufj00-13	19.841	0.006	-0.857	0.012	1.047	0.013	0.000	0.264	0.230	1.197	0.371
9	udm10-24	21.646	0.033	-1.254	0.043	1.275	0.059	0.000	0.250	0.366	0.861	0.528
10	umd0a-47	20.912	0.008	-1.013	0.014	1.709	0.040	0.000	0.190	0.165	1.862	0.549
11	ua400-26	21.448	0.013	-0.534	0.020	1.754	0.028	0.000	0.184	0.000
12	uvd01-26	21.157	0.012	-0.522	0.020	1.368	0.018	0.000	0.183	0.162	1.500	0.550
13	ua-01-10	21.153	0.011	-0.731	0.014	1.502	0.024	0.000	0.175	0.187	1.430	0.550
14	uzz01-37	21.190	0.021	-0.890	0.032	1.209	0.051	0.000	0.173	0.279	0.690	0.511
15	ut201-18	20.827	0.009	-0.763	0.014	1.351	0.026	0.000	0.169	0.241	0.966	0.489
16	uvd01-14	20.221	0.009	-0.505	0.012	1.169	0.013	0.000	0.167	0.130	1.441	0.458
17	uzz00-3	18.912	0.083	-0.498	0.084	1.257	0.084	0.291	0.160	0.089	1.894	0.402
18	usa00-35	22.319	0.020	-1.084	0.030	0.416	0.024	0.000	0.154	0.202	0.121	0.623
19	ueh02-14	20.715	0.034	-0.244	0.037	-0.246	0.358	0.000	0.144	0.000
20	umd0a-25	19.717	0.012	-0.593	0.023	1.286	0.014	0.335	0.141	0.178	1.033	0.410
21	uui00-31	21.469	0.028	-0.789	0.036	0.844	0.030	0.317	0.133	0.055	1.803	0.669
22	u26x6-11	21.311	0.015	-0.978	0.025	2.144	0.056	0.000	0.124	0.139	2.020	0.676
23	usa00-9	19.364	0.004	-0.502	0.000	1.007	0.006	0.150	0.118	0.117	1.016	0.392
24	uzp01-19	20.859	0.016	-0.305	0.017	1.169	0.036	0.000	0.117	0.112	1.216	0.554
25	umd05-46	20.913	0.028	-0.283	0.029	0.684	0.189	0.000	0.116	0.035	1.985	0.674
26	ueh02-4	19.720	0.014	-0.087	0.015	0.336	0.095	0.000	0.115	0.000
27	uy401-4	18.498	0.008	0.512	0.011	1.194	0.021	0.463	0.094	0.077	1.411	0.366
28	uj700-29	20.014	0.036	0.219	0.030	1.240	0.059	0.152	0.000	0.087
29	uvd01-12	20.014	0.007	-0.414	0.009	1.119	0.009	0.026	0.086	0.088	1.094	0.488
30	uzp01-24	21.422	0.017	-0.850	0.021	0.949	0.032	0.000	0.086	0.084	0.975	0.652
31	umd05-37	21.016	0.015	-0.793	0.020	0.742	0.029	0.000	0.082	0.094	0.594	0.579
32	u26x5-6	20.819	0.014	-0.822	0.018	0.941	0.020	0.000	0.080	0.065	1.166	0.596
33	uy400-16	21.172	0.031	0.021	0.028	1.455	0.062	0.000	0.078	0.056	1.815	0.703
34	ust00-8	19.541	0.014	-0.679	0.018	1.173	0.021	0.627	0.074	0.070	1.233	0.467
35	uzz00-4	18.827	0.026	0.580	0.021	1.177	0.028	0.079	0.074	0.046	1.693	0.432
36	uzz00-20	20.454	0.016	-0.665	0.018	0.931	0.019	0.000	0.073	0.057	1.200	0.564
37	u26x7-18	21.325	0.017	-0.904	0.022	1.256	0.034	0.035	0.069	0.093	0.932	0.666
38	u26x8-23	21.384	0.015	-0.914	0.020	1.187	0.023	0.000	0.067	0.097	0.785	0.669
39	uzd10-6	19.236	0.011	0.362	0.011	1.004	0.017	0.360	0.067	0.038	1.620	0.471
40	u26x9-25	21.598	0.028	-0.877	0.032	1.353	0.055	0.000	0.059	0.000
41	u26x6-9	21.118	0.018	-1.052	0.022	0.951	0.026	0.123	0.059	0.053	1.067	0.674
42	ust00-27	21.157	0.008	-0.584	0.009	1.430	0.019	0.129	0.058	0.064	1.323	0.701
43	uhdfk-106	22.976	0.009	-1.739	0.015	1.954	0.023	0.091	0.056	0.055	1.974	1.113
44	umd09-4	17.900	0.006	0.591	0.005	0.963	0.012	0.000	0.056	0.044	1.225	0.354
45	urp03-14	20.770	0.024	-0.153	0.025	0.608	0.038	0.000	0.056	0.055	0.628	0.614
46	uxy10-6	20.276	0.010	-1.083	0.010	0.753	0.019	0.173	0.000	0.052

Table 2.3—Continued

ID#	Name	l_{mag}	σ_l	hlr	σ_{hlr}	V-I	σ_{V-I}	B/T _I	P/T _I	P/T _V	V-I _P	σ_{V-I}
47	uui00-17	20.335	0.014	0.145	0.017	1.270	0.024	0.167	0.050	0.043	1.434	0.623
48	uci10-11	20.551	0.011	0.108	0.010	0.751	0.018	0.000	0.049	0.046	0.820	0.601
49	uhdfk-36	21.484	0.004	-0.846	0.005	0.950	0.006	0.000	0.049	0.000
50	u26x8-31	21.355	0.034	-0.461	0.031	1.219	0.069	0.000	0.049	0.067	0.879	0.721
51	ufj00-17	20.477	0.011	-0.539	0.013	0.607	0.019	0.000	0.048	0.038	0.861	0.604
52	u26x7-10	20.519	0.016	-0.496	0.016	1.224	0.048	0.000	0.045	0.035	1.497	0.665
53	uzk02-5	20.630	0.008	-0.742	0.012	0.435	0.022	0.000	0.043	0.000
54	usa02-34	21.318	0.021	-0.751	0.023	0.776	0.026	0.173	0.042	0.067	0.269	0.689
55	uui00-11	20.176	0.008	-0.617	0.009	0.588	0.009	0.000	0.041	0.044	0.511	0.558
56	uim01-9	19.678	0.024	0.213	0.017	0.637	0.059	0.000	0.039	0.020	1.362	0.568
57	uhdfk-68	22.465	0.010	-0.936	0.013	1.418	0.021	0.000	0.039	0.043	1.312	0.978
58	ua-01-9	20.852	0.016	-0.860	0.021	1.242	0.086	0.400	0.000	0.037
59	usp00-10	21.198	0.016	-0.266	0.000	0.637	0.035	0.123	0.000	0.036
60	uhdfk-32	21.315	0.004	-0.922	0.006	0.457	0.014	0.247	0.034	0.000
61	u26x7-7	20.685	0.017	-0.685	0.020	0.653	0.021	0.279	0.033	0.038	0.500	0.657
62	umd0a-63	21.437	0.028	-0.711	0.033	0.398	0.056	0.158	0.032	0.017	1.085	0.829
63	uhdfk-17	20.409	0.003	-0.363	0.003	1.181	0.006	0.000	0.031	0.000
64	usp00-3	19.001	0.008	0.344	0.005	1.022	0.017	0.027	0.031	0.024	1.300	0.513
65	uqk11-6	19.203	0.052	0.386	0.102	1.628	0.120	0.933	0.031	0.045	1.223	0.557
66	ut201-37	21.348	0.014	-0.739	0.016	0.903	0.030	0.000	0.030	0.019	1.399	0.875
67	uhdfk-63	22.603	0.007	-1.628	0.010	0.611	0.009	0.000	0.028	0.035	0.369	0.974
68	ua-30-20	21.381	0.027	-0.759	0.028	0.909	0.045	0.000	0.027	0.032	0.725	0.814
69	ugk00-1	18.206	0.008	0.572	0.006	0.762	0.017	0.000	0.026	0.017	1.223	0.444
70	u26x9-8	20.217	0.023	0.043	0.019	0.751	0.061	0.000	0.025	0.000
71	u26x8-7	18.880	0.011	0.279	0.008	0.820	0.017	0.000	0.025	0.000
72	ust01-7	19.280	0.017	-0.068	0.016	0.906	0.030	0.000	0.024	0.000
73	uj000-28	20.111	0.019	-0.109	0.018	0.303	0.049	0.000	0.023	0.000
74	u26x7-14	20.417	0.042	0.500	0.027	0.652	0.166	0.000	0.022	0.000
75	uhdfk-46	22.199	0.007	-1.351	0.007	0.650	0.009	0.000	0.021	0.024	0.505	0.969
76	usa01-34	21.149	0.008	-1.360	0.013	1.033	0.012	0.000	0.020	0.057	-0.104	0.799
77	ut201-33	21.118	0.033	-0.216	0.029	0.829	0.093	0.000	0.020	0.016	1.071	0.875
78	uy400-15	21.469	0.017	-1.178	0.018	1.372	0.038	0.148	0.019	0.054	0.238	0.884
79	uy000-14	19.829	0.035	-0.174	0.042	1.415	0.040	0.597	0.019	0.020	1.359	0.699
80	ua400-8	19.913	0.008	-0.054	0.008	0.833	0.012	0.000	0.018	0.011	1.368	0.711
81	urp03-8	19.488	0.006	0.293	0.007	0.766	0.031	0.191	0.000	0.018
82	uqa01-21	19.183	0.008	-0.818	0.008	0.846	0.014	0.000	0.018	0.012	1.286	0.608
83	uj000-20	20.034	0.190	0.184	0.097	0.048	0.190	0.000	0.017	0.000
84	usa00-5	18.945	0.007	0.259	0.006	0.569	0.009	0.000	0.016	0.014	0.714	0.544
85	ust00-23	20.667	0.030	0.136	0.020	1.755	0.042	0.000	0.016	0.000
86	ujh01-2	18.329	0.005	-0.088	0.006	0.790	0.010	0.002	0.016	0.011	1.197	0.556
87	u26x6-6	21.076	0.041	-0.690	0.033	-0.026	0.042	0.000	0.016	0.000
88	ux400-7	18.932	0.003	-0.203	0.004	0.763	0.006	0.000	0.016	0.000
89	uko01-25	20.378	0.036	0.040	0.028	0.617	0.155	0.000	0.016	0.039	-0.350	0.695
90	ueh00-2	18.065	0.016	0.565	0.010	0.719	0.023	0.000	0.016	0.011	1.126	0.476
91	u26x8-5	19.000	0.010	0.1209	0.008	0.716	0.016	0.000	0.015	0.000
92	urx00-8	19.401	0.005	-0.087	0.005	0.853	0.007	0.030	0.015	0.016	0.783	0.620
93	uem00-4	18.695	0.011	0.490	0.008	1.177	0.022	0.000	0.015	0.012	1.419	0.580

Table 2.3—Continued

ID#	Name	I_{mag}	σ_I	hlr	σ_{hlr}	V-I	σ_{V-I}	B/T _I	P/T _I	P/T _V	V-I _P	σ_{V-I}
94	uwy02-5	19.135	0.010	-0.050	0.011	0.686	0.010	0.199	0.015	0.000
95	uzz07-4	18.955	0.025	0.488	0.022	0.703	0.028	0.047	0.000	0.013
96	uhdfk-27	20.972	0.004	-0.049	0.005	1.015	0.004	0.000	0.013	0.017	0.724	0.872
97	u26x8-12	20.219	0.031	0.155	0.020	1.223	0.078	0.000	0.013	0.000
98	uui00-3	18.417	0.005	0.076	0.005	0.812	0.006	0.012	0.012	0.027	-0.068	0.477
99	umd08-13	18.085	0.004	0.222	0.001	0.620	0.018	0.059	0.000	0.012
100	usa02-6	18.658	0.016	0.403	0.015	0.745	0.027	0.204	0.012	0.000
101	uim01-4	18.603	0.019	0.578	0.020	1.155	0.041	0.530	0.012	0.027	0.275	0.524

CHAPTER 3

SPECTROSCOPY AND REDSHIFTS

Ground-based spectroscopic follow-up for the galaxies imaged with HST is an important part of the science objectives of the Medium Deep Survey. Spectra allow us to determine redshifts for the host galaxies for construction of an accurate luminosity function of the unresolved nuclei. Spectra also allow us to associate detected emission lines with morphological properties and confirm the identification of LLAGNs or starburst nuclei for the brightest candidates. Additional spectra of MDS galaxies in the field were obtained to address other scientific questions about the nature of moderately redshifted galaxies. For example, these redshifts allow us to assign distances to morphologically classified galaxies to see how the mix of Hubble types changes with cosmic time (Im et al. 1996). Also, the redshifts of additional MDS galaxies allow us to pursue the evolution of effective radii of ellipticals and scale lengths of disks with cosmic time (Mutz et al. 1994). The reader is referred to the noted papers as these topics will not be discussed here. However, the database of other MDS galaxies is used in another way which is of interest to this project. Understanding how morphological and photometric properties of galaxies vary with redshift can help us to estimate reasonably

redshifts for those candidates for which adequate spectra are not obtained. This “photometric redshift” technique is described in detail in the last section of this chapter.

3.1. Spectroscopy and Data Reduction

Spectra were obtained with the Kitt Peak 4-meter telescope using the R. C. Spectrograph and Cryogenic Camera. The detector is a dedicated Loral (Ford) 800x1200 pixel device with relatively good cosmetics in a fast (f/1) camera-dewar combination. Total system throughput (telescope + spectrograph + CCD) is typically 20%. This instrument allows for use of multi-slit masks so that several targets can be exposed at the same time. For each field, 1 to 3 masks were designed based on astrometry taken from the WFPC2 images. Each mask exposed between 4 and 10 galaxies with a typical mask exposing 6 galaxy targets at once. Using this technique, most galaxies in each field could be observed down to a limiting magnitude of $I \sim 21.0$.

Observations of WFPC2 imaged galaxies were made during observing runs in 1994 October, 1995 April, 1996 January, 1996 July, and 1996 September. A total of 19 nights at the 4 meter telescope was allocated for this project during these 5 observing runs. Due to poor weather, 6 nights were lost yielding a total of 13 nights. Grism number 650 was used during the October '94 run while Grism number 770 was used for the subsequent runs since the longer wavelength range was desirable for observing emission lines of higher redshift galaxies. The redshift range and resolution (using a 2.5" slit) for each grism as well as the gain in units of e^-/ADU and readnoise in electrons for each observing run is listed in Table 3.1. The redshift range allows for coverage of the H&K Calcium lines and 4000Å

blanketing break, 3727 Å [OII], 5007/4959 Å [OIII], and several other emission and absorption features out to $z \approx 0.8$. However, the actual redshift range detectable for each object varies somewhat due to the galaxy position within the focal plane.

Typically, 2 to 3 one-hour exposures were required for each multi-slit mask to achieve a signal-to-noise of at least 10 for a galaxy of $I \approx 20.0$. Calibration images consisted of quartz flats obtained for each mask, HeNeAr lamp images obtained before and after each mask observation, and bias frames obtained at the beginning of each night.

The data were reduced using several IRAF routines outlined in the manual “Multi-Slits at Kitt Peak” (DeVeney et al. 1996). At least 20 bias frames were averaged together for each night of observing and were subtracted from all images taken that night using CCDPROC. Bad CCD columns were removed from all images by interpolation using FIXPIX. Quartz lamp images for each individual mask were averaged together using FLATCOMBINE. Next, APFLATTEN was used to flatten the flat field for each mask leaving an image which represents the pixel-to-pixel gain variations in the CCD. The resulting flat field no longer has spatial (slit-function) information. This is appropriate for the quartz lamp

Table 3.1 Spectroscopic Observing Run Summary

Date	Grism #	λ range (Å)	Å/pixel	Res. (Å)	Gain	Rd Noise
Oct 94	650	4000-6800	3.2	12	1.5	15
Apr 95	770	4300-8500	4.3	15	1.5	15
Jan 96	770	4300-8500	4.3	15	1.5	15
Jul 96	770	4300-8500	4.3	15	1.5	15
Sep 96	770	4300-8500	4.3	15	0.8	15

exposures of multi-slit masks since the short slit length ($\sim 10''$ to $20''$) doesn't reveal much slow variation along the spatial direction. Each aperture is fit with an appropriate polynomial to remove the overall shape of the quartz lamp flat. Typically, this was a legendre polynomial with order = 20 to 30. The flat field correction was then applied to each mask image (object images as well as comparison lamp images) using CCDPROC.

Before extracting the spectra, the individual object frames for each mask were usually combined using IMCOMBINE. In some cases, if the telescope had been moved slightly between exposures, each object frame was extracted separately. The comparison lamp frames for each mask were also combined before extracting. To extract the object spectra, APALL was used to set and fit the background (sky region) of each aperture as well as setting the object region. The spectra were traced and interactively fit using this task. The resulting image contains the object spectrum for each aperture with variance weighting, the object spectrum without variance weighting, the sky spectrum for each aperture, and the error spectrum for each aperture. The HeNeAr comparison images are then extracted using the APSUM task with the object apertures set identically to those in the the object image extractions. The emission lines in each of the comparison spectra are then identified and this dispersion solution is applied to the appropriate aperture object spectrum in each of the images using DISPCOR.

3.2. Redshift Determination

For each spectrum with obvious emission lines and/or absorption features, a redshift estimate was first determined by measuring the emission wavelengths of two or more features and comparing them with the known rest wavelengths.

Cross-correlation with a template galaxy spectrum containing similar features was used to accurately determine the true redshift for the object. We used FXCOR in IRAF to do the cross-correlation. The galaxy template spectra are from Kennicutt (1992) for various galaxy types. At least 5 different templates were employed depending on the galaxy type for which the redshift was being determined. A parabolic fit to the peak in the cross-correlation function determined the redshift and provided a formal error in the redshift determination based upon this fit.

In some cases only one emission or absorption line was obvious. If the redshift determination was based on only one line or two weak features, it is marked as uncertain (?) in the redshift list. Some galaxy spectra contained adequate signal but no obvious emission or absorption features were noted at all. The cross-correlation technique was also employed with these spectra to determine if weaker absorption or emission features could be detected. In these cases, if a redshift was determined for the spectra, it was marked as very uncertain (??) in the final redshift list.

A total of 253 objects were observed through slitlet masks over the 5 observing runs. Of these objects, 136 had enough signal present in the spectra to detect emission lines or possible absorption features so that a redshift could be determined. This yields a success rate of 54% in obtaining MDS galaxy redshifts. The majority of these galaxies for which redshifts were determined are non-nuclear point source galaxies.

As discussed in the previous chapter, a total of 101 galaxies were found to contain nuclear point sources, including galaxies from the Groth strip and HDF. The spectroscopic follow-up pursued in this study includes only MDS fields. Other groups have obtained spectroscopic follow-up for the non-MDS fields which we use

to complement our redshift survey.

Of the 101 galaxies containing nuclear point sources, 77 are in MDS fields with the remaining 24 observed in the Groth strip and HDF. Of the 77 galaxies selected from the MDS fields which contain nuclear components, 35 have been observed through slitlets at the 4 meter. Figure 3.1 shows the 35 spectra where the prominent absorption and/or emission features have been indicated. Adequate signal along with emission or absorption features were detected in 29 of these spectra allowing their redshifts to be determined. The dashed line is the arbitrarily scaled error spectrum indicating regions where night sky lines affected the object spectrum. The redshift is shown in the upper left corner of each spectrum under the object name. Uncertain redshifts are indicated with question marks. We also show in the upper right corner an ID number corresponding to the ID number in Figure 2.13 allowing each spectrum to be matched to its image. The spectra are arranged in order of decreasing contribution of the nucleus to the galaxy light.

There are on average 1.2 galaxies containing unresolved nuclei per WFPC2 field. For every MDS field observed at the 4 meter, slitlets were placed on those galaxies containing nuclear components with the remainder placed on other relatively bright ($I \lesssim 21.0$) galaxies in the field. Because of the sparseness of the nucleated galaxies in each field, it was difficult to obtain spectroscopic observations for the entire sample of 77 galaxies in 13 nights of 4 meter time with the typical total exposure time per field being 3 hours. As mentioned above, only 35 of the compact nuclei galaxies were observed and 29 (38% of the 77 galaxies) yielded good spectra for redshift determination. We then include the compact nuclei galaxies from the HDF (Cohen et al. 1996) and Groth strip (Koo et al. 1996) for which redshifts are taken from the literature. Of the 24 compact nuclei galaxies in these 2

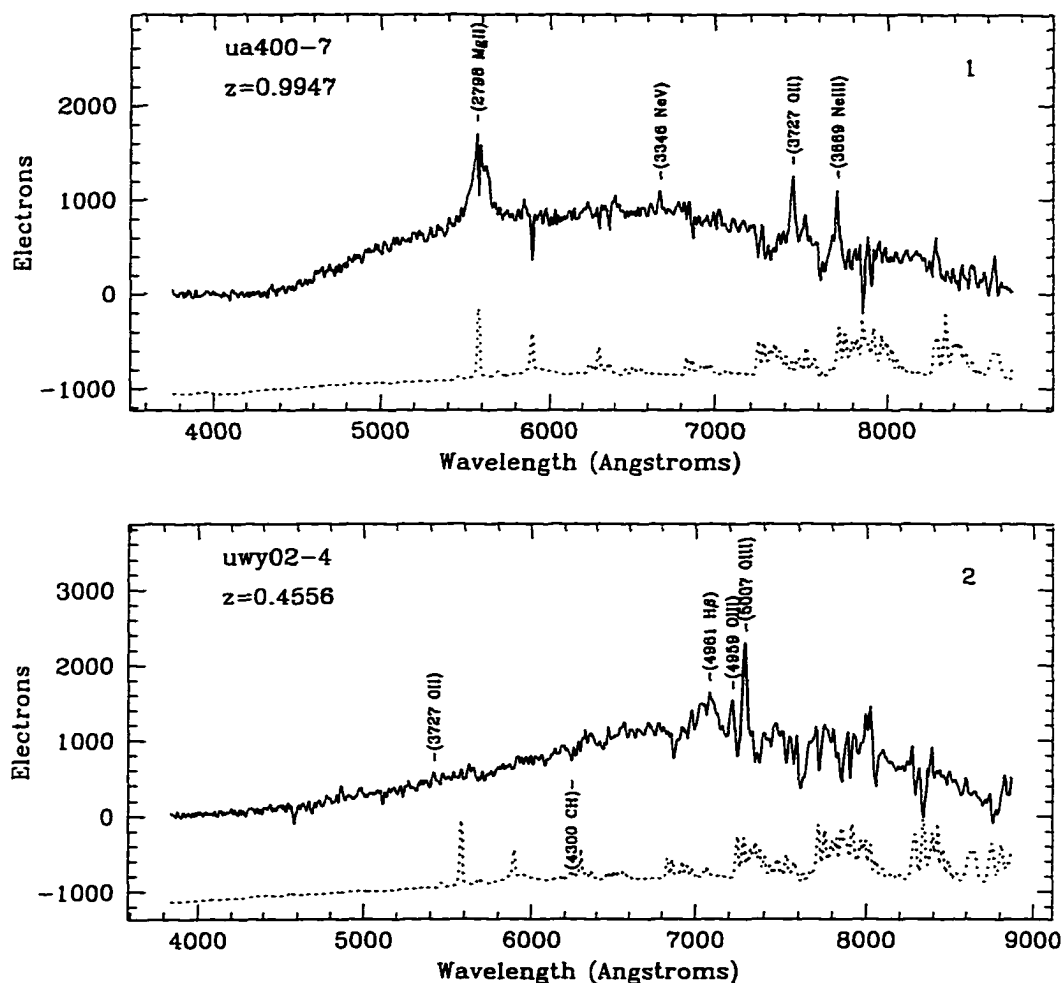
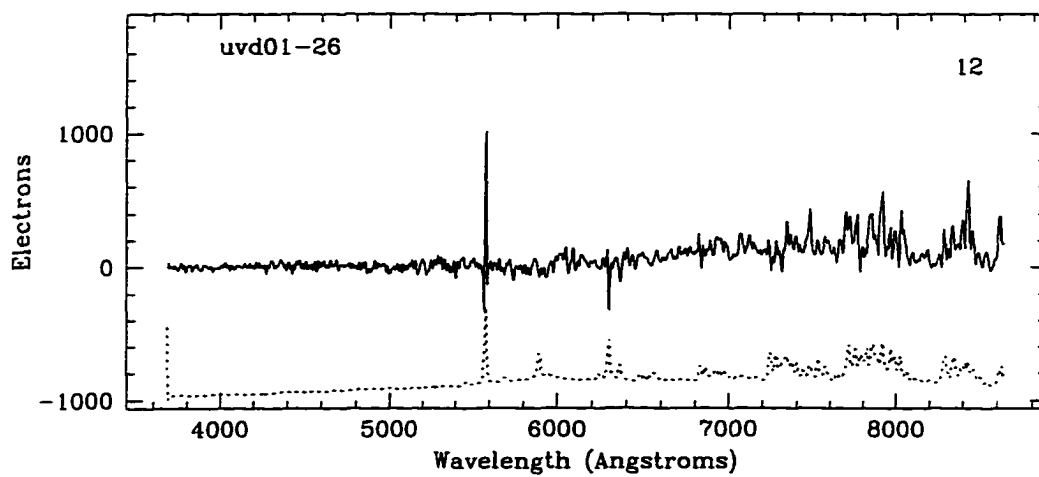
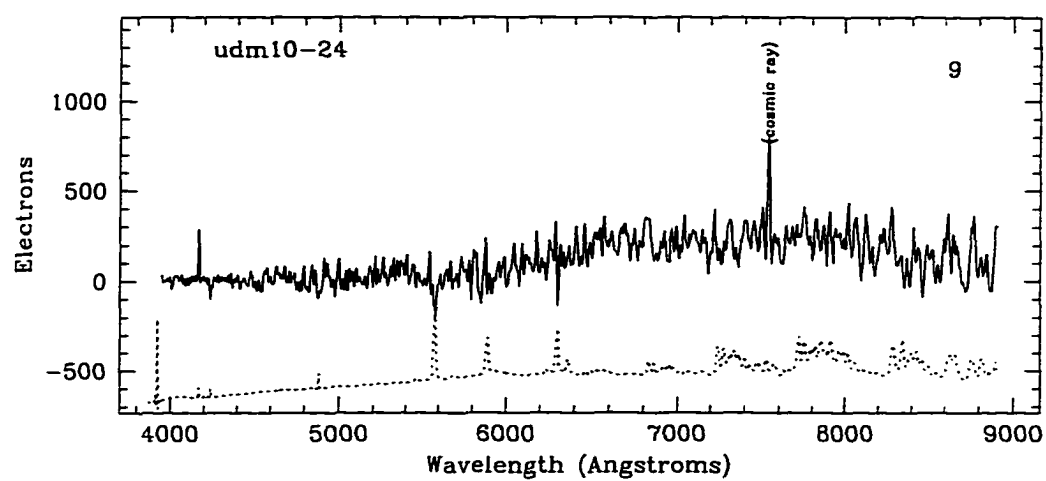
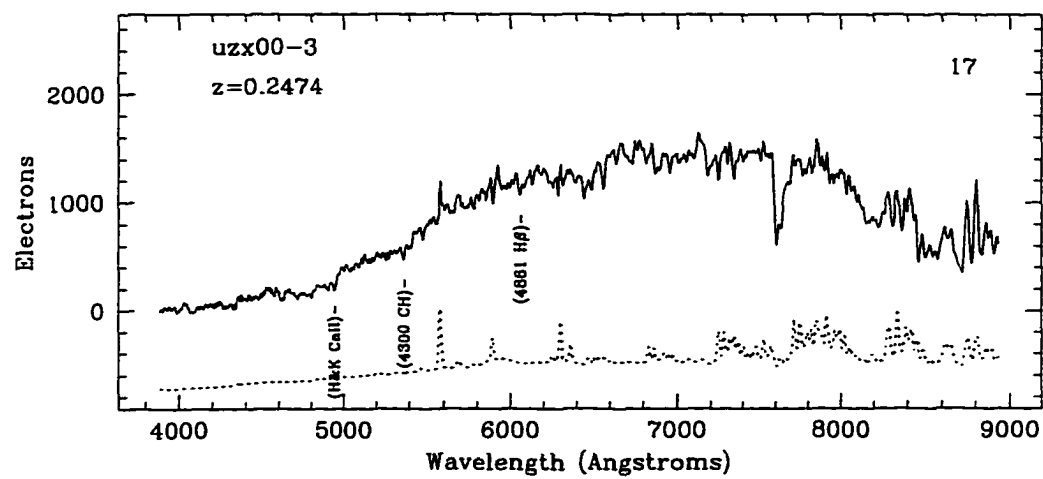
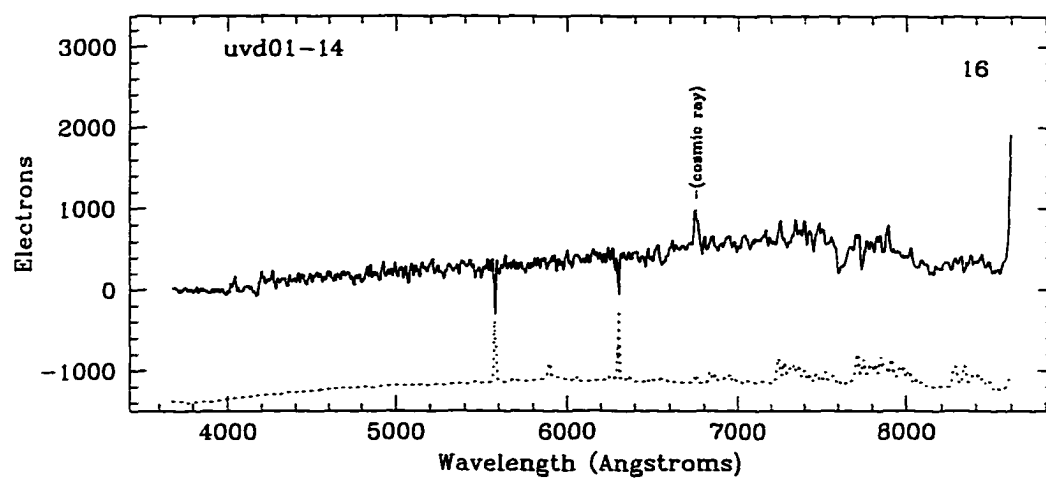
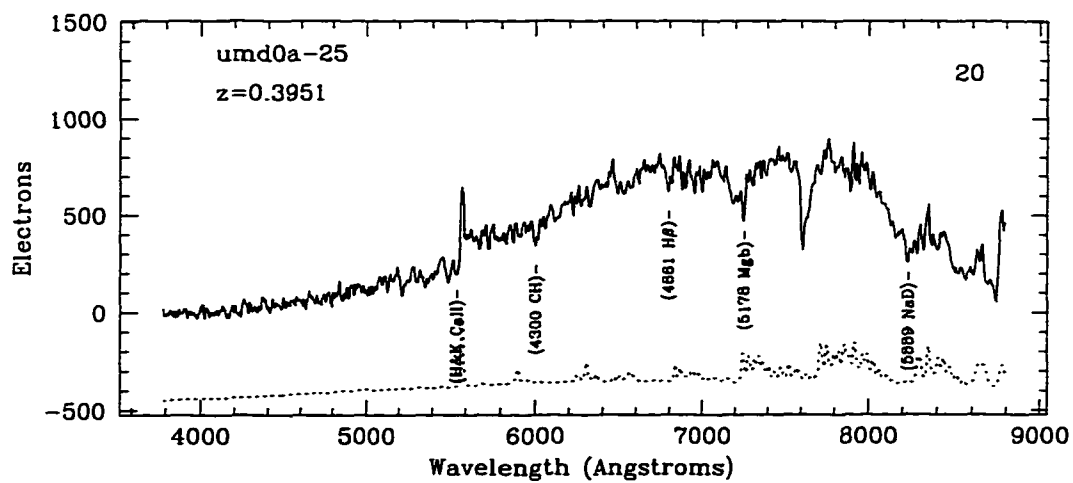
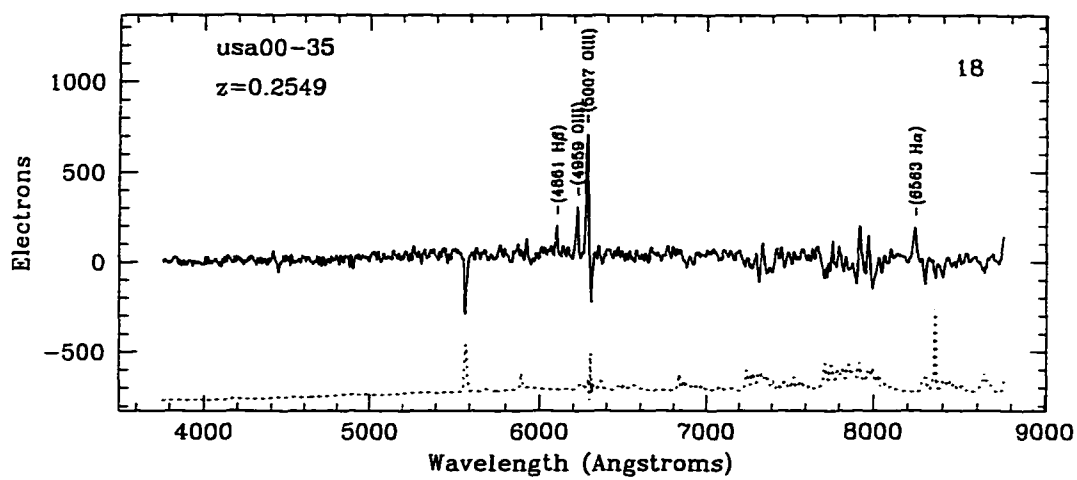
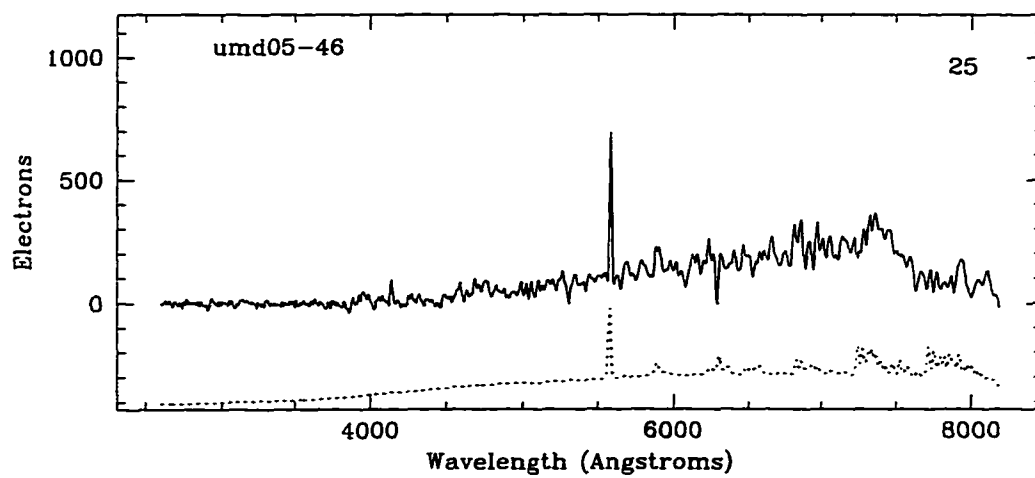
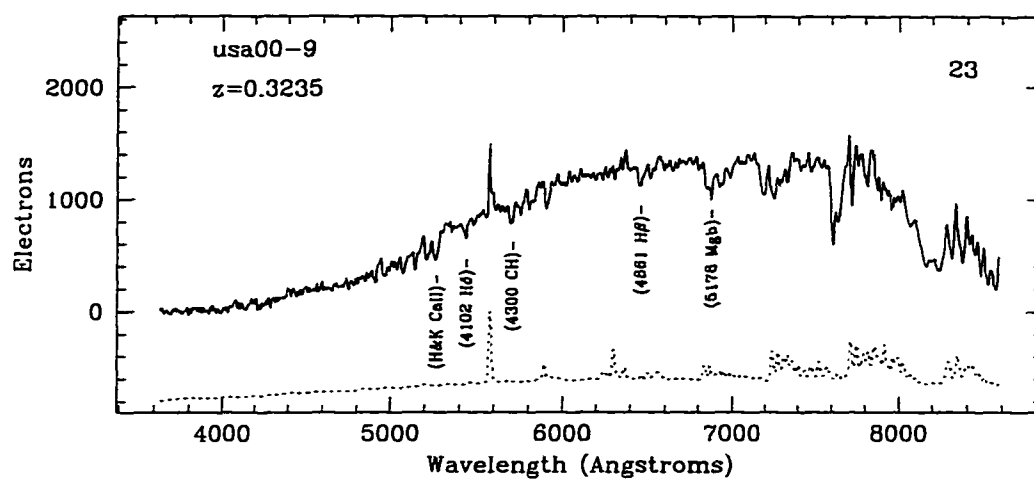


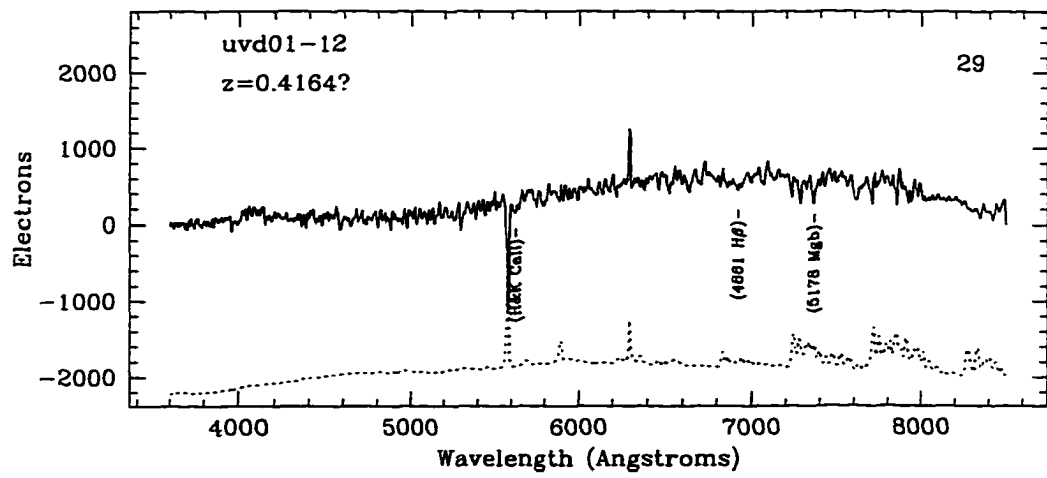
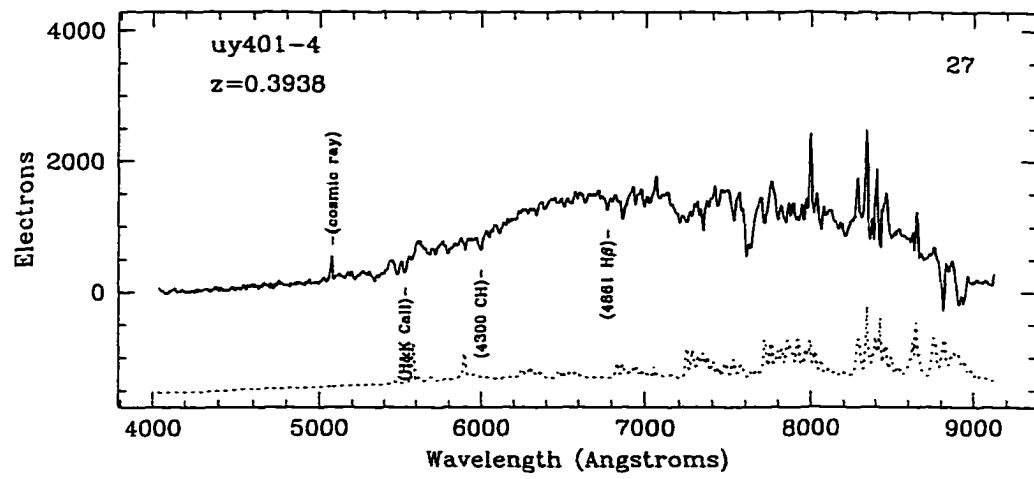
Figure 3.1 Spectra of galaxies containing compact nuclei obtained at the Kitt Peak 4-meter telescope. The spectra are not flux calibrated and are in units of flux (electrons) vs. wavelength (angstroms). Prominent emission and absorption features are indicated. The object name and redshift is in the upper left corner and an ID number corresponding to the ID number for the galaxy image in Figure 2.13 is in the upper right corner. The dashed line is the arbitrarily scaled error spectrum.

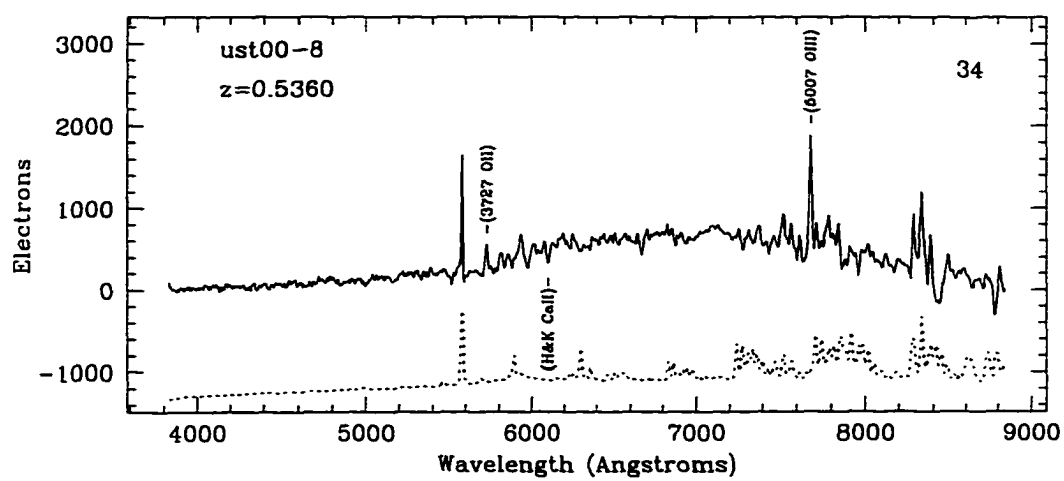
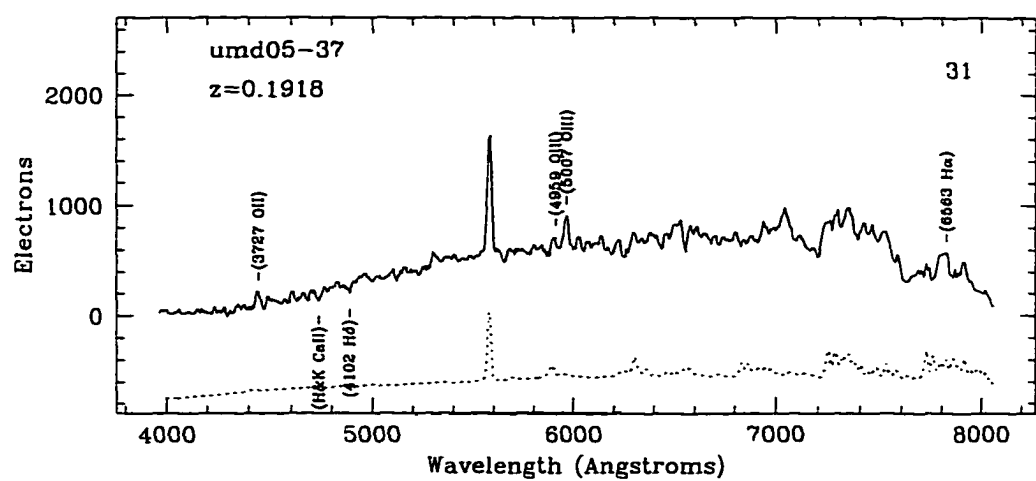


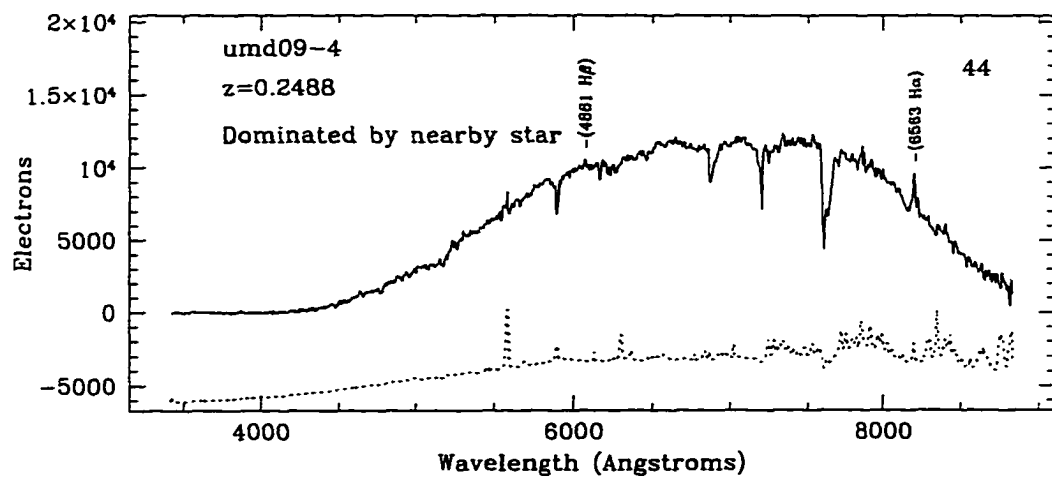
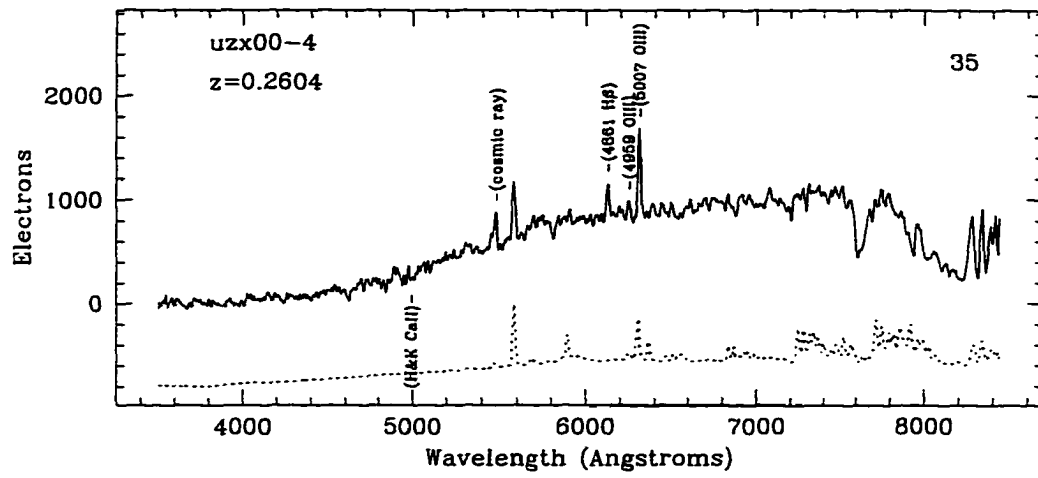


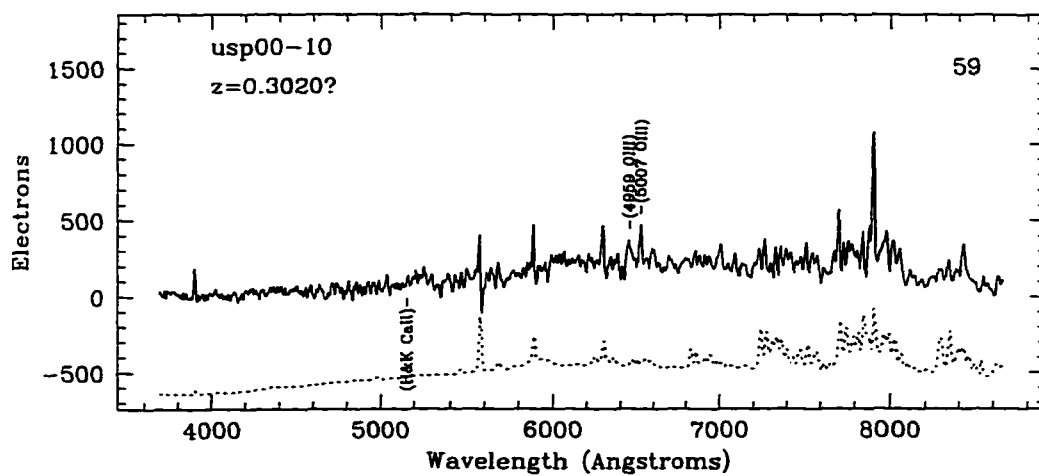
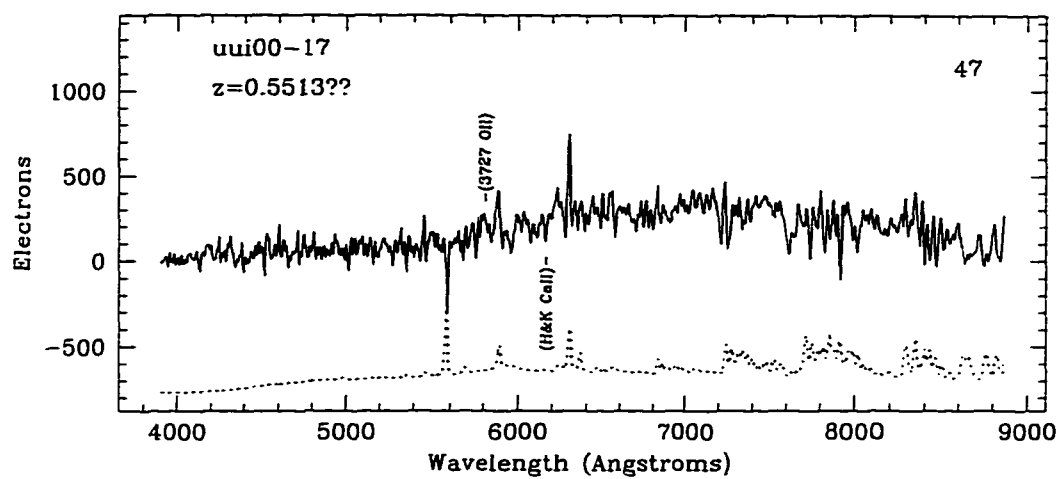


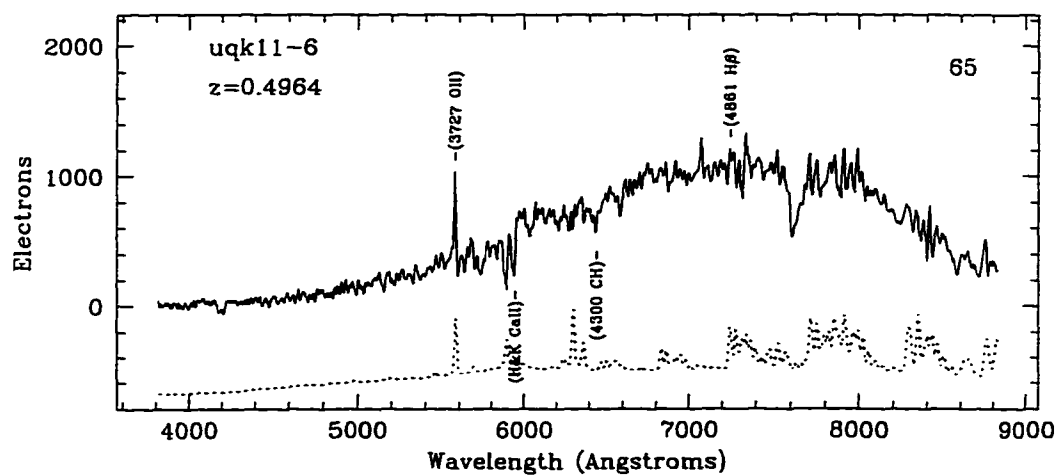
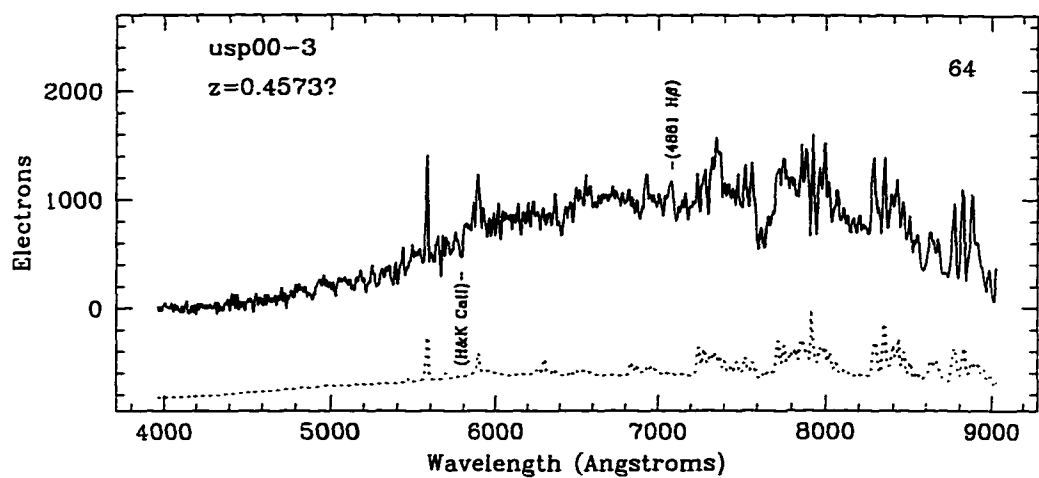


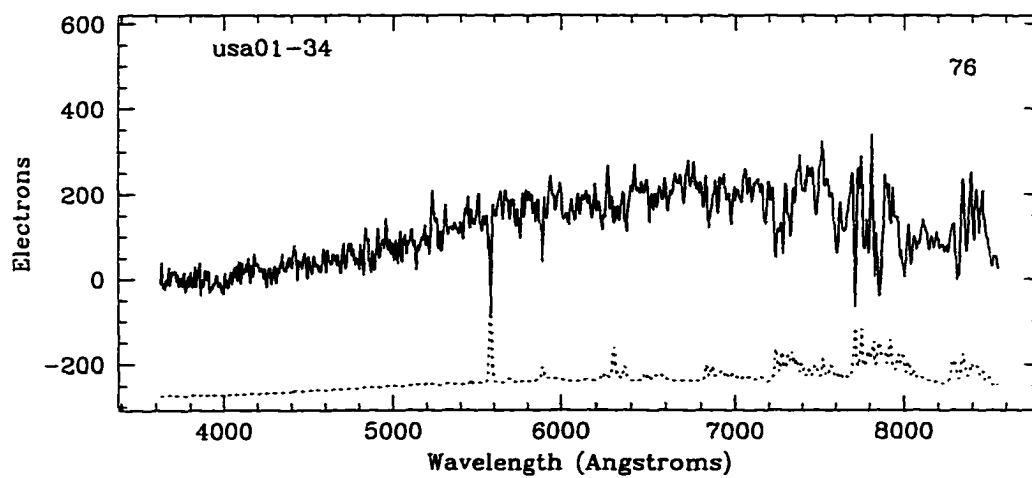
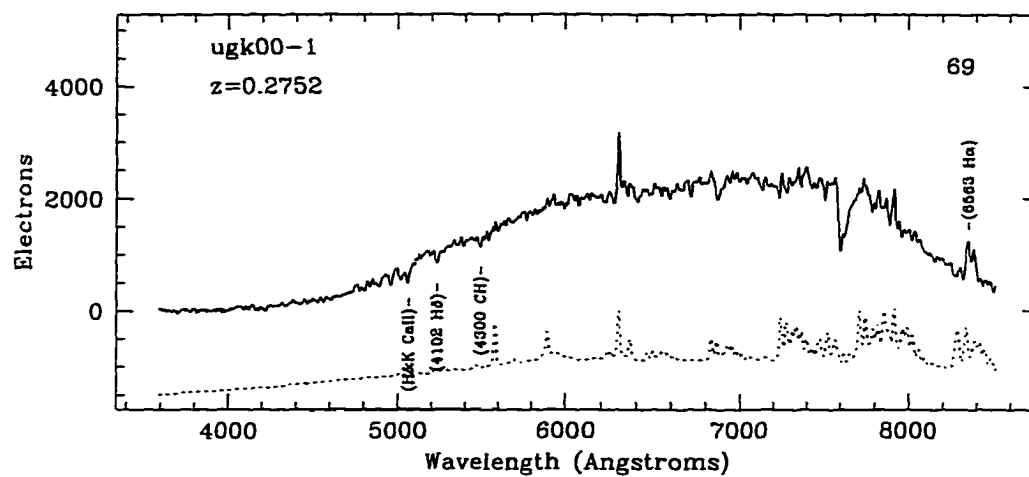


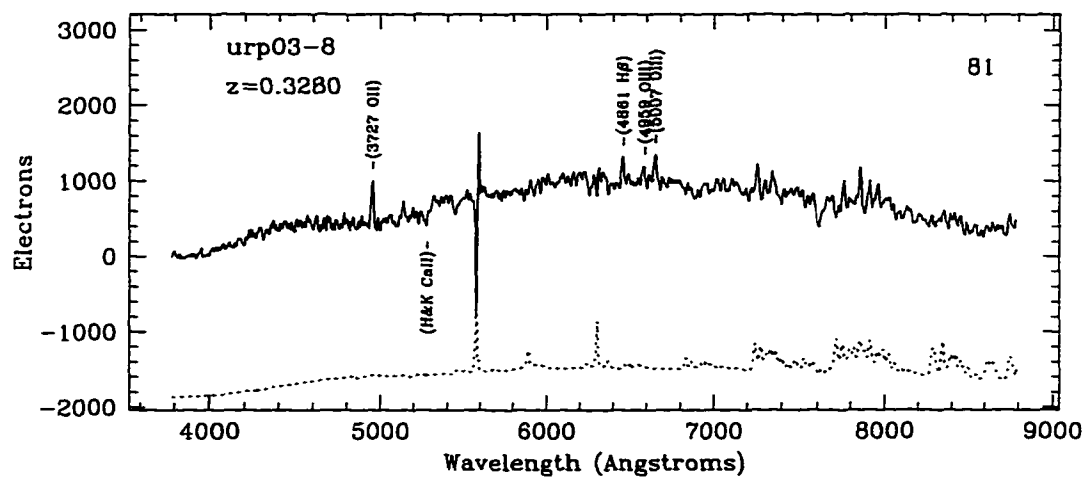
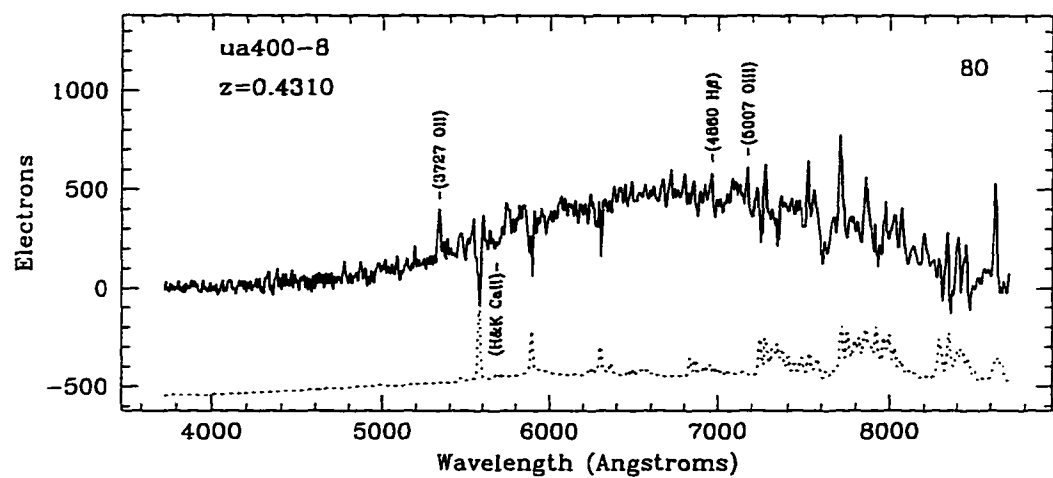


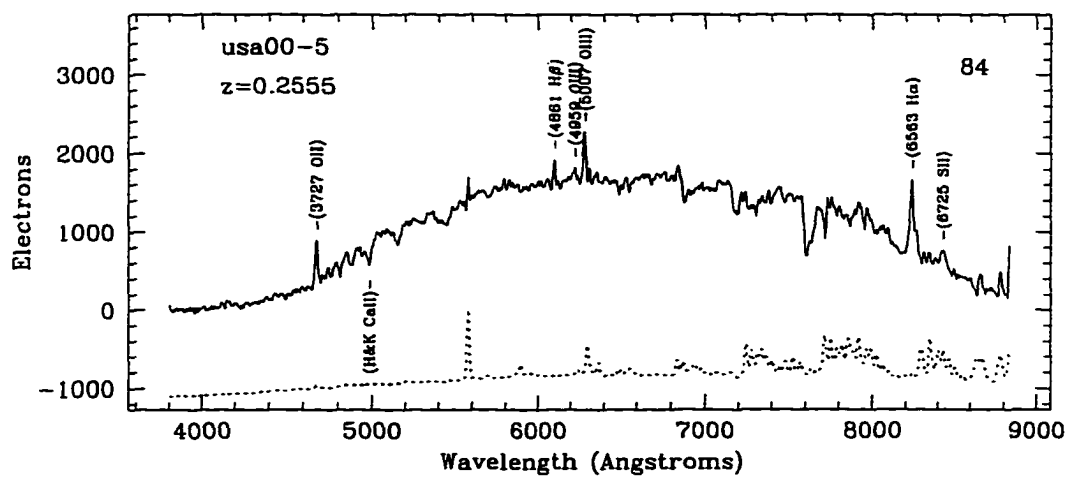
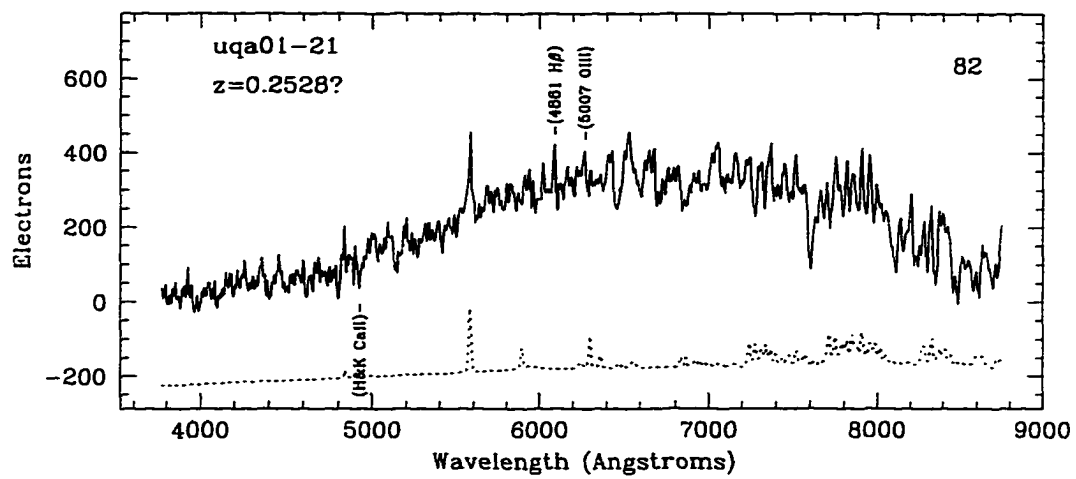


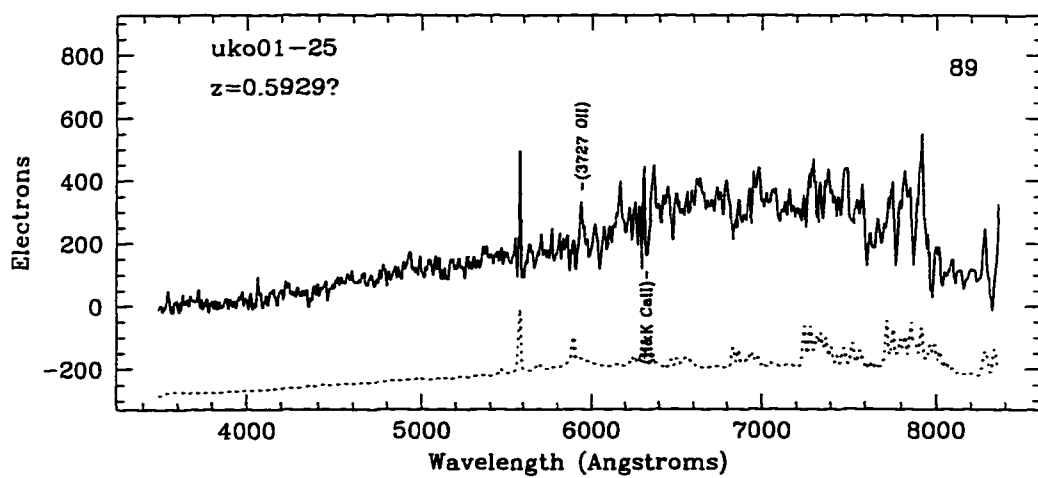
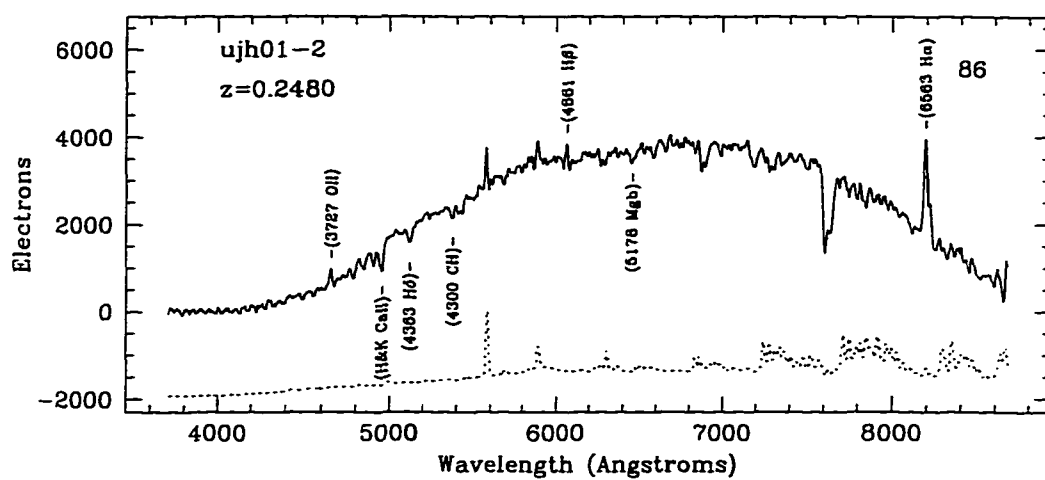


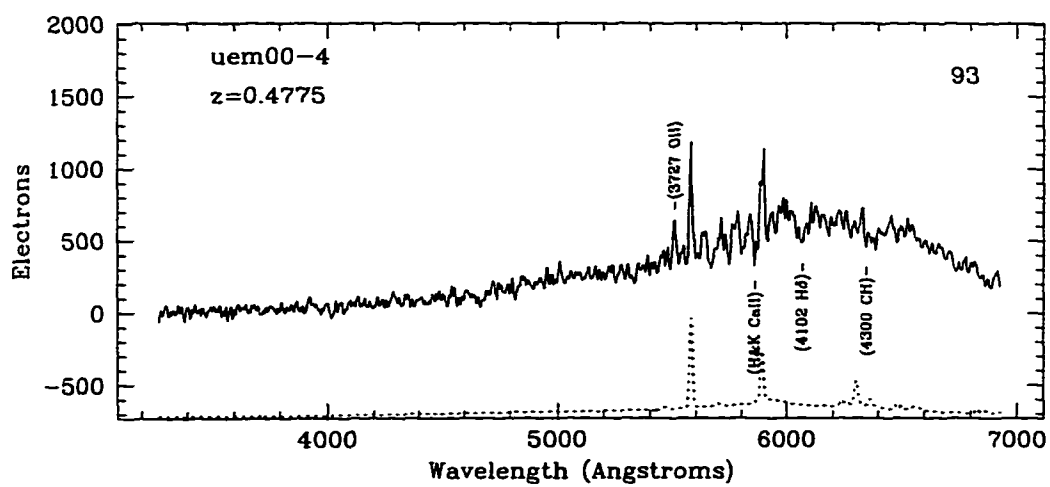
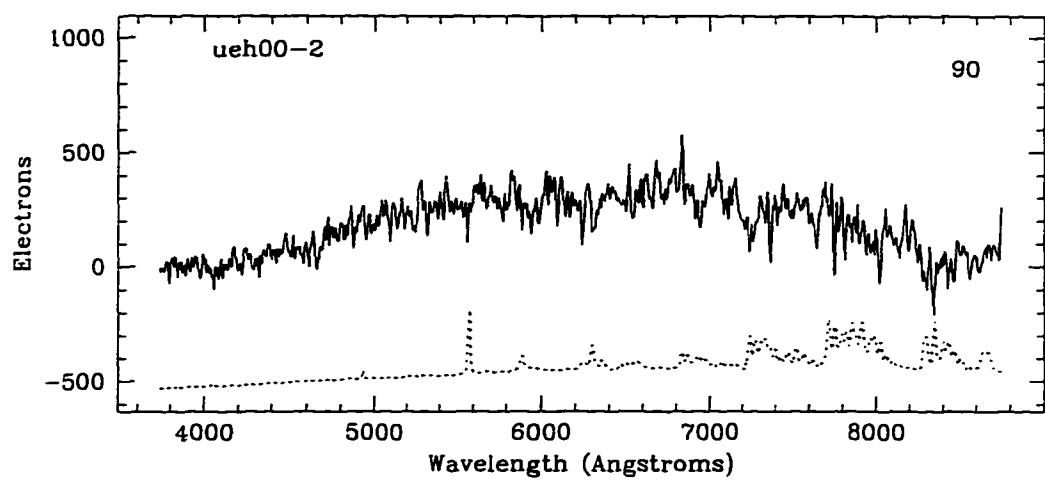


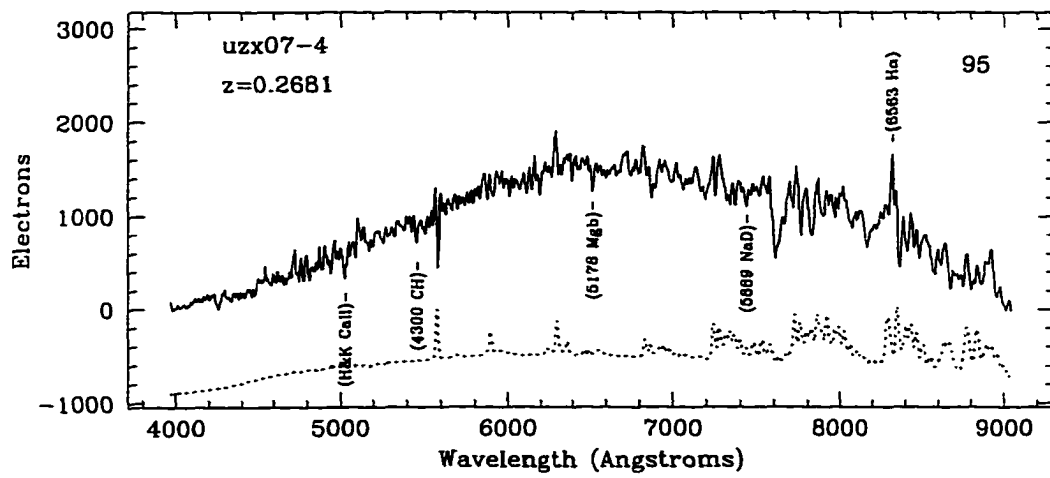
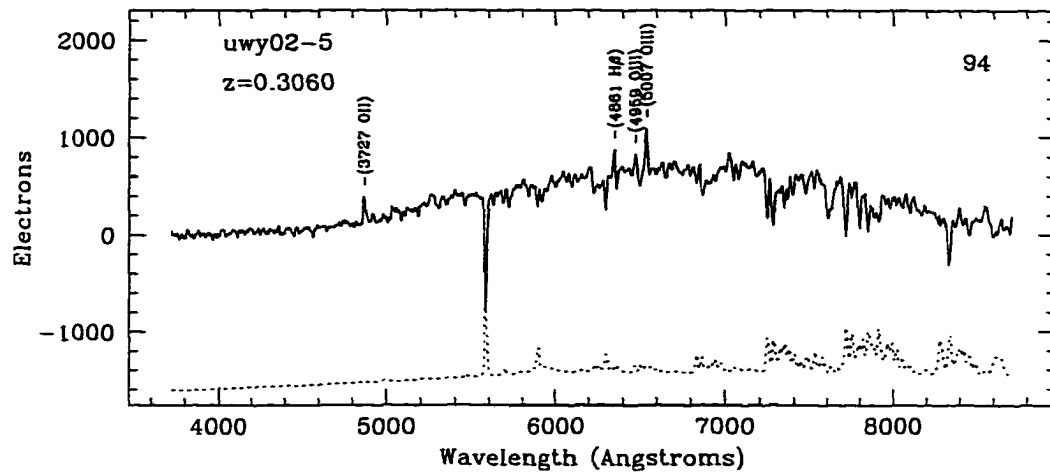


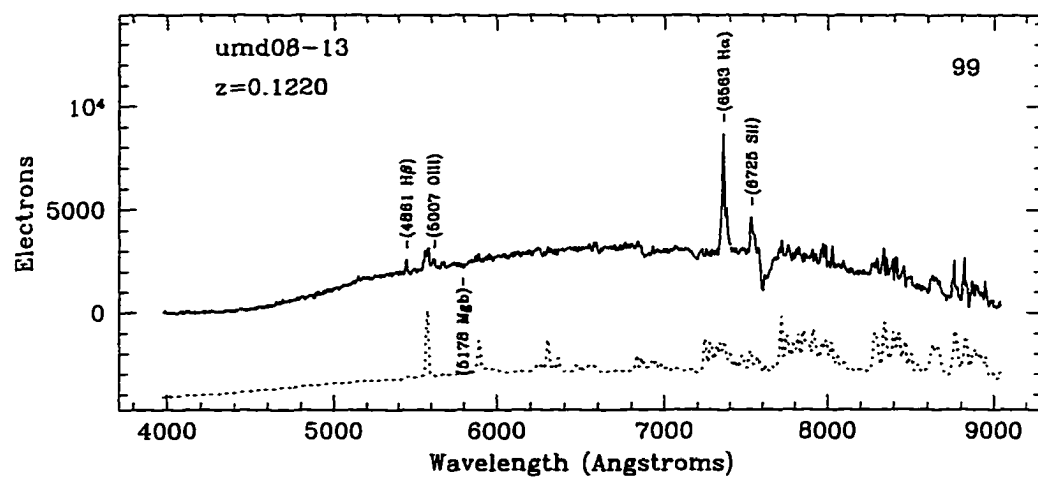
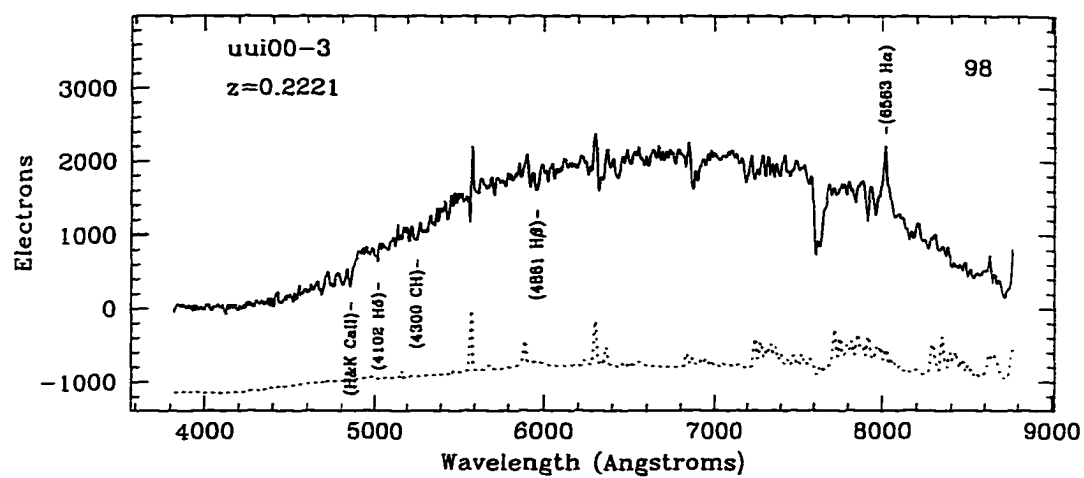


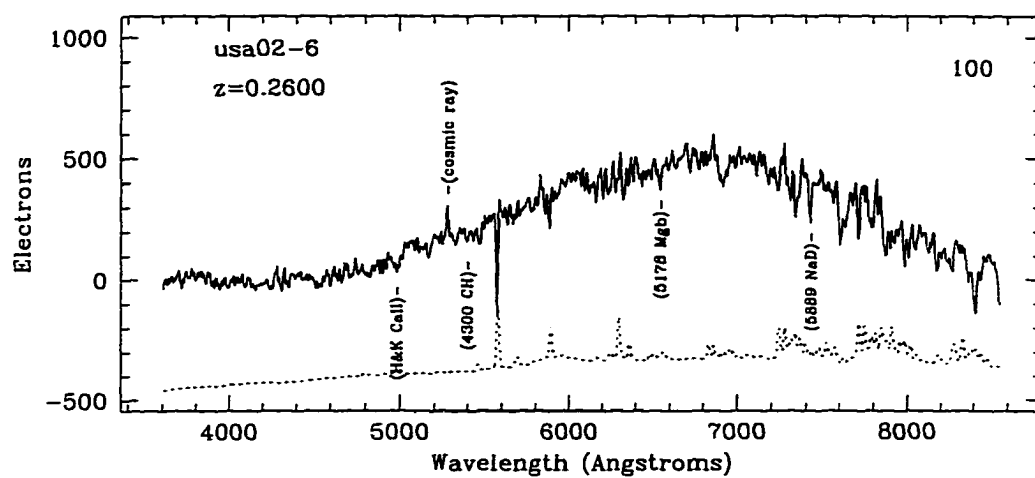












fields, 6 had published redshifts. When we include these fields we have 35 compact nuclei galaxies with known redshifts (35% of the 101 galaxies).

3.3. Spectroscopic Identifications for Nuclear Point Source Galaxies

The nuclei are typically too faint to contribute much light to the galaxy spectrum. As stated in Chapter 2, 59% of the nuclei comprise less than 5% of the total galaxy light. For this reason, we do not expect to see the spectrum of the nucleus in these observations. The typical resolution at the 4 meter is $1''$ which is comparable to the galaxy size in most cases. This level of resolution combined with the faintness of the nuclei makes it impossible to study the nuclear spectrum subtracted from that of the host galaxy.

As mentioned previously, the spectra in Figure 3.1 are arranged in order of decreasing contribution of the nucleus to the total galaxy light. Interestingly, we find that the first two spectra displayed, the galaxies with the brightest nuclear point source components (ua400-7 and uwy02-4) reveal broad emission lines, indicative of Seyfert 1-type galaxies. In the case of ua400-7, we see broad MgII in addition to [NeV] and [NeIII] emission lines. The spectrum of uwy02-4 reveals broad $H\beta$ as well as narrow line [OII] and [OIII] emission. In addition, usa00-35, where the nucleus is 20% of the galaxy V filter light, has a flux ratio of $([OIII] \lambda 5007)/(H\beta \lambda 4861) \simeq 5$. We also detect $H\alpha$ but not [SII] in the spectrum. We determine the $([SII] \lambda 6725)/(H\alpha \lambda 6563)$ flux ratio limit to be $\simeq 0.4$. According to the line ratio diagnostics of Veilleux & Osterbrock (1987), this is likely to be a Seyfert 2 nucleus. These spectroscopic identifications provide a check that our technique to search for unresolved nuclei is sensitive to Seyfert-like nuclei present

in the survey galaxies.

The remainder of the spectra contain a variety of emission and absorption features. Of the 29 spectra with adequate signal-to-noise for redshift determination, 18 display narrow 3727 Å [OII] emission and/or 5007/4959 Å [OIII] emission. Hydrogen emission lines of H β and/or H α are seen in 13 of the spectra. The CaII H and K absorption and 4000 Å blanketing break are seen in 22 of the 29 spectra. These spectra can be used to classify the host galaxy types. Based on spectral features, 19 have spectra consistent with mid to late type spirals while 10 are consistent with early type galaxies from Sa to ellipticals. These classifications are used in Chapter 4 in comparison with the bulge-to-total luminosity ratio classifications for the host galaxies.

3.4. Photometric Redshifts

Our observing strategy was to place slitlets on those galaxies containing nuclear components with the remainder placed on other relatively bright ($I \lesssim 21.0$) galaxies in the field. As described in section 3.2, all compact nuclei galaxies from the MDS, HDF and Groth strip for which redshifts are known make up 35% of the 101 compact nuclei galaxies. For the remainder of our sample, we can estimate redshifts based on several host galaxy parameters.

To determine redshifts “photometrically”, it is necessary to have as large a database as possible of galaxies with measured redshifts and HST images for high resolution photometry. All MDS fields used in this study are imaged in both the V and I filters. We obtained good spectra for 136 galaxies for which redshifts could be determined. Highly reliable redshifts are determined for 102 of these galaxies, where the redshift is based on at least two strong emission or absorption features. At

the time of this study, several redshifts had been published from the HDF (Cohen et al. 1996). Of the HDF galaxies we fit with the modeling software described in Chapter 2, 47 have reliable redshifts published. For the Groth strip, 25 modeled galaxies have reliable published redshifts (Koo et al. 1996). We then removed from these samples any galaxies with poorly fit parameters such as non-convergence of the model in one filter or very irregular morphology. Because the bulge-to-total measurement will be used in the empirical fit, it is important to remove highly irregular galaxies for which the bulge-to-total luminosity ratio less is meaningful. This leaves us with 129 galaxies with excellent model fits where the bulge-to-total luminosity ratio, magnitude and V-I color have been well determined.

Figure 3.2 demonstrates how the color, magnitude, and bulge-to-total luminosity ratio vary as a function of the galaxy redshift. If we break down our sample into different bulge-to-total bins, we see that the relationship between magnitude, color and redshift becomes tighter since we confine ourselves to galaxies of a similar Hubble type. An empirical fit to the data in different bulge-to-total bins will allow for redshift estimation based entirely on color, magnitude and bulge-to-total luminosity ratio. Initially, we also included the half-light radius in the empiricle fit to determine redshift but found that it was not a useful parameter in constraining the redshift.

We use the fitting software GaussFit (McArthur et al. 1994) to perform a least-squares linear regression in 3 dimensions to determine redshift as a function of magnitude and color according to the equation below.

$$z_{est} = C1 \times color + C2 \times mag + C3 \quad (3.1)$$

where C1 and C2 are the coefficients of color and magnitude and C3 is the zero point of the fit. The data were divided into various subsamples of limited

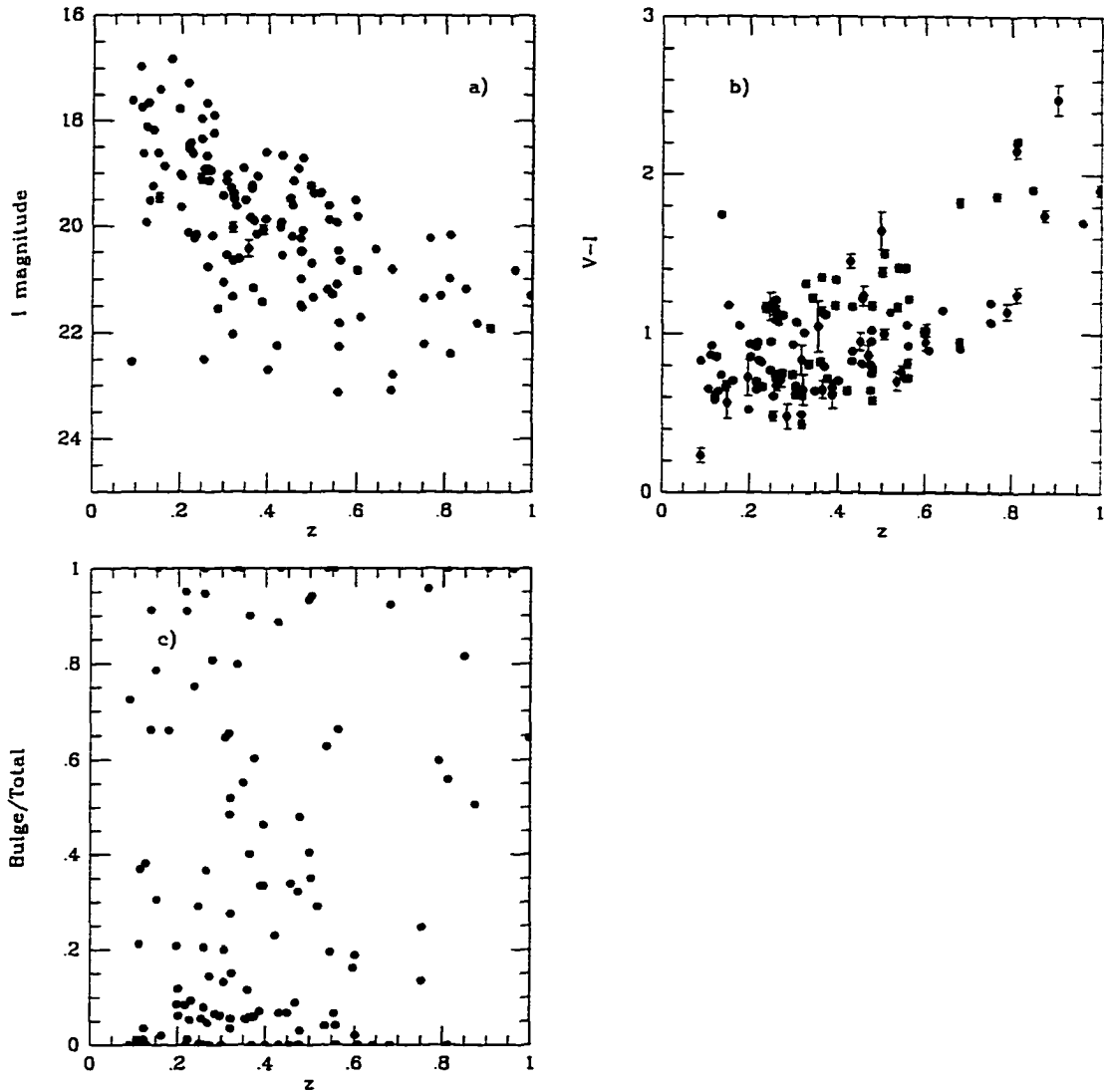


Figure 3.2 a) The I magnitude for galaxies in our survey vs. the measured redshift. b) The V-I color vs. the redshift. c) The Bulge/Total luminosity ratio vs. the redshift.

bulge-to-total ratios and the fitted z values were compared with the input redshifts to determine the 1σ error in the calculated redshift. It was found that among the galaxies having bulge-to-total ratios less than 0.5, 2 galaxies with $z \geq 0.8$ fell far from the linear fit. Since so few data points exist beyond $z=0.8$, we cannot attempt to estimate redshifts accurately beyond this limit. Therefore, these 2 galaxies were removed from the dataset allowing for a much better fit to the remaining data points. After removing these 2 data points, we are left with 127 points in the fit.

The GaussFit fitting procedure was applied to various subsamples of the total galaxy dataset of 127 points. In Figures 3.3 through 3.6 we show the fitting results for subsamples of the data separated into bulge-to-total luminosity ratio bins. Large bulge-to-total bins were chosen so that uncertainties in the determination of the bulge component in galaxies where a nuclear point source is also detected will not significantly affect the redshift estimation. Figure 3.3 contains galaxies with $\text{Bulge/Total} \leq 0.2$, those with $\text{Bulge/Total} \leq 0.5$ are in Figure 3.4, those with $\text{Bulge/Total} > 0.5$ are in Figure 3.5, and Figure 3.6 contains those with $\text{Bulge/Total} \geq 0.8$. In each figure, a) is the I magnitude for the galaxies vs. their measured redshifts, b) is the V-I galaxy color vs. the redshift, c) is the estimated redshift based on the fit vs. the measured redshift, and d) is the residual ($z_{\text{measured}} - z_{\text{est}}$) vs. the measured redshift. The 1σ error in the fitted redshift value is given in the upper left corner of the residual plot in d). Figure 3.7 shows the estimated redshift for all of the galaxies used in this calculation vs. their spectroscopically measured redshifts. This figure is the combination of panel c) from each of the preceding figures. The coefficients for the fit in each subsample in addition to the standard deviation error in the fit are listed in Table 3.2.

The results of this fitting technique were then applied to the galaxies hosting

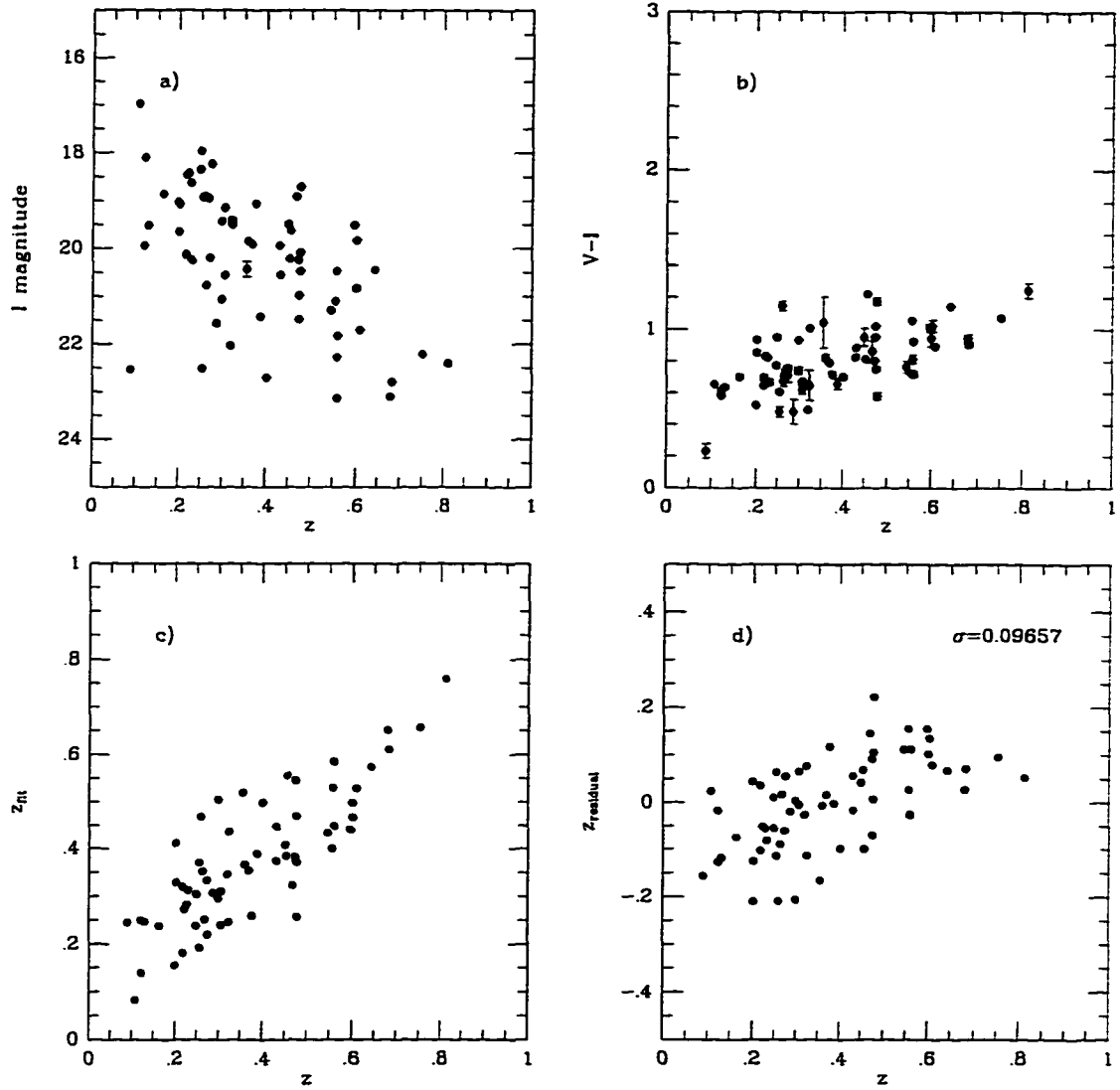


Figure 3.3 a) The I magnitude for galaxies in our survey with $\text{Bulge/Total} \leq 0.2$ vs. the measured redshift. b) The V-I color vs. the redshift. c) The estimated redshift based on fits to the color and magnitude vs. the true redshift. d) The residual of the fit ($z_{\text{measured}} - z_{\text{est}}$) vs. the measured redshift. The standard deviation of the fit is indicated.

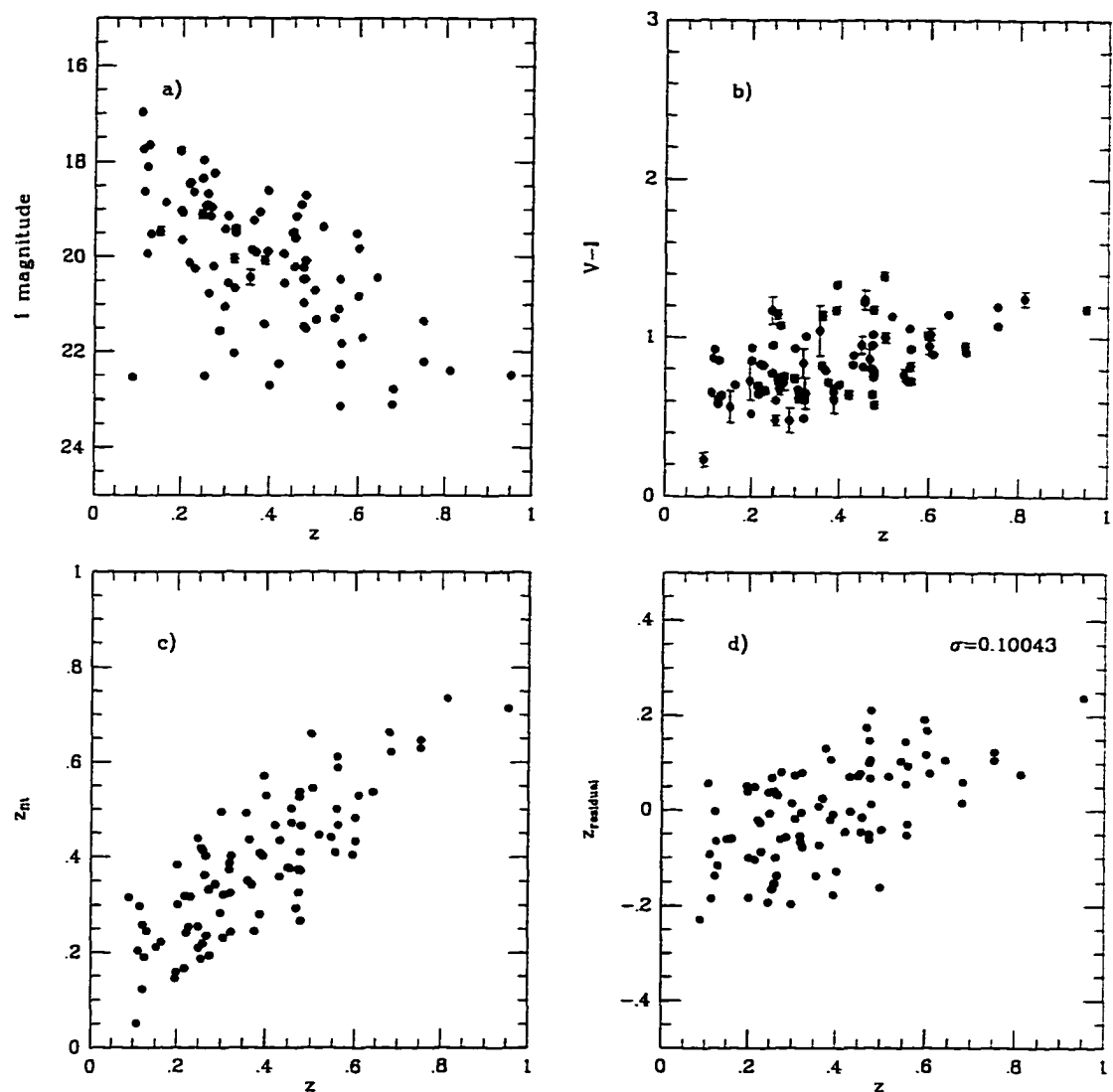


Figure 3.4 a) The I magnitude for galaxies in our survey with $\text{Bulge/Total} \leq 0.5$ vs. the measured redshift. b) The V-I color vs. the redshift. c) The estimated redshift based on fits to the color and magnitude vs. the true redshift. d) The residual of the fit ($z_{\text{measured}} - z_{\text{est}}$) vs. the measured redshift. The standard deviation of the fit is indicated.

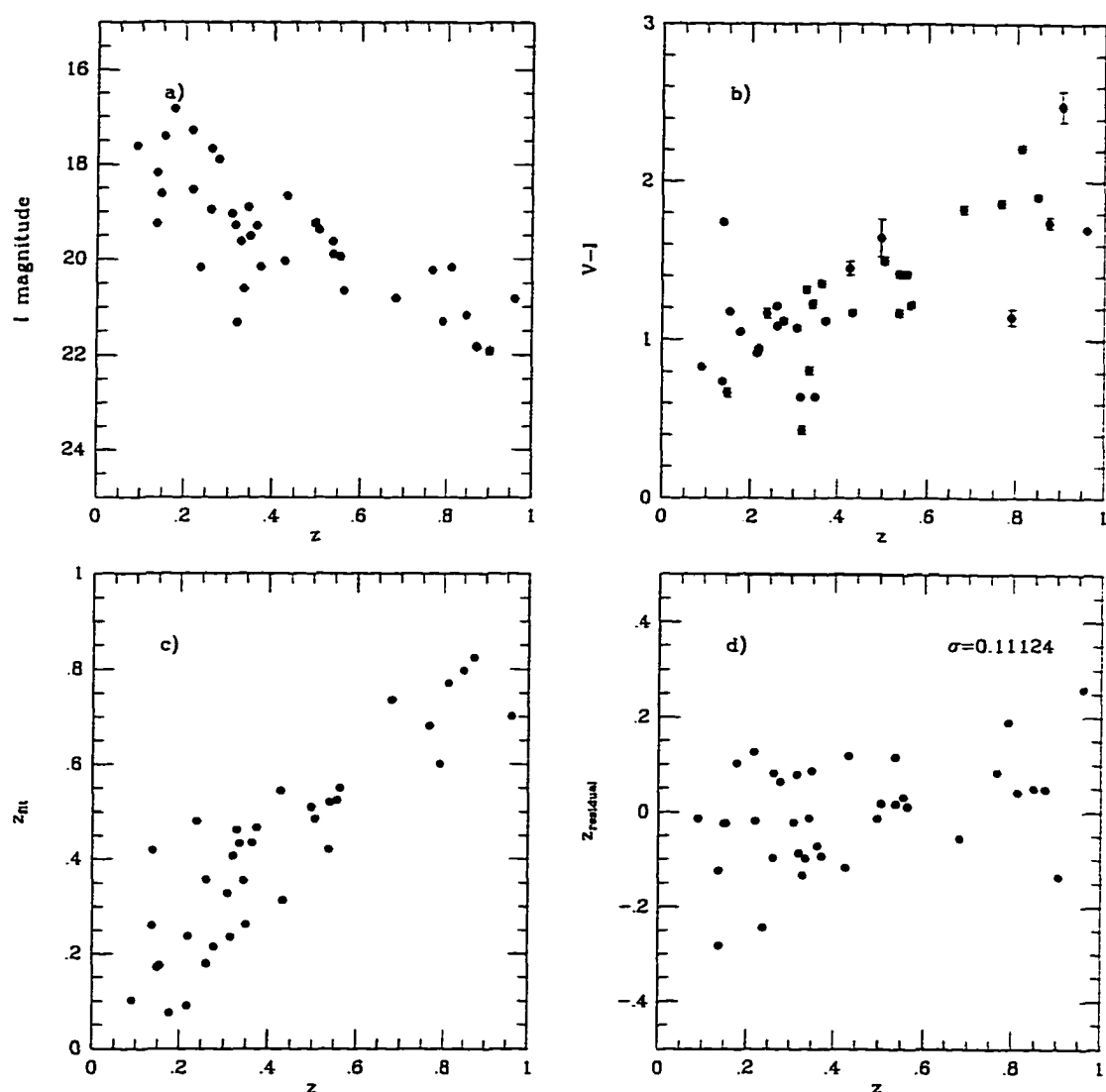


Figure 3.5 a) The I magnitude for galaxies in our survey with Bulge/Total >0.5 vs. the measured redshift. b) The V-I color vs. the redshift. c) The estimated redshift based on fits to the color and magnitude vs. the true redshift. d) The residual of the fit ($z_{measured} - z_{est}$) vs. the measured redshift. The standard deviation of the fit is indicated.

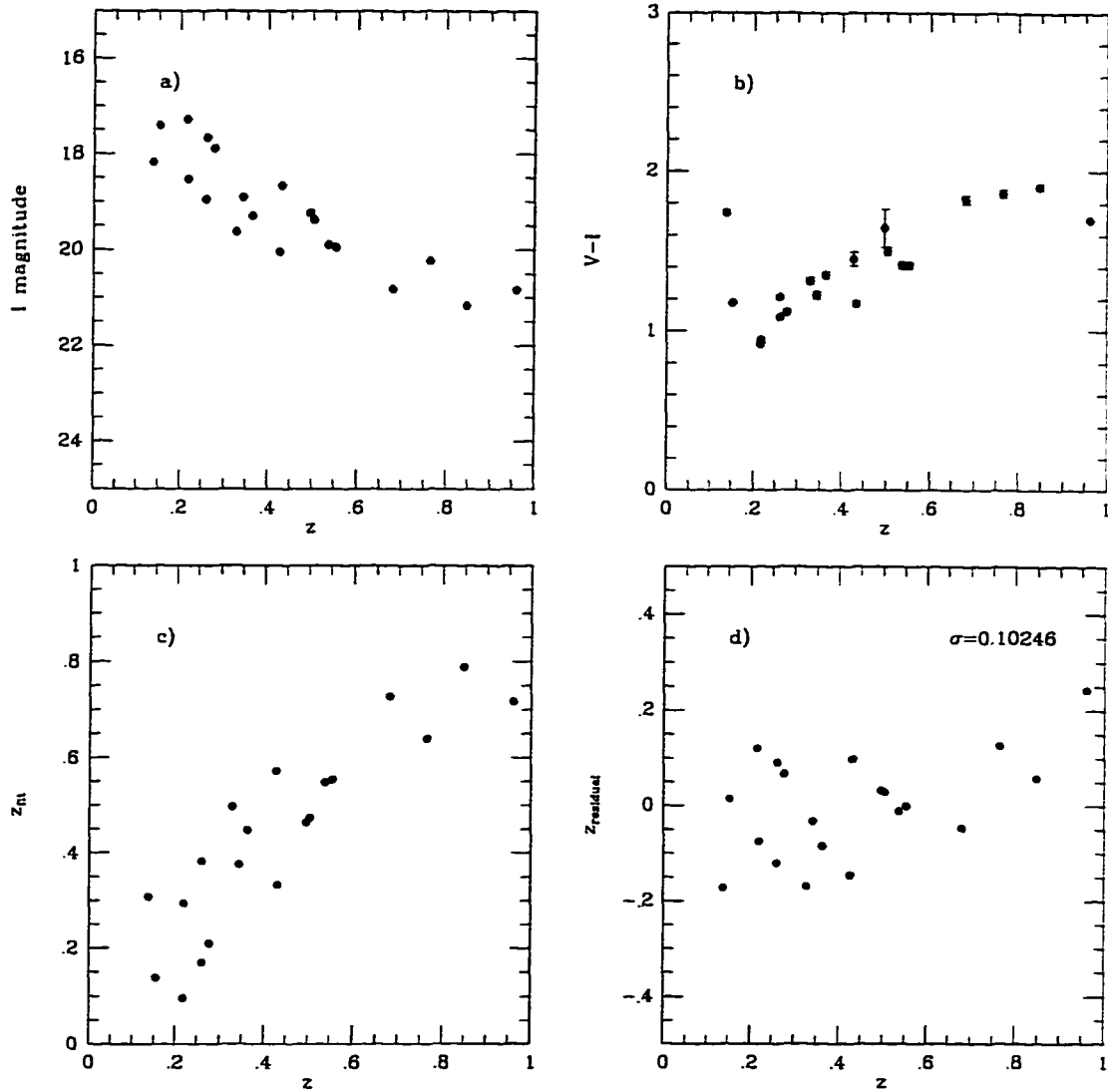


Figure 3.6 a) The I magnitude for galaxies in our survey with Bulge/Total >0.8 vs. the measured redshift. b) The V-I color vs. the redshift. c) The estimated redshift based on fits to the color and magnitude vs. the true redshift. d) The residual of the fit ($z_{\text{measured}} - z_{\text{est}}$) vs. the measured redshift. The standard deviation of the fit is indicated.

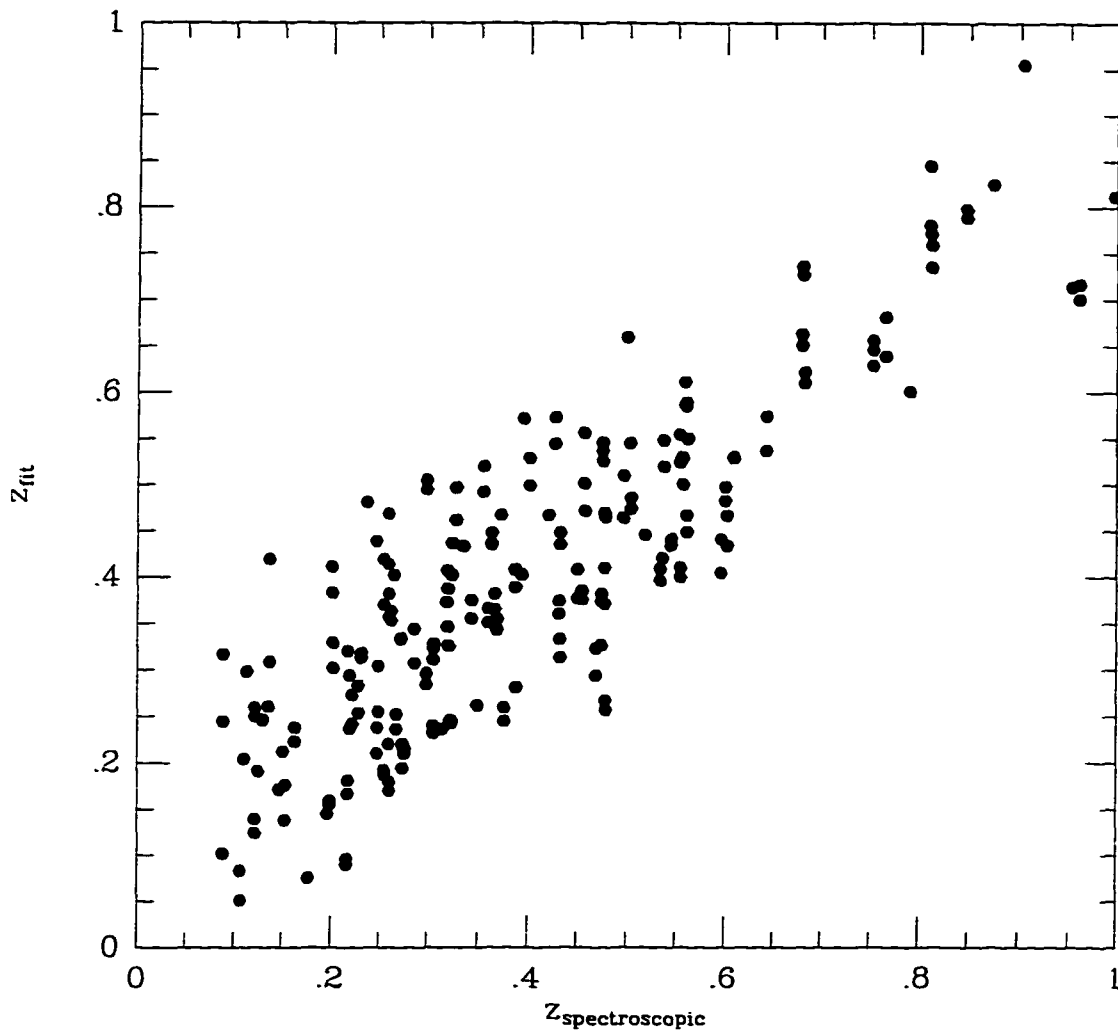


Figure 3.7 The photometric redshift vs. their measured spectroscopic redshift for those galaxies used in the empirical fit.

Table 3.2 Redshift Estimation Coefficients

Bulge/Total	σ_z	# of gals	C1 (color)	C2 (mag)	C3 (zero pt.)
≤ 0.20	0.09657	66	0.5154	0.0681	-1.4084
≤ 0.50	0.10043	88	0.4013	0.0761	-1.4901
> 0.50	0.11124	39	0.2768	0.1115	-2.0903
> 0.80	0.10246	22	0.0868	0.1560	-2.6792

compact nuclei. The typical error in determining redshifts using this technique is $\sigma_z \sim 0.1$. For the purposes of this study, errors of this size are acceptable in determining the space density of compact nuclei. The redshift errors can be incorporated in the determination of luminosity functions for these objects (See Chapter 5). Table 3.3 is the resulting redshift list for the 101 compact nuclei galaxies in our sample. The 29 galaxies with spectroscopic redshifts obtained at the 4 meter are indicated with a star (*). The error in the spectroscopic redshift is estimated from the formal error of the cross-correlation template fit and the error in the fit to identified lines in the comparison spectrum which was used to determine the dispersion solution. Redshifts from the HDF and Groth strip are reported from the literature and are indicated in the table. For the 66 photometrically estimated galaxies, the error in the reported redshift is based upon the standard deviation of the points in the fit and the error in determining the galaxy magnitude and color. The RA and DEC in J2000 are also given in this table for each object.

Four of the estimated redshifts (6%) yielded negative values or values less than $z=0.1$. Objects less than $z=0.1$ are very rare in this survey data based on the spectroscopic measurements and therefore we can assume they are in error. Each of the four galaxies have very blue colors ($V-I \lesssim 0.2$) which caused the redshift to be estimated too low. To achieve a more realistic estimate of the redshift for these galaxies, we determine the average redshift of galaxies within ± 0.5 magnitudes of the galaxy in question. In this way, we use only magnitude information and no color information in the determination. The standard deviation of the average provides the new error estimate for the redshift which is $\sigma_z \simeq 0.2$. This error is rather large but applies to only a small portion of the sample galaxies.

Figure 3.8 is a histogram of the redshifts for the compact nuclei galaxies. The

solid line represents all 101 galaxies with spectroscopic or photometric redshifts. The hatched region is the histogram of only the 35 galaxies with spectroscopic redshifts. There is clearly some peakiness which appears in the spectroscopic as well as the total redshift distribution. The distribution peaks near $z \sim 0.4$ and extends to $z = 1.0$. However, only those redshifts estimated at $z \leq 0.8$ are considered reliable since very few points beyond $z = 0.8$ were used in the empirical fit for the redshift estimation technique.

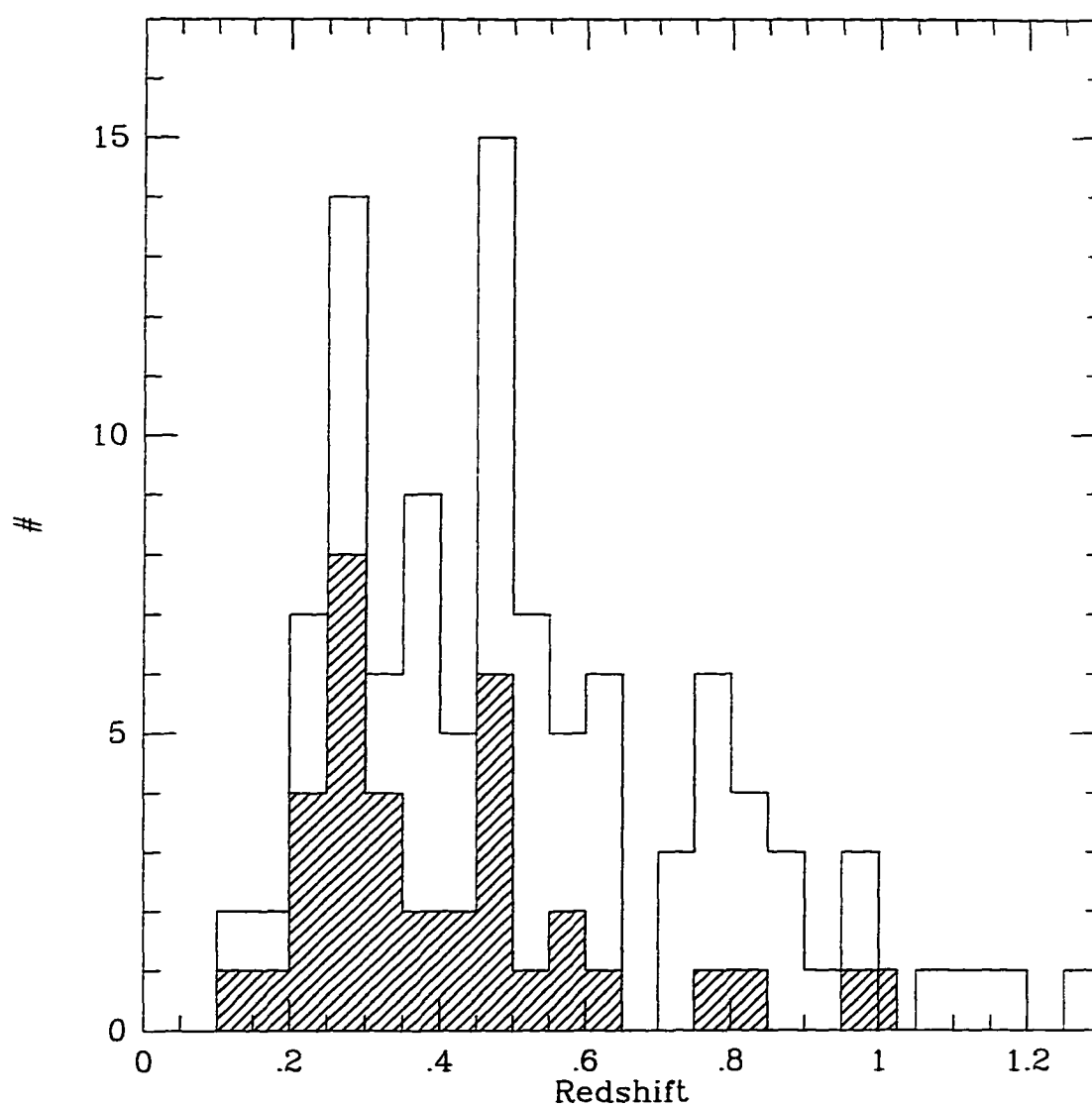


Figure 3.8 The histogram of redshifts for the compact nuclei galaxies. The hatched region represents those galaxies where the redshift was determined spectroscopically.

Table 3.3. Redshift List

ID#	Name	RA	DEC	Redshift	σ_z	Comment
1	ua400-7	0 24 53.42	-27 16 43.4	0.9947	0.0003	*
2	uwy02-4	12 40 20.60	-11 32 13.5	0.4556	0.0004	*
3	ua-30-13	0 58 2.72	-28 12 43.2	0.5547	0.0975	
4	ust01-11	10 5 19.20	-7 46 24.8	0.5113	0.1025	
5	u26x9-20	14 17 28.33	52 25 56.7	1.0727	0.0995	
6	uy401-12	14 35 32.07	25 17 38.0	0.4632	0.0970	
7	ut200-28	16 1 8.64	5 12 47.7	0.7611	0.0989	
8	ufj00-13	2 7 6.50	15 25 0.7	0.4798	0.0969	
9	udm10-24	2 42 54.22	-0 4 30.9	0.8381	0.1025	
10	umd0a-47	21 51 14.30	29 1 7.3	0.8951	0.0990	
11	ua400-26	0 24 52.89	-27 16 9.3	0.8575	0.0977	
12	uvd01-26	15 43 22.64	53 52 11.2	0.7382	0.0971	
13	ua-01-10	1 4 40.54	-27 5 43.7	0.8287	0.0974	
14	uzx01-37	12 30 55.30	12 18 34.3	0.7486	0.1006	
15	ut201-18	16 1 8.40	5 35 25.2	0.7706	0.0977	
16	uvd01-14	15 43 20.90	53 51 52.1	0.5603	0.0968	
17	uzx00-3	12 30 13.99	12 22 29.4	0.2474	0.0003	*
18	usa00-35	17 12 25.89	33 36 36.4	0.2549	0.0002	*
19	ueh02-14	0 53 38.04	12 50 20.8	0.5021	0.2084	
20	umd0a-25	21 51 14.59	28 59 55.7	0.3951	0.0003	*
21	uui00-31	11 42 14.87	71 38 16.9	0.4566	0.1013	

Table 3.3—Continued

ID#	Name	RA	DEC	Redshift	σ_z	Comment
22	u26x6-11	14 17 46.02	52 30 32.6	1.1674	0.1012	
23	usa00-9	17 12 29.36	33 36 36.0	0.3235	0.0003	*
24	uzp01-19	11 50 27.00	28 47 27.4	0.6206	0.0984	
25	umd05-46	21 51 3.06	29 0 16.6	0.3284	0.1373	
26	ueh02-4	0 53 37.88	12 49 48.8	0.3853	0.1575	
27	uy401-4	14 35 29.27	25 19 23.4	0.3938	0.0003	*
28	uj700-29	19 40 33.84	-69 17 13.7	0.6446	0.1013	
29	uvd01-12	15 43 16.31	53 52 35.8	0.4164?	0.0003	*
30	uzp01-24	11 50 29.58	28 47 45.1	0.5450	0.0981	
31	umd05-37	21 51 2.80	28 59 43.8	0.1918	0.0002	*
32	u26x5-6	14 17 47.85	52 30 47.0	0.4915	0.0972	
33	uy400-16	14 35 18.64	24 59 5.9	0.7761	0.1018	
34	ust00-8	10 5 44.51	-7 41 7.2	0.5360	0.0003	*
35	uzx00-4	12 30 20.87	12 22 47.7	0.2604	0.0002	*
36	uzx00-20	12 30 20.35	12 21 50.5	0.4604	0.0971	
37	u26x7-18	14 17 42.15	52 26 45.2	0.7111	0.0982	
38	u26x8-23	14 17 35.82	52 25 33.1	0.6830	0.0975	
39	uzd10-6	13 55 22.96	40 20 49.7	0.3691	0.1007	
40	u26x9-25	14 17 23.14	52 25 28.9	0.7302	0.1007	
41	u26x6-9	14 17 46.35	52 30 43.8	0.5208	0.0976	
42	ust00-27	10 5 43.76	-7 42 1.5	0.7774	0.0971	
43	uhdfk-106	12 36 41.38	62 12 16.3	1.1670	0.0978	

Table 3.3—Continued

ID#	Name	RA	DEC	Redshift	σ_z	Comment
44	umd09-4	21 50 40.26	28 56 29.1	0.2488	0.0002	*
45	urp03-14	8 47 23.28	17 57 51.2	0.3231	0.0987	
46	uxy10-6	12 36 37.45	-0 42 58.8	0.3904	0.0971	
47	uui00-17	11 41 57.11	71 37 30.1	0.5513??	0.0003	*
48	uci10-11	1 24 41.22	3 51 56.6	0.3801	0.0970	
49	uhdfk-36	12 36 49.56	62 12 58.6	0.4750	...	1
50	u26x8-31	14 17 35.06	52 25 41.5	0.6886	0.1030	
51	ufj00-17	2 7 10.39	15 25 37.4	0.2967	0.0971	
52	u26x7-10	14 17 40.59	52 27 13.1	0.6174	0.0997	
53	uzk02-5	12 11 18.95	39 26 27.0	0.1994	0.0973	
54	usa02-34	17 12 28.02	33 35 29.3	0.4613	0.0975	
55	uui00-11	11 42 2.76	71 37 18.5	0.2735	0.0967	
56	uim01-9	3 55 30.05	9 43 44.7	0.2520	0.1013	
57	uhdfk-68	12 36 49.12	62 11 49.6	0.8576	0.0972	
58	ua-01-9	1 4 35.01	-27 4 54.2	0.6116	0.1063	
59	usp00-10	8 54 18.71	20 3 51.4	0.3020?	0.0003	*
60	uhdfk-32	12 36 49.47	62 14 7.7	0.7520	...	1
61	u26x7-7	14 17 37.09	52 27 39.1	0.3511	0.1008	
62	umd0a-63	21 51 17.68	29 0 54.4	0.2504	0.1008	
63	uhdfk-17	12 36 53.80	62 12 54.9	0.6420	...	1
64	usp00-3	8 54 12.38	20 4 15.4	0.4573?	0.0003	*
65	uqk11-6	7 24 48.88	60 31 26.3	0.4964	0.0003	*

Table 3.3—Continued

ID#	Name	RA	DEC	Redshift	σ_z	Comment
66	ut201-37	16 1 14.56	5 34 35.0	0.5067	0.0978	
67	uhdfk-63	12 36 43.29	62 11 52.8	0.4519	0.0967	
68	ua-30-20	0 58 2.92	-28 12 29.0	0.5211	0.0994	
69	ugk00-1	2 38 52.48	16 43 29.3	0.2752	0.0003	*
70	u26x9-8	14 17 24.57	52 23 57.3	0.3431	0.1015	
71	u26x8-7	14 17 31.07	52 25 24.0	0.2870	...	2
72	ust01-7	10 5 12.19	-7 47 15.8	0.3597	0.0978	
73	uj000-28	19 39 18.25	-46 14 46.8	0.4663	0.1935	
74	u26x7-14	14 17 39.94	52 28 20.8	0.3072	0.1292	
75	uhdfk-46	12 36 45.34	62 13 27.0	0.4416	0.0967	
76	usa01-34	17 12 27.06	33 35 57.6	0.5873	0.0969	
77	ut201-33	16 1 11.32	5 35 32.9	0.4562	0.1079	
78	uy400-15	14 35 16.91	24 59 11.4	0.7825	0.0986	
79	uy000-14	14 16 15.42	11 32 4.6	0.5149	0.1119	
80	ua400-8	0 24 53.94	-27 15 57.5	0.4310	0.0003	*
81	urp03-8	8 47 21.26	17 56 52.7	0.3280	0.0003	*
82	uqa01-21	17 36 41.53	28 4 31.2	0.2528?	0.0003	*
83	uj000-20	19 39 19.86	-46 13 2.8	0.4797	0.1973	
84	usa00-5	17 12 21.34	33 35 56.7	0.2555	0.0002	*
85	ust00-23	10 5 49.23	-7 41 38.5	0.8957	0.0990	
86	ujh01-2	1 9 0.38	35 35 38.9	0.2480	0.0002	*
87	u26x6-6	14 17 47.60	52 29 4.1	0.8098?	...	2

Table 3.3—Continued

ID#	Name	RA	DEC	Redshift	σ_z	Comment
88	ux400-7	15 19 38.88	23 53 2.0	0.2663	0.0966	
89	uko01-25	4 56 49.45	3 52 6.7	0.5929?	0.0003	*
90	ueh00-2	0 53 22.38	12 32 56.0	0.1908	0.0973	
91	u26x8-5	14 17 26.51	52 27 5.7	0.2472	0.0969	
92	urz00-8	12 53 0.61	-29 15 4.3	0.3541	0.0966	
93	uem00-4	3 4 59.22	-0 11 46.5	0.4775	0.0004	*
94	uwy02-5	12 40 22.59	-11 31 12.5	0.3060	0.0002	*
95	uzx07-4	12 30 47.73	12 19 43.4	0.2681	0.0003	*
96	uhdfk-27	12 36 49.65	62 13 14.0	0.4750	...	1
97	u26x8-12	14 17 34.35	52 25 25.8	0.5925	0.1047	
98	uui00-3	11 42 1.65	71 37 33.1	0.2221	0.0002	*
99	umd08-13	21 50 32.22	28 50 29.4	0.1220	0.0002	*
100	usa02-6	17 12 20.46	33 34 41.4	0.2600	0.0003	*
101	uim01-4	3 55 33.17	9 44 45.6	0.3097	0.1118	

Note. — Comments are as follows: (*)-spectroscopically determined at the KPNO 4-meter; (1)-from Cohen et al. (1996); (2)-from Koo et al. (1996).

CHAPTER 4

COMPACT NUCLEI GALAXIES: HOST GALAXIES AND NUCLEAR COLORS

The sample of 101 galaxies containing unresolved nuclei is large enough to study, with some statistical significance, the morphological and photometric characteristics of the nuclei and host galaxies. Here we examine the properties of the hosts and compare them with local AGN and starburst host galaxies. The colors of the nuclei themselves are used to answer questions concerning the nature of this population of objects.

4.1. Properties of The Host Galaxies

4.1.1. Host Galaxy Types

When discussing the host galaxy types for the point source nuclei galaxies in our sample, it is very important to determine how well the bulge component is measured in these galaxies. This measurement effect was examined using

Monte-Carlo simulations described in sections 2.4.2 and 2.5. The galaxies used in the simulation were originally fit with disk+bulge models before the simulated nuclear point source was added. Based on this *a priori* disk+bulge fitting, we have a known “input” bulge-to-bulge+disk ($B/B+D$) luminosity ratio which can be compared with the measured $B/B+D$ luminosity ratio when the simulated point source is detected in the galaxy.

Figure 2.9b shows how the bulge-to-bulge+disk ratio varies with the point source-to-total ratio for point sources detected in the simulated data. We see that for detections of point sources greater than 20% of the total galaxy light, the bulge is never detected regardless of the input bulge value. It is clear that we are unable to separate and measure the bulge and point source components when the point source is a large contributor ($\geq 20\%$) of the total galaxy light. Point sources fainter than 20% of the galaxy light are often measured as having non-zero bulge components. Figure 2.9a shows that in the case of fainter nuclei, the bulge is often accurately measured. We note that in all of the cases where the input bulge-to-total was zero, it was also measured as zero.

For point sources fainter than 20% of the galaxy light where the input bulge-to-total ratio is non-zero, how often is it measured accurately and how often is it measured as zero? Figure 4.1 shows the fraction of galaxies where the bulge is measured at 0% in the simulations as a function of the input bulge-to-total luminosity ratio. The error bars represent the Poisson statistics based on the number of points in each bin. From this figure we see that as the bulge becomes more significant, it is more likely to be measured accurately and not go undetected.

We can apply this statistical result to the real sample of compact nuclei galaxies to determine what fraction of these galaxies may actually contain a

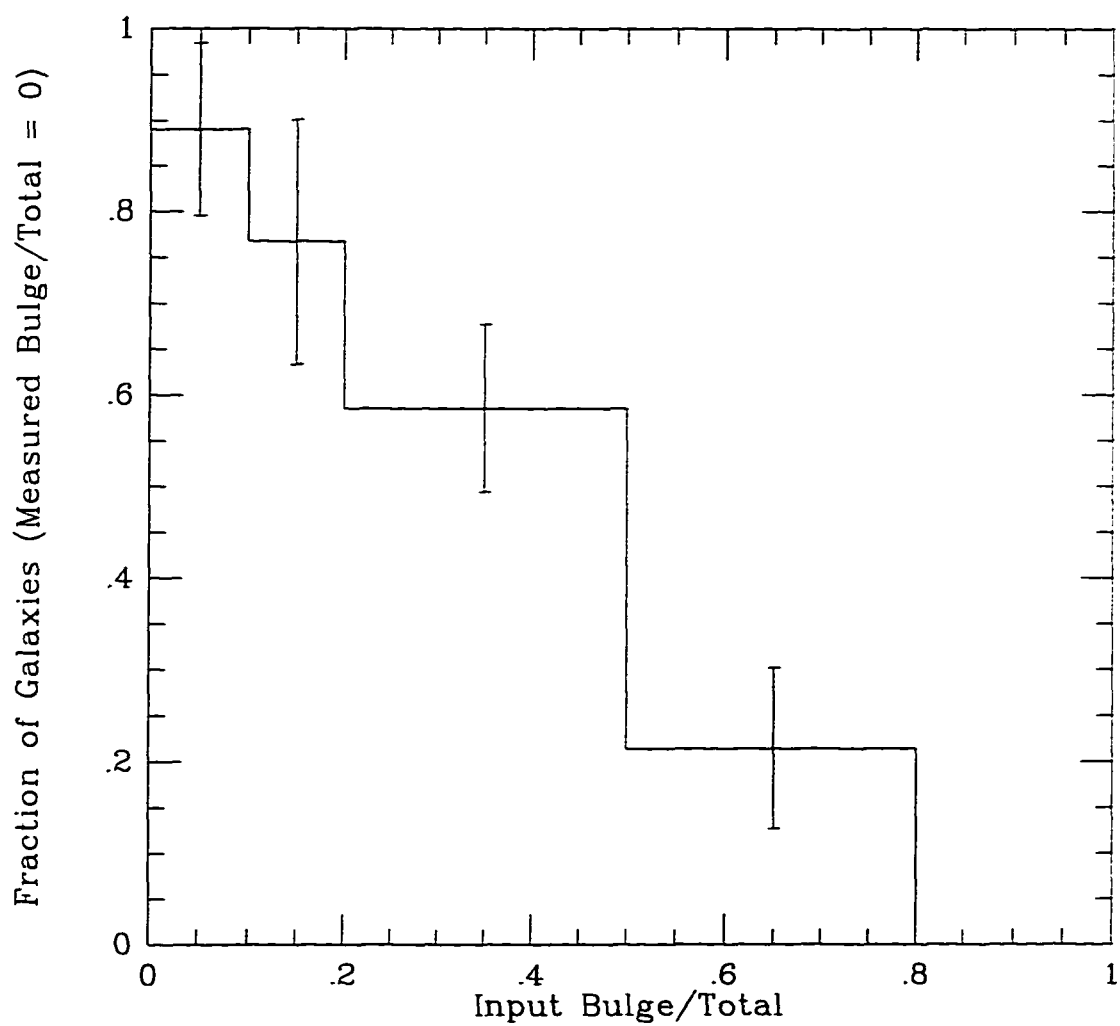


Figure 4.1 The fraction of galaxies in the Monte-Carlo simulation where the measured Bulge/Total is zero as a function of the input Bulge/Total for the galaxy. The errorbars are the Poisson statistics based on the number of galaxies in each bin.

significant bulge. Of the 101 compact nuclei galaxies in our sample, only 8 have point source-to-total luminosity percentages greater than 20%. For these 8, the bulge is measured at 0% as we would expect based on the simulations. Any of these 8, however, could contain a significant bulge component which is not being properly measured due to the bright point source nucleus. Examination of these 8 images (see first 8 boxes of Figure 2.13), reveals spiral-like nebulosity suggesting the presence of a disk. A hidden bulge component in these galaxies may be as much as 50% of the total light but is probably not dominating the host galaxy.

The remaining 93 galaxies have point source-to-total luminosity percentages less than 20%. Of these, 57 are measured to have no bulge component. We can estimate the fraction of the 57 that are statistically likely to contain a bulge based on Figure 4.1. In Figure 4.1, the fraction of galaxies having measured bulge-to-bulge+disk luminosity ratios between 0 and 0.2 is high, indicating that a large fraction of host galaxies having bulge components as large as 20% will be measured as having no bulge. Our 57 hosts with 0% bulge are likely to contain bulges anywhere from 0% to 20% of the total host galaxy light. Therefore, our first grouping of host galaxy types are those with $0 \leq (B/B+D) < 0.2$ since it is difficult to differentiate these galaxy types with higher resolution. There are a total of 79 hosts in this grouping after adding 22 with $0 < (B/B+D) < 0.2$.

There are 9 galaxies measured with $0.2 \leq (B/B+D) < 0.5$. According to Figure 4.1, $59\% \pm 9\%$ of galaxies with this size bulge will be measured with no bulge when a point source (of less than 20% the galaxy light) is detected. If 9 galaxies have $0.2 \leq (B/B+D) < 0.5$ then as many as 9 to 19 galaxies of this type will be measured with 0% bulge. Three host galaxies fall in the $0.5 \leq (B/B+D) < 0.8$ bin. Figure 4.1 indicates that $21\% \pm 9\%$ of these galaxy types will be measured as having 0%

bulge. Based on this percentage, we would expect one additional host galaxy with $0.5 \leq (B/B+D) < 0.8$ to be measured as having no bulge component.

According to this analysis, the 57 host galaxies measured with no bulge component are likely to be comprised of 9 to 19 galaxies with $0.2 \leq (B/B+D) < 0.5$ and 1 galaxy with $0.5 \leq (B/B+D) < 0.8$. Removing these 10 to 20 galaxies from the $B/B+D=0$ bin allows us to statistically redistribute the host galaxy types based on our previous simulations. The solid line in Figure 4.2 is the measured $B/B+D$ distribution for the 101 host galaxies containing compact nuclei. The dashed lines are the statistically redistributed histograms where the 2 lines represent the two extremes of the distribution. Here we have assumed that the 8 host galaxies with point source nuclei greater than 20% of the galaxy light have bulges less than 50% of the host galaxy light and could lie entirely in the $0 \leq (B/B+D) < 0.2$ bin or the $0.2 \leq (B/B+D) < 0.5$ bin.

The dashed lines in Figure 4.2 indicate that the actual number of host galaxies having $0 \leq (B/B+D) < 0.2$ is likely to be from 58% to 76% of the 101 host galaxies in our sample. 18% to 36% may have $0.2 \leq (B/B+D) < 0.5$. Only 6% are likely to have $B/B+D \geq 0.5$. We note, however, that the incompleteness estimates for detecting point sources in galaxies containing a substantial bulge is high. Figures 2.11b and 2.11c show that the completeness is typically 25 to 40% over the point source-to-total range of interest for galaxies with $0.5 \leq (B/B+D) < 1.0$. Therefore, there are likely to be 2.5 to 4 times as many point source nuclei present than were actually found in galaxies with large bulges.

Figure 4.2 shows that even at the extremes, the majority of host galaxies (58-76%) have small bulges indicating late-type spiral galaxy hosts. One-fifth to one-third may be early-type spirals with bulges greater than 20% of the galaxy

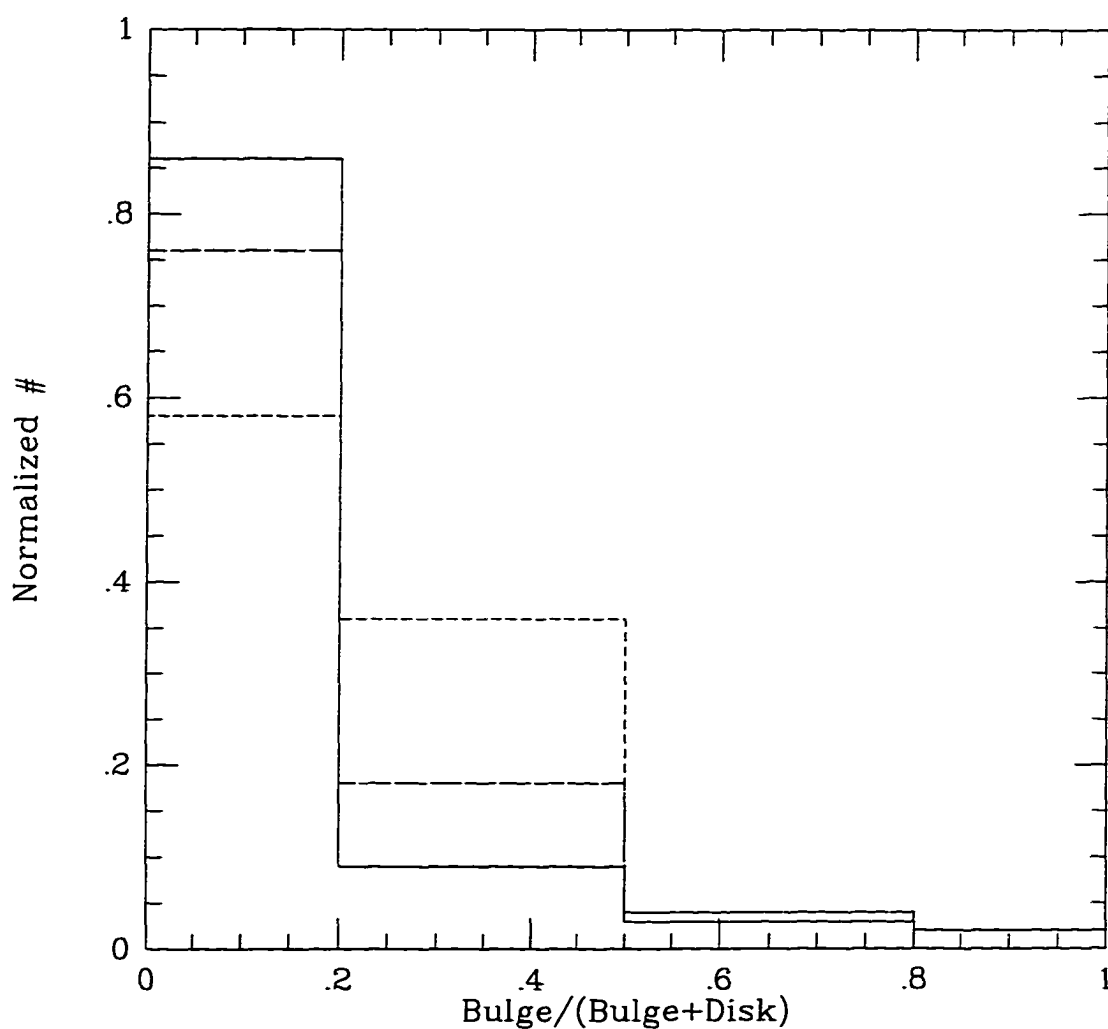


Figure 4.2 The distribution of Bulge/Bulge+Disk measurements for galaxies containing compact nuclei. The solid line is the actual number distribution. The two dashed lines represent two extremes of the distribution after statistically correcting for bulge misclassification as described in the text.

light but less than 50%. We detect only 6% with bulges greater than 50% of the host galaxy light. Incompleteness corrections could increase this from 6% to $\sim 10\%$ (see discussion in following section).

To compare our sample with local host galaxy types of Seyferts and starbursts, we will assume a galaxy with $B/B+D \leq 0.2$ is a late type spiral (Sc to Sb) and $0.2 \leq (B/B+D) < 0.5$ is an early type spiral (Sa to S0). Although Hubble type does not depend on Bulge/Disk measurement alone we can estimate the approximate type based on a study of the luminosity distribution in nearby spiral galaxies (Boroson 1981). The CfA Seyfert galaxies studied in McLeod & Rieke (1995) had Hubble types ranging from S0 to Sc with no elliptical hosts. 45% were found in late type spirals and the remaining 55% in early type spirals. These Seyferts, although considered low-luminosity AGN, are likely to have intrinsically brighter nuclei than our sample since they were selected spectroscopically. A more comparable sample to ours can be found in the Ho et al. (1997a) study of “dwarf” Seyfert nuclei in nearby galaxies. They find about 13% of the dwarf nuclei reside in ellipticals, while 35% are in S0 to Sa galaxies and 53% reside in Sb through Sm galaxies. This distribution is close to that of our host galaxy distribution in Figure 4.2 assuming incompleteness effects in our detection of ellipticals.

The Balzano (1983) study of starburst nuclei in local galaxies finds that, for the classifiable galaxies, 3% are in ellipticals, 30% are in early type spirals, and 67% are in late type spirals. Locally, starburst galaxies appear to favor late type spirals more so than dwarf Seyfert nuclei and this causes the local starburst host type distribution to more closely resemble our host galaxy type distribution. Our host galaxy type distribution is also consistent with some combination of local Seyfert nuclei hosts and starburst nuclei hosts. Without separating the AGN from

starburst nuclei, we can find no evidence for evolution of the dominant host galaxy types for starbursts or AGNs in our moderately redshifted sample.

As part of this study, we also note the galaxies in our survey for which we obtained spectra and compare their Bulge/Total measurements with Hubble-types as estimated from their spectra. Kennicutt (1992) presents integrated spectra of nearby galaxies and compares emission and absorption features with Hubble class for normal and peculiar galaxies for a range of galaxy types. He finds that early-type galaxies from E's to Sa's have similar absorption feature spectra. $H\alpha$ + [NII] and [SII] become prominent for Sb's and later types. In Sc's through irregulars, we see many more emission lines such as [OIII], $H\beta$ and [OII].

In our spectra, 10 galaxies had wavelength coverage for $H\alpha$ detection. $H\alpha$ emission was observed in 9 of those galaxies all of which had Bulge/Total values less than 0.06, consistent with late-type spirals. The one without $H\alpha$ detected had Bulge/Total=0.3 which is consistent with an early-type spiral galaxy. For these cases, our Bulge/Total measurements appear to be consistent with spectroscopic classifications for these galaxies.

Out of the 29 spectra for which redshifts could be determined, 23 showed emission lines while 6 were only absorption spectra. 91% of the emission line spectra galaxies had Bulge/Total \leq 0.2 and 67% of the absorption spectra had Bulge/Total \geq 0.2. Again, these statistics indicate that the majority of galaxies in our sample with measured spectra have spectral types consistent with their Bulge/Total measurements.

4.1.2. Comparison with Other Survey Galaxies

Morphology

It is interesting to compare the host galaxies of our compact nuclei with the entire sample of 1033 galaxies from the MDS, Groth strip, and HDF. As mentioned before, the measurement of Bulge/Total luminosity ratio gives us an estimate of the probable Hubble type for a galaxy. Figure 4.3 is the histogram of Bulge/Total values for the entire sample of galaxies in our survey. The hatched region is the true normalized histogram while the dotted line represents the fraction of galaxies found in each Bulge/Total bin defined in the previous subsection. This dotted line can be compared to the host galaxy Bulge/Bulge+Disk distributions in Figure 4.2. All of the possible host galaxy distributions in Figure 4.2 are weighted towards later-type galaxies as compared to the total galaxy sample. In Figure 4.3, a larger fraction of host galaxies have $0 \leq (B/B+D) < 0.5$ than survey galaxies. Although the largest fraction of survey galaxies also have $0 \leq (B/B+D) < 0.5$, there are many more with $0.5 \leq (B/B+D) < 1.0$ than what is seen in the host galaxy sample.

This apparent discrepancy could be attributed in part to incompleteness in detecting nuclei in galaxies with large bulges. We can correct for this effect using conservative completeness estimates from Figures 2.10 and 2.11 (90% completeness for $(B/B+D)=0$, 55% completeness for $0 < (B/B+D) \leq 0.4$, 43% for $0.4 < (B/B+D) \leq 0.8$, and 38% for $(B/B+D) > 0.8$). Adjusting our numbers in each $B/B+D$ bin accordingly indicates an increase in the number of host galaxies with $0.5 \leq (B/B+D) < 1.0$ from 6% to $\sim 10\% \pm 2.5\%$. This fraction is lower than the $\sim 15\%$ of all survey galaxies of this type. Based on this distribution, the host galaxies containing compact nuclei do appear to favor galaxies with bulges contributing less than 50% of the total galaxy light.

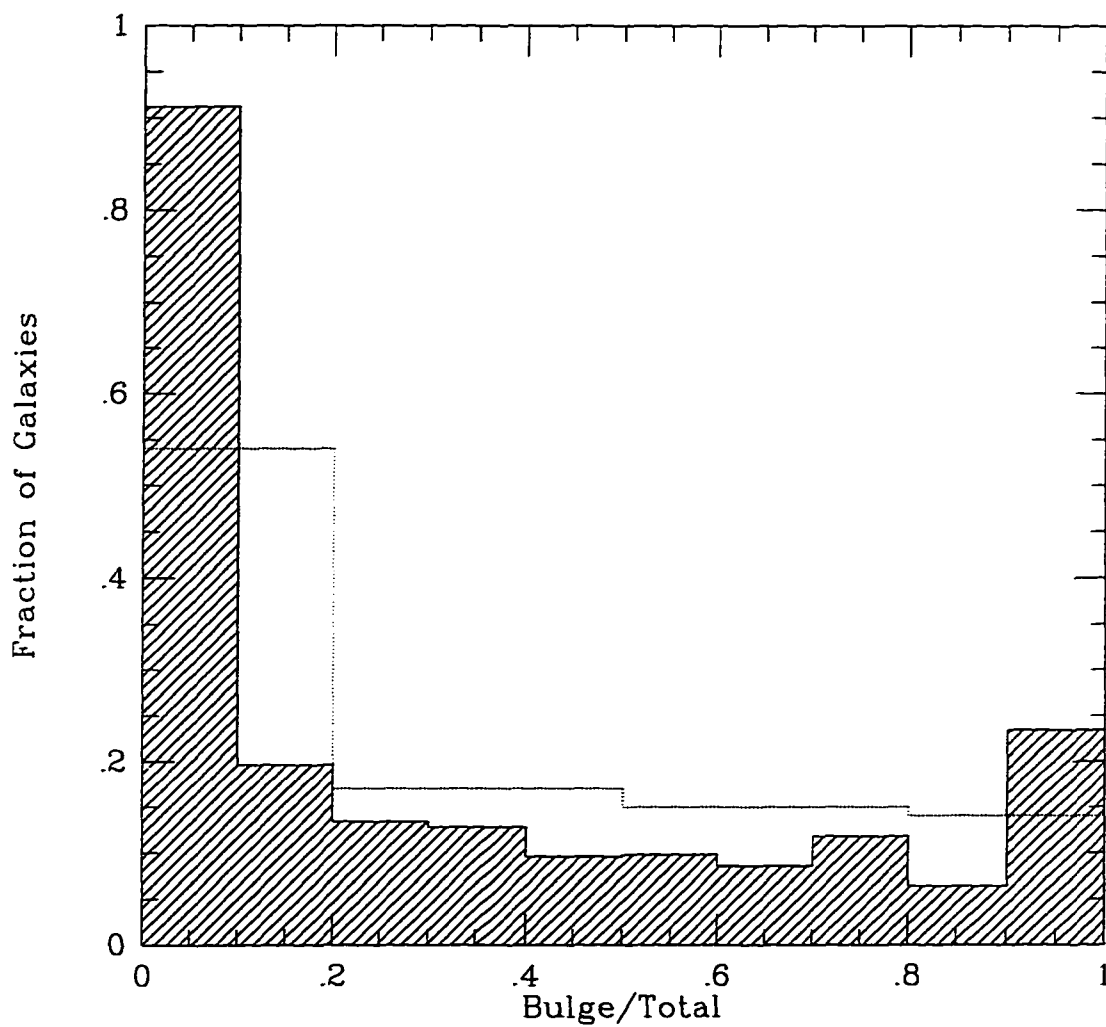


Figure 4.3 Histogram of measured Bulge/Total values for the 1033 galaxies in our survey (hatched region) normalized to 1=500. The dotted line represents the total fraction of galaxies in each Bulge/Total bin.

Size and Magnitude

We would also like to see how the compact nuclei galaxies vary in angular size and apparent magnitude as compared with the entire survey. Figure 4.4a shows the angular size in natural log of the half-light radius in arcsec vs. the apparent I band magnitude of the survey galaxies (open circles) and the host galaxies (filled circles). The typical limiting magnitude for MDS and Groth strip fields is $I \simeq 21.5$ and is apparent in the diagram. Most of the fainter galaxies are from the Hubble Deep Field. The smallest host galaxies are also from the HDF and are as small as 2 pixels ($0.2''$) in radius. It appears that few of the large but faint galaxies, possibly low surface brightness galaxies, appear to host point source nuclei. This trend is further revealed in Figure 4.4b which is the normalized distribution of the half-light radii for the host galaxies (hatched region) and the non-host galaxies (solid line). The host galaxy distribution peaks at a smaller half light radius ($h_{lr} \simeq 0.45''$) than the non-host galaxies ($h_{lr} \simeq 0.72''$) and also cuts off at a half-light radius of $\sim 1.9''$. A KS test conducted on both the size and magnitude distributions of the two populations indicates that they are drawn from different parent populations with a marginal significance of 80%. A possible explanation for this is that these galaxies may not contain enough mass to sustain a starburst nucleus or AGN. Additionally, some mechanism is usually required to transport fuel to the nucleus. Mihos et al. (1997) show through numerical simulations that low surface brightness galaxies are stable against the growth of bar instabilities, inhibiting a strong inflow of gas to the galaxy center for fueling a nuclear starburst or AGN. Although our nuclei are intrinsically faint, this observation implies that some limiting mass or ability to transport mass to the nucleus is necessary for their formation and duration.

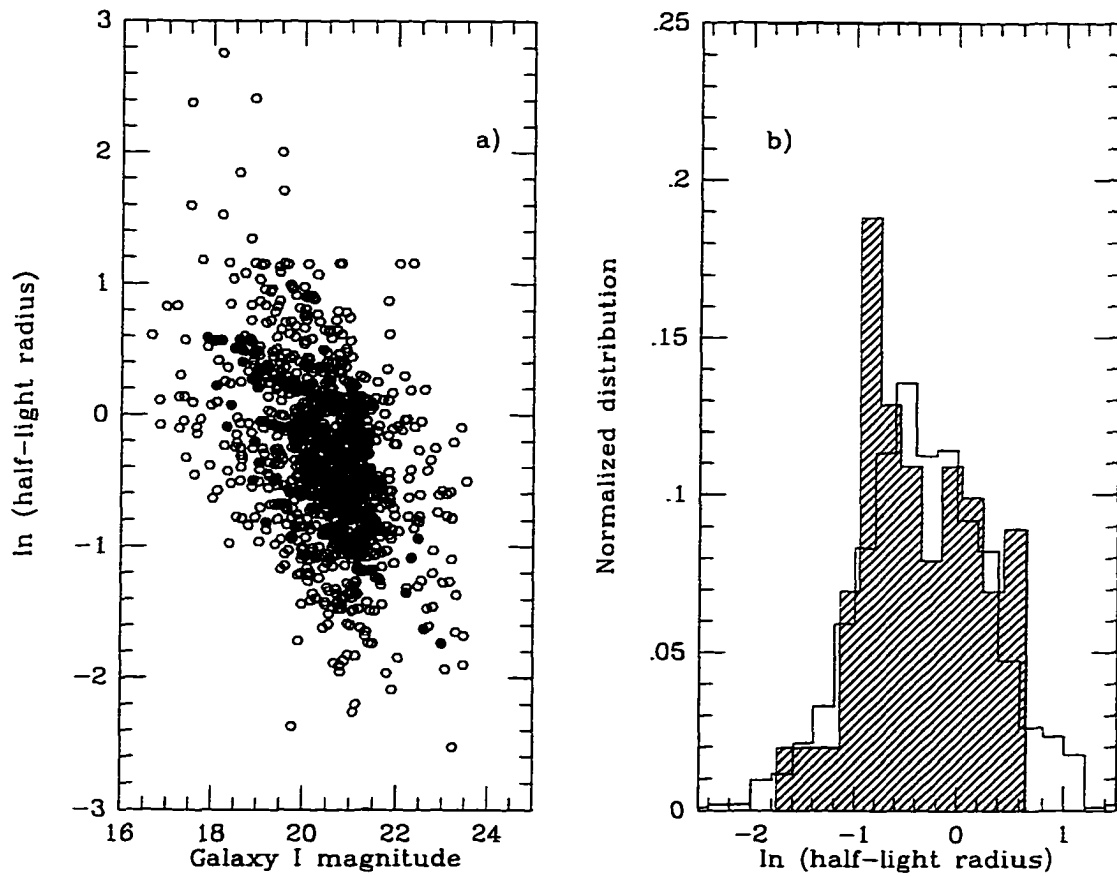


Figure 4.4 a) The galaxy I magnitude vs. the natural log of the half-light radius of the galaxy for all survey galaxies (open circles) and those galaxies containing compact nuclei (filled circles). b) The normalized distribution of half-light radii for all survey galaxies (solid line) and those containing compact nuclei (hatched region).

Axis Ratios

It has been observed that optically selected AGN nuclei avoid edge-on spirals (Keel 1980; McKleod & Rieke 1995). Figure 4.5 shows the distribution of axis ratios for the disks of our host galaxies. We have included in this diagram only those hosts that are disk-dominated, containing bulges less than 20% of the total galaxy light. The distribution is normalized by dividing the axis ratio distribution of host galaxies by the same distribution for the total sample of survey galaxies which are also disk-dominated. This normalizes the axis ratio distribution so that each bin represents the fraction of all disk-dominated galaxies with the specified axis ratio which contain compact nuclei. There is an observed drop in the fraction of hosts with disk axis ratios $(b/a) \lesssim 0.4$. However, this drop is much less significant than that observed in the spectroscopically selected CfA Seyferts. Lawrence and Elvis (1982) found that an inclination bias does not appear in hard X-ray selected samples of AGN. They conclude that selection biases seen in other samples are due to obscuration in a flattened disk parallel to the plane of the host galaxy. Although the axis ratio distribution of our data reveals a slight bias against edge-on host galaxies, our morphological selection technique appears to be less affected by this type of obscuration.

Galaxy Color

Finally, we would like to see how the colors of the host galaxies compare with the non-host galaxies. First we must understand the accuracy of the host colors. From Chapter 2 simulations, we realize that the bulge component of a host galaxy is often undetected when a nuclear point source is fit. We also see in Figure 2.7 that the point source magnitudes are well determined within the errors. Therefore, the

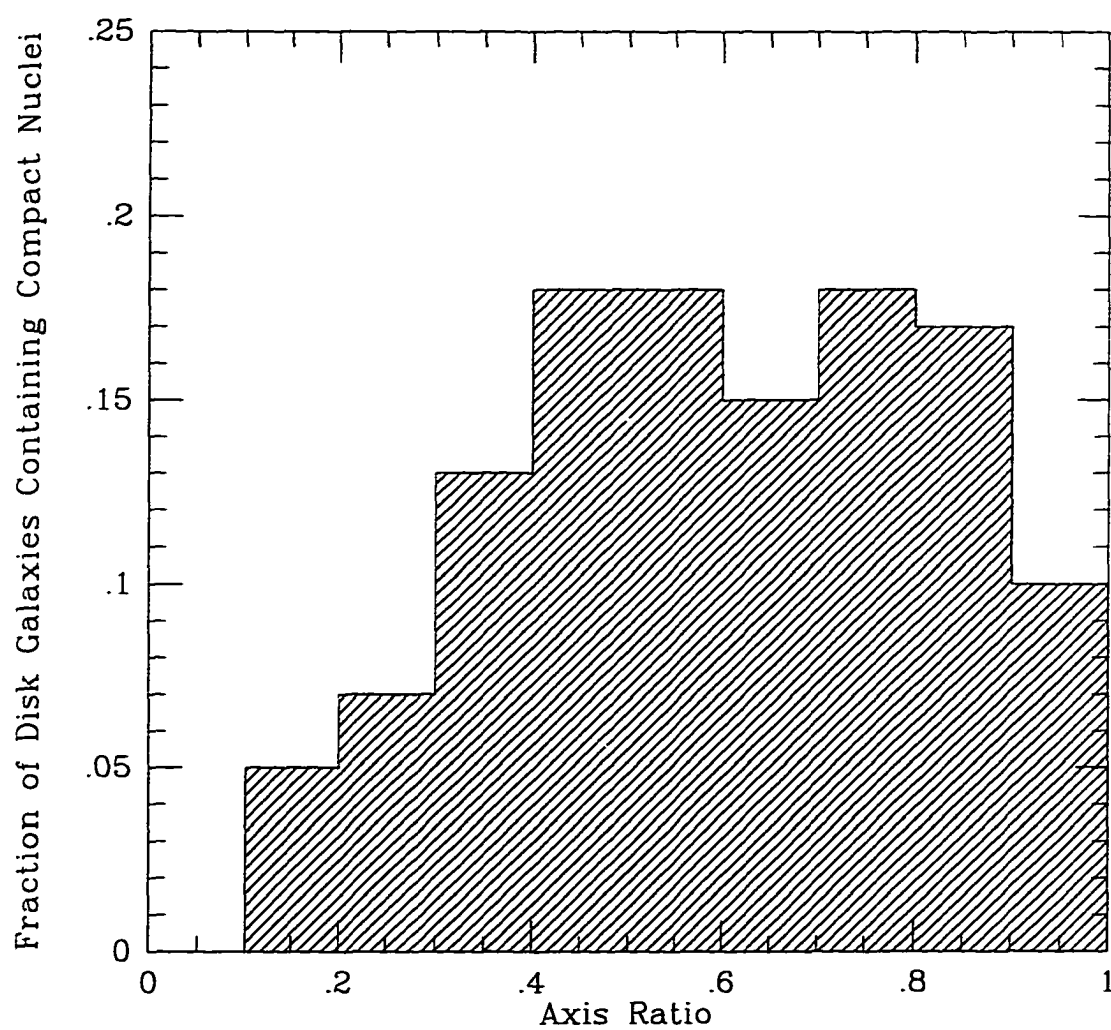


Figure 4.5 Histogram of the axis ratios for galaxies containing compact nuclei. The histogram is normalized by dividing by the axis ratio histogram for all spiral survey galaxies.

undetected bulge component does not appear to be mistakenly measured as part of the point source. How then does the missing bulge component effect the magnitude and consequently the color measurement for the host galaxy? We again look at the Monte-Carlo simulations of Chapter 2 to compare the *input* galaxy colors to those measured for the galaxy when a simulated point source is measured in the nucleus. In these simulations, the bulge component was often undetected when the point source was detected. For 389 galaxies in the simulation where the point source nucleus was detected (in both or only one filter) the mean error in the color of the host galaxy was $\simeq 0$ and the error in determining the color was $\sigma_{(V-I)}=0.37$. Since the mean error is zero, we are not seeing any trend in the color of the host galaxy which might be expected if the bulge were being completely ignored in the model fitting. Instead, when the bulge is not detected, it seems to be absorbed in the disk component such that the host galaxy color is not systematically affected. Keeping in mind the typical errors in determining the host galaxy color, we compare them to those of galaxies in our survey without unresolved nuclear components.

Figure 4.6a is the color-magnitude diagram for the galaxies in our survey where the open circles are non-host galaxies and the filled circles are the host galaxies. We have removed the color contribution of the nucleus from the integrated galaxy color to produce the host galaxy V-I color. In order to directly compare the sample of host galaxies with a similar representation of the survey galaxies, a random subset of the 1033 survey galaxies was selected based on the host galaxy distribution in Figure 4.2 (short-dashed line). This allows us to compare our host galaxy colors to those of survey galaxies morphologically similar to our hosts. Figure 4.6b shows the normalized histogram of the V-I colors of the compact nuclei host galaxies (hatched region) where the subset of similar survey galaxies is represented by the solid line. A KS test for these color distributions yields a KS probability of 0.43, where low

KS probabilities indicate that two populations are not drawn from the same parent distribution. This result indicates that the two distributions are not statistically different. The mean color for the host galaxies is measured at $\mu_{(V-I)}=0.970$ while the survey galaxies have $\mu_{(V-I)}=1.026$. The host galaxies tend to be slightly bluer than the general population of morphologically similar galaxies, although the color difference of 0.06 mag is not likely to be statistically significant. In general, we find that the host galaxy colors are like those of other morphologically similar galaxies in the field with a slight tendency to be bluer.

4.1.3. Host Galaxy Absolute Magnitudes

Using the spectroscopic and photometric redshifts for each galaxy containing an unresolved point source nucleus, we can examine the absolute magnitudes of the host galaxies as they compare with other galaxies. Figure 4.7a is the histogram of absolute rest-frame B magnitudes for the 101 host galaxies which contain unresolved nuclei using $H_0=75$ km/s/Mpc and $q_0=0$. The B-band luminosities for the galaxies were derived from their V magnitude, V-I color and redshift. This information is used to select a non-evolving model spectral energy distribution from the set described in Gronwall and Koo (1995). The models are based on those of Bruzual and Charlot (1993). The k-corrections are small (typically $\lesssim 0.3$ mag) since the V magnitude is roughly rest-frame B at the median redshift of our survey ($z \simeq 0.35$).

Our luminosity distribution peaks at $M_B \simeq -20.4$ which is approximately L^* . For comparison with the following samples, this corresponds to a peak at $M_B \simeq -21.3$ with $H_0=50$ km/s/Mpc. The luminosity distribution of normal spiral galaxies peaks at $M_B = -20.6$ ($H_0=50$ km/s/Mpc) (Christensen 1975), somewhat fainter than our sample of compact nuclei galaxies. Interestingly, Yee (1983) found the

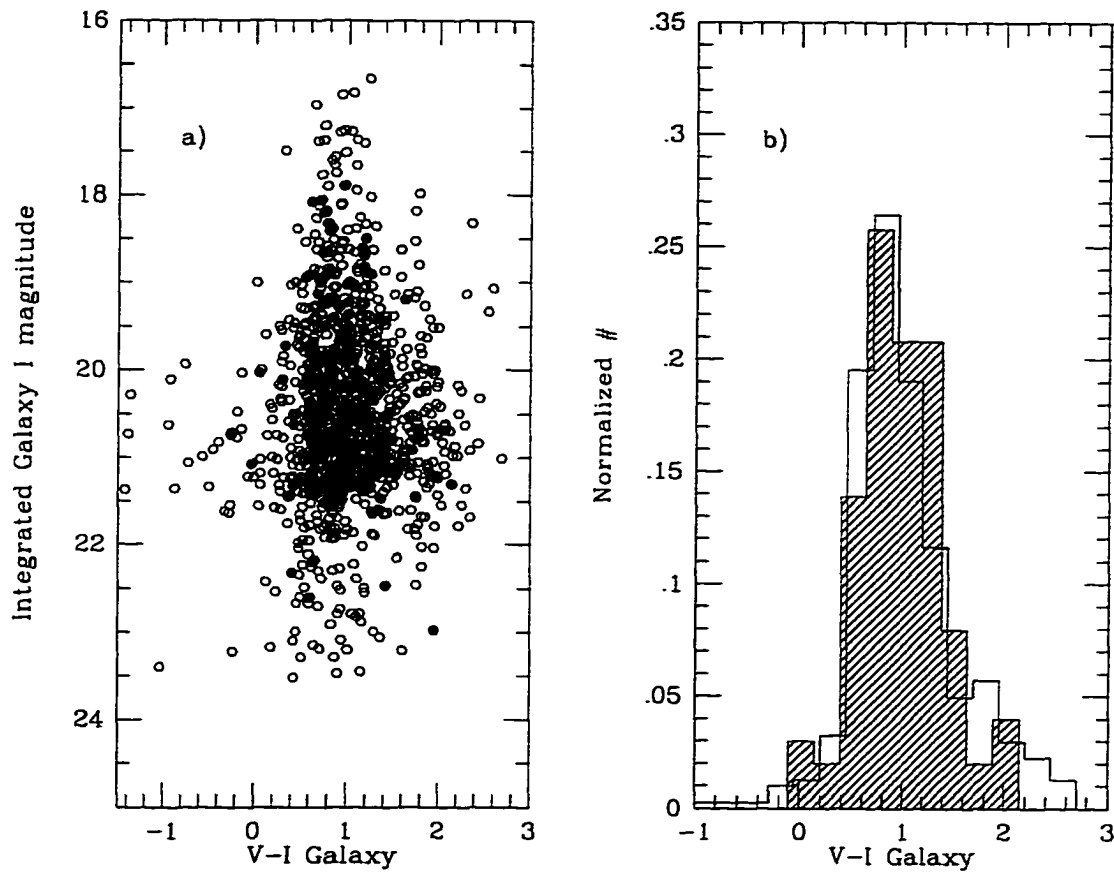


Figure 4.6 a) The color-magnitude diagram for galaxies in our survey where open circles represent non-host galaxies and filled circles represent those galaxies hosting a compact nucleus. b) The normalized histogram of galaxy V-I colors for the host galaxies (hatched region) compared with the normalized histogram of galaxy colors for a representative group of non-host galaxies of similar morphological type (solid line)

peak luminosity of Seyfert hosts from the Markarian survey to be $M_B = -21.3 \pm 0.8$ which is strikingly similar to our sample. From this observation he argues that the Seyfert phenomenon tends to occur more often in the luminous end of the spiral population. According to the present study, this trend may also hold true for galaxies hosting compact nuclei. This brighter absolute magnitude for AGN hosts is also seen, though to a lesser degree, for X-ray selected AGN where the peak luminosity is $M_B = -20.9$ (Kotilainen & Ward 1994).

We can compare our distribution to the dwarf seyfert nuclei hosts of Ho et al. (1997a) (Figure 4.7b) and the distribution of galaxies containing HII nuclei from Ho et al. (1997b) (Figure 4.7c) which were derived using $H_0 = 75$ km/s/Mpc. These samples provide an interesting comparison since the *nuclear* luminosities are closer to those of our sample than other spectroscopically selected AGN. The luminosity distributions are similar among the three samples. Although the peak luminosities are close, our sample does appear to drop off faster on the low luminosity side of the distribution. This is most likely caused by the nature of our magnitude-limited survey as it is observed over a range in redshift. As we observe at higher redshifts, intrinsically fainter galaxies are missed. Accounting for this discrepancy, we observe no evidence for evolution in the luminosity of AGN or starburst host galaxies out to $z \simeq 0.8$.

4.2. The Colors of the Point Source Nuclei: Clues to Their Nature

Model fitting of the point source component allows us to separate the color of the nucleus from that of the host galaxy. Of the 101 nuclear point sources detected, 93 were detected in the I filter image, 80 were detected in the V filter image, and 72

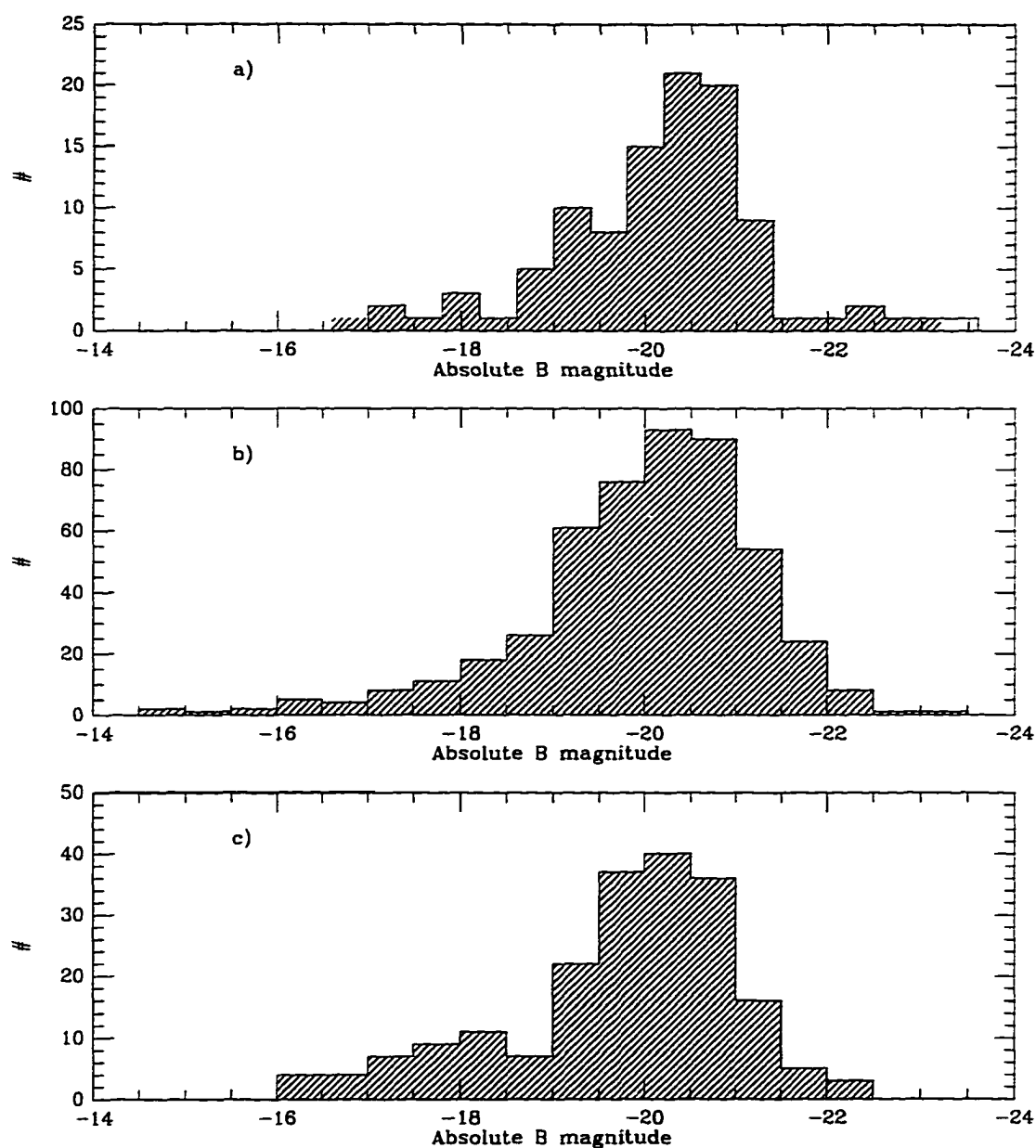


Figure 4.7 a) Histogram of rest-frame B absolute magnitudes for the host galaxies in our sample. b) Absolute B magnitudes from Ho et al. (1997a) of dwarf Seyfert nuclei hosts. c) Absolute B magnitudes from Ho et al. (1997b) of HII nuclei hosts.

were detected in both filters allowing for a V-I color to be determined. This result leaves 29 point sources with no color information. There are a few reasons for not detecting the point source in one of the filters such as 1) the point source is too faint in the other filter, 2) the point source does not converge properly in the other filter making its magnitude unreliable, and 3) the image is too noisy in the other filter for a point source to be detected. Of these 29, 5 were not detected in the other filter because of non-convergence of the model, 7 were not detected because of additional noise elements in the other filter, and 17 were not detected because the point source was too faint in the other filter. For these 17, we can determine a limit for the point source color assuming the point source in the other filter is fainter than 1% of the total galaxy light. For the other 12 point sources detected only in one filter, we cannot estimate the nuclear color and they will be omitted from the discussion in this section.

Figure 4.8a shows the V-I colors of the point source nuclei vs. their host galaxy V-I colors. Here we have plotted the 72 points having color information with their appropriate error bars. The 17 points with a point source color limit, due to non-detection in one filter, are marked with an arrow. Within the errors of the point source colors, the majority of point source nuclei are the same color as the underlying host galaxy. The large errorbars on the point source colors cause the correlation coefficient between the point source and host galaxy colors to be small indicating a low probability of correlation. In Figure 4.8b we show the generalized histogram of color differences between the host and point source where point sources bluer than the host are positive and those redder than the host are negative. This histogram is made by allowing each point to be represented as a gaussian with the calculated 1σ error defining the width of the gaussian. The histogram is the summation of these gaussians. It does not include the 17 points

with only color limits. The peak of this distribution occurs at $\mu=-0.05$, essentially zero, and the FWHM of the distribution is 1.52. The nuclear colors are in general the same as the host galaxy colors with a large spread in the distribution. Nuclei which appear bluer than the host can be explained as either young starburst nuclei or unobscured AGN. However, a nucleus can appear redder than the host if there is sufficient dust present or excess star formation in the disk causes the underlying galaxy to appear bluer.

In addition to the nuclear color vs. host galaxy study, it is also interesting to see how the nuclear colors compare with the color of the bulge where it is detected in both the V and I filters. Again, we first must understand the errors in the bulge colors as determined from the Monte-Carlo simulations. Based on comparison of the input bulge colors of the simulation galaxies to the measured bulge colors when a point source nucleus is detected, we determine the error in bulge color to be $\sigma_{V-I}=0.85$. This error is large but not unexpected since the bulge component appears to be the most difficult to measure accurately when a point source nucleus is detected in the galaxy. Again, there is no systematic color difference in the bulges observed in the simulation galaxies when a point source is detected. We apply the determined color error for bulges to our data to investigate any trends in the relationship between the nuclear and bulge colors.

Figure 4.9a is the point source color vs. the bulge color for the 17 galaxies where both a point source and bulge color were measurable. We have applied the determined bulge color error and point source color errors. Because these errorbars are so large, this figure is not useful for studying individual cases. In Figure 4.9b we show the generalized histogram of the color difference between the point source and bulge components. The histogram is made in the way described for Figure

4.8b. This figure allows us to observe any trends in the color difference while taking into account the errors in the individual points. The mean color difference between the bulge and the point source nucleus is $(V-I)_{bulge} - (V-I)_{nucleus} \simeq 0.5$. This indicates that in general, the nuclear colors are bluer than the bulge. This is expected if the bulge represents an older population than the nucleus or if the nucleus has typical non-thermal source colors.

Studying the nuclear colors allows us to look more deeply into the question of their nature. In the case of detection in a bulge dominated system, the color of the nucleus plays a role. As discussed above, we require the nucleus to be a different color from that of the underlying bulge to ensure that it is not merely an unresolved region of the bulge. Other than Seyferts and starbursts, what other objects could appear unresolved in an elliptical or bulge dominated galaxy and would be composed of a different stellar population from that of the bulge so that it would appear a different color? One additional possibility is a merger remnant. Theoretical and observational evidence suggests that major mergers, where the galaxies are of almost equal mass, form elliptical remnants (Hibbard et al. 1994 and references therein). In the case of the merger remnant NGC 3921, an unresolved nucleus is observed in an $r^{1/4}$ profile galaxy (Schweizer 1996). The color gradient of the remnant indicates a redder nucleus than the remaining galaxy body. Such remnant nuclei could exist in our sample, although the small number (6%) of elliptical hosts suggests they would be a minor contributor to the population. There is also the possibility that minor merger remnants in the centers of galaxies could reveal themselves as unresolved nuclei of a different stellar population than the host galaxy. It is unclear at this time how often such an object might occur in our survey.

With the spectroscopic and photometric redshifts of each host determined, we can examine any trends in the nuclear colors with redshift. This information is important in determining the true nature of the nuclei. Figure 4.10 shows the V-I colors of the nuclei plotted against their determined redshift. Errorbars in the redshift direction clearly differentiate between those objects with photometric redshifts ($\sigma_z \simeq 0.9$) and those with spectroscopic redshifts. Open circles are those point sources with only limiting color information. To interpret this figure, we must understand how the colors of starbursts, AGN or any other stellar population thought to be present in our nuclear sample behave as a function of redshift. This modeling is explored in the following section.

4.3. Synthetic V-I colors for AGN and Star Clusters: Comparison with the Nuclear Colors

The V-I colors of the point source nuclei in our sample provide important information to help us to understand their nature. To determine if the nuclei are starbursts or AGN, we must first understand the colors of these different objects. Most starburst and AGN photometry (other than of bright QSO's) has been done at low redshifts. To simulate the effects of K-corrections on the object colors and therefore provide a more realistic comparison with our data, we use representative spectra to calculate synthetic V-I colors for AGN and starbursts with the HST V and I filters.

The spectra used for this simulation have been taken from the literature. To simulate colors for the AGN nuclei, we use synthetic spectra from Kalinkov et al. (1993) representative of Seyfert 1, Seyfert 1.5 and Seyfert 2 galaxies where the nuclear activity dominates the spectrum. The spectra were produced by

averaging the spectra of several reliably classified AGN in each class to produce a representative spectrum. Figure 4.11 shows each of the spectra in arbitrary flux units of $\text{ergs s}^{-1} \text{ cm}^{-2} \text{ \AA}^{-1}$.

Spectra of star clusters of various ages are used to simulate the color of starburst nuclei in our sample. These spectra will simulate the appearance of certain isochronic stellar populations present in the nuclei sample. The spectra are from E. Bica and are available as part of a database of spectra for galaxy evolution models (Leitherer et al. 1996). Figure 4.12a is an integrated spectrum of HII regions, representing a very young population or current starbursting nucleus. Figure 4.12b represents a star cluster with $\text{age} \simeq 10 \text{ Myr}$ and $[Z/Z_{\odot}] \simeq -0.25$. Figure 4.12c represents a star cluster with $\text{age} \simeq 25 \text{ Myr}$ and $[Z/Z_{\odot}] \simeq -0.4$. The ages of the star cluster spectra shown in Figure 4.12d through 4.12f are 80 Myr, 200-500 Myr and 1-2 Gyr, respectively. Their respective metallicities are -0.5, -0.6 and -0.5. The flux units are in $\text{ergs s}^{-1} \text{ cm}^{-2} \text{ \AA}^{-1}$.

To simulate the effects of redshift in our sample, each of the spectra in Figures 4.11 and 4.12 were stepped incrementally in redshift to $z \sim 0.8$. The IRAF task CALCPHOT was then used to determine the V-I colors of each of the spectra at the range of redshifts. CALCPHOT utilizes the HST V (F606W) and I (F814W) filter response which is convolved with the spectra to produce accurate synthetic colors.

Figure 4.13 shows the V-I colors for the 3 types of Seyfert galaxies as a function of redshift. The solid line is the Seyfert 2 color, the short dashed line is the Seyfert 1.5 and the long dashed line is the Seyfert 1. Comparing this figure to Figure 4.10 allows us to determine which point source nuclei are consistent with Seyfert-like galaxy nuclei. The majority of nuclei are consistent with the Seyfert colors within

the errorbars. As a reference, we note the 2 spectroscopically identified Seyfert 1s in our sample at $z=0.45$, $V-I=0.89$ and $z=0.99$, $V-I=0.22$. These points are consistent with the Seyfert 1 colors (long dashed line). Of the 89 point source nuclei with measurable colors or color limits, 8 are too blue to be consistent with the Seyfert colors and 8 are too red (based on 1σ errors). These red points may be consistent with Seyfert nuclei colors containing moderate amounts of reddening due to dust.

In Figure 4.14 we show the $V-I$ colors for the various star cluster spectra shown in Figure 4.12 as a function of redshift. The solid line is the integrated HII region color. This locus represents the color a young starburst would have in our sample. The color varies with redshift as different emission lines in the spectrum pass through the V and I filters. The dramatic reddening decrease in the HII region color at a redshift of ~ 0.35 is caused by the 4959\AA and 5007\AA [OIII] and $H\beta$ emission lines moving into the V filter. The remaining lines are as follows: the short dashed line is the 10 Myr cluster, the long dashed line is the 25 Myr cluster, the dot-short dashed line is the 80 Myr cluster, the dot-long dashed line is the 200-500 Myr cluster, and the dotted line is the 1-2 Gyr cluster. The decrease in the HII color at $z\sim 0.35$ is the most striking difference between the HII color and that of the remaining intermediate age clusters and the Seyfert colors of Figure 4.13.

Comparing this figure with Figure 4.10, we see that the majority of our point source nuclei are also consistent with the colors of intermediate aged star clusters. Some of the point source nuclei, which were inconsistent with Seyferts because of their blue colors, lie in the $z\lesssim 0.4$ region where they are consistent with the young starburst, HII-like colors. Of the 8 galaxies which are too blue to be Seyferts, 5 fall in this region of the redshift-color diagram. Another one of these 8 point

sources ($z=0.60, V-I=-0.10$) has a color consistent with that of a 25 Myr old cluster. Together, these 6 point sources have colors more consistent with that of a star cluster than a Seyfert nucleus. The other 2 point sources too blue to be Seyferts are also inconsistent with the star cluster colors.

The synthetic colors show that the vast majority of the nuclei in our sample have colors consistent with Seyfert-like nuclei and also consistent with intermediate aged star clusters. A small number (6 out of 89) have colors too blue to be Seyferts but are consistent with young or intermediate aged star cluster colors. These 6 are likely to be starburst nuclei in our sample. The main population, however, cannot be identified explicitly as either Seyfert-like or starburst-like based on the $V-I$ color alone. We assume that the remaining sample of 95 point sources, which includes the 12 point sources with no measurable color, consists of some combination of starbursts and Seyfert nuclei. The remaining 95 point sources represent an upper limit sample of AGN-like nuclei. In the next chapter, this sample is used to determine an upper limit on the AGN luminosity function at low luminosities.

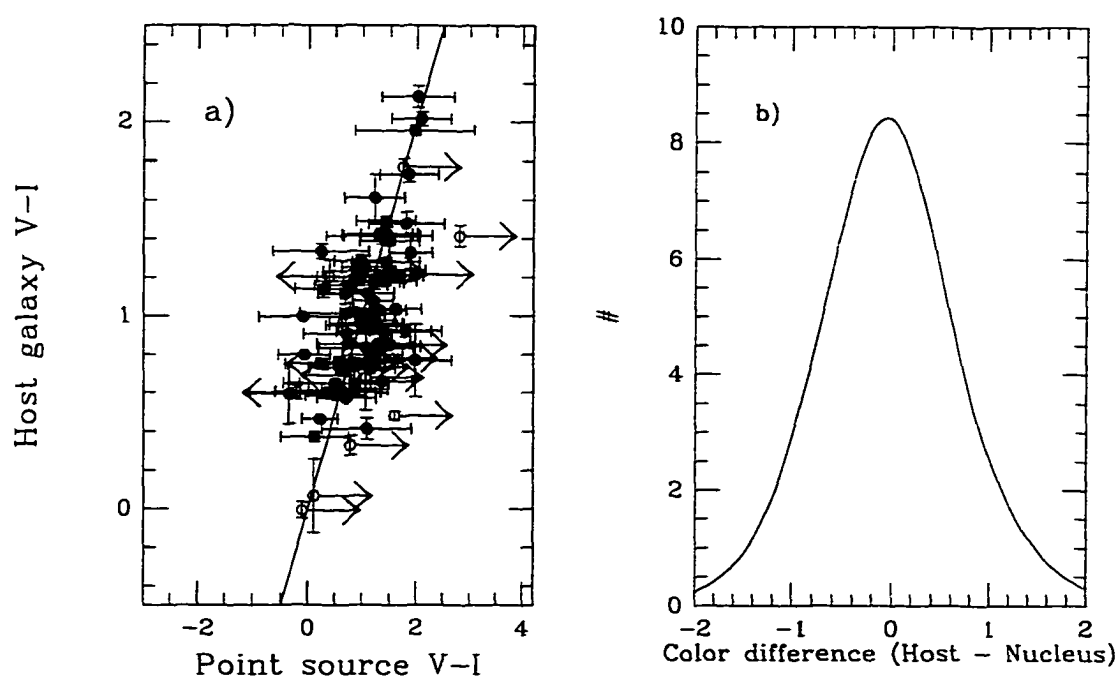


Figure 4.8 a) The point source V-I color vs. the host galaxies V-I color. Points measured in only one filter are shown as color limits. b) The generalized histogram of the color difference between the host galaxy and the point source.

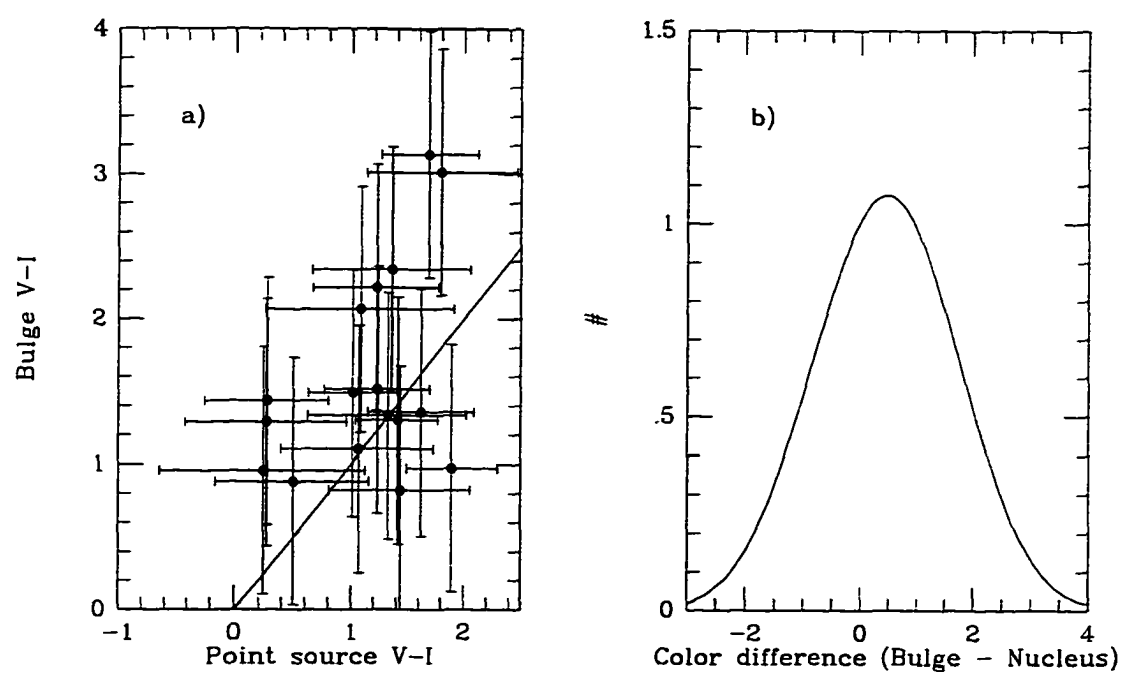


Figure 4.9 a) The point source V-I color vs. the bulge V-I color for the 17 galaxies containing a measureable bulge and point source color. b) The generalized histogram of the color difference between the bulge and the point source nucleus.

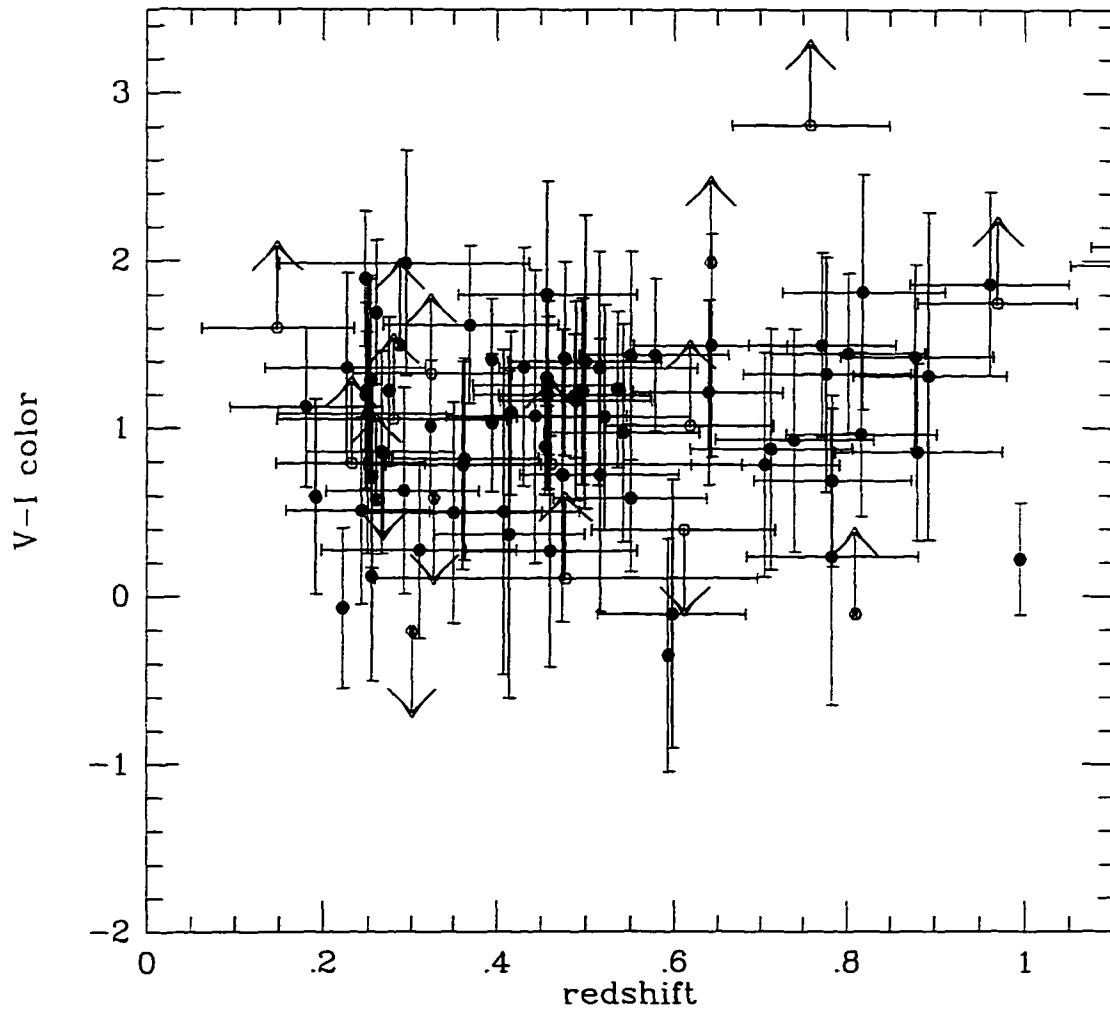


Figure 4.10 The redshift vs. the V-I color of the unresolved nuclei. The open circles are those nuclei with color limits.

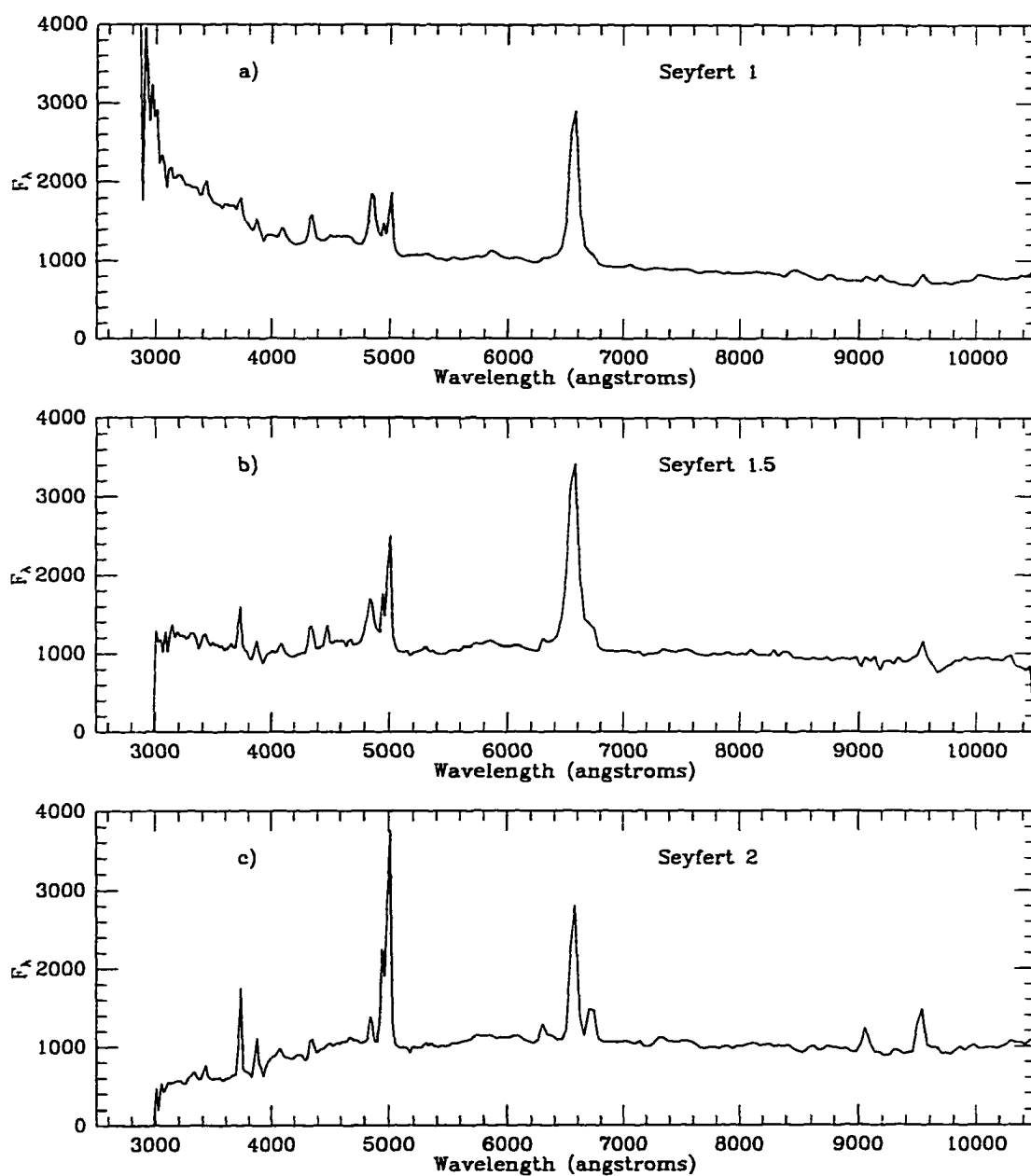


Figure 4.11 a) Seyfert 1 spectrum produced by averaging several reliably classified Seyfert 1 galaxies (Kalinkov et al. 1993). b) Seyfert 1.5 galaxy spectrum. c) Seyfert 2 galaxy spectrum.

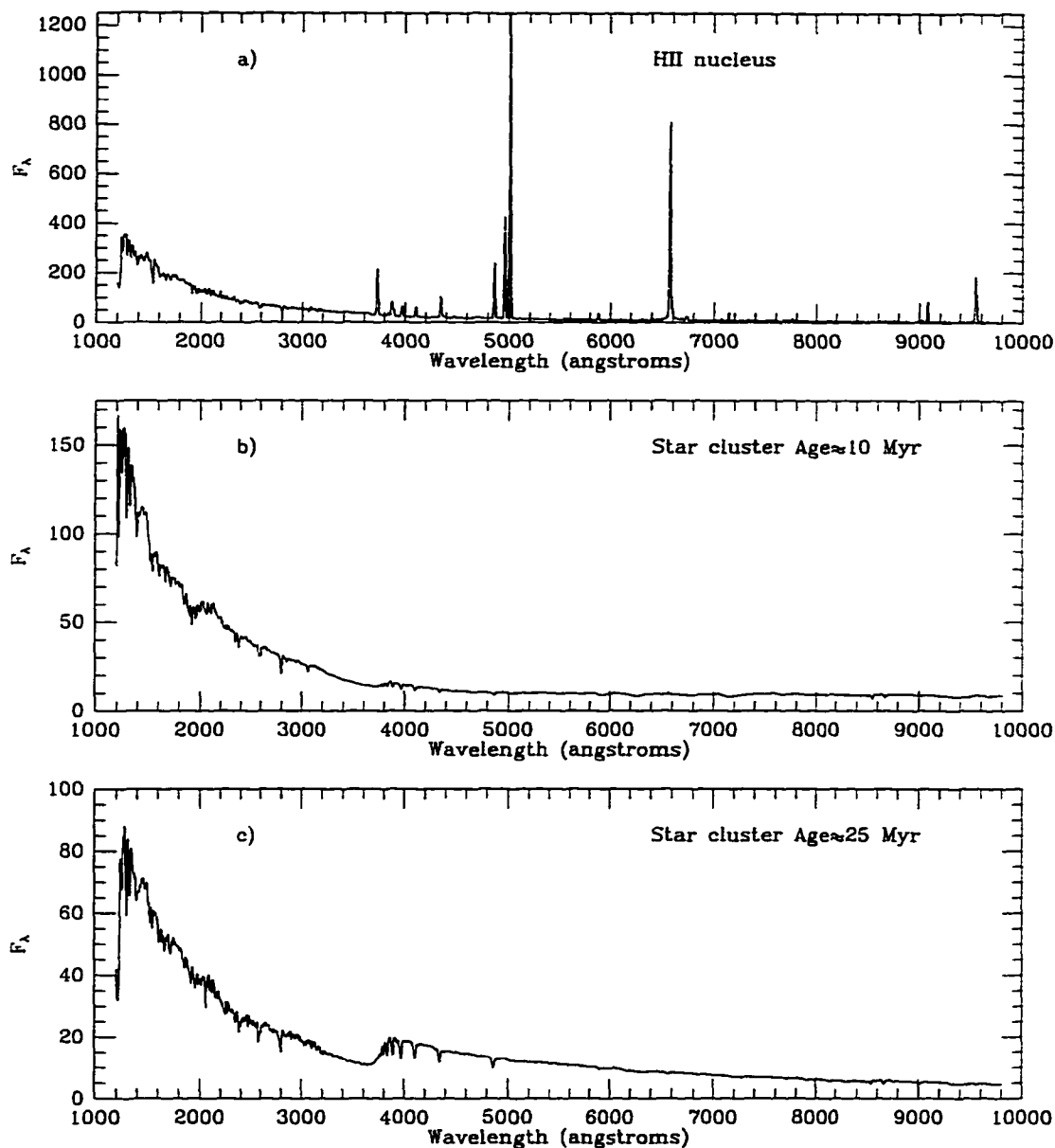
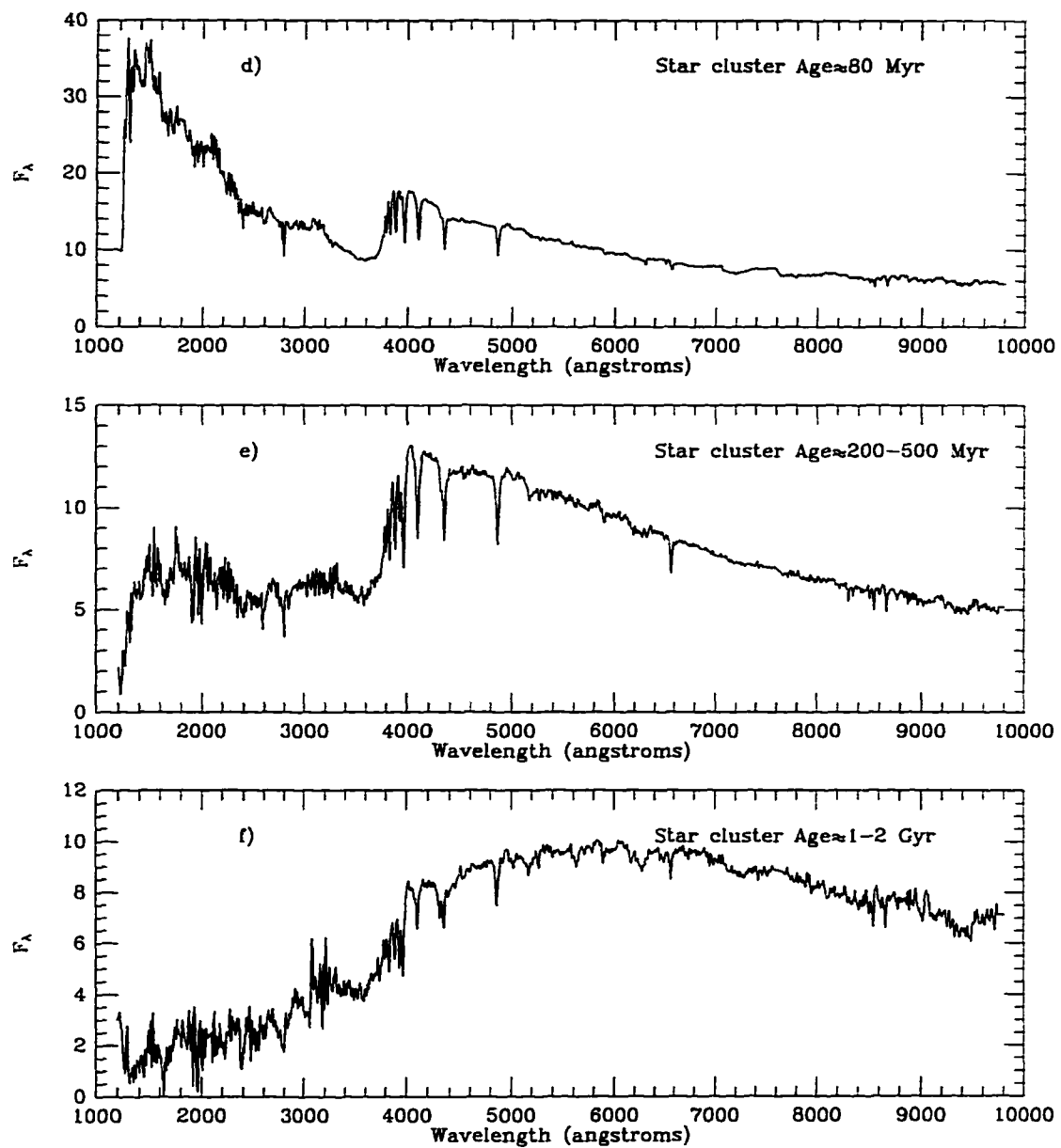


Figure 4.12 a) HII nucleus. b) age ≈ 10 Myr star cluster with $[Z/Z_\odot] \approx -0.25$. c) age ≈ 25 Myr star cluster with $[Z/Z_\odot] \approx -0.4$. d) age ≈ 80 Myr star cluster with $[Z/Z_\odot] \approx -0.5$. e) age ≈ 200 -500 Myr star cluster with $[Z/Z_\odot] \approx -0.6$. f) age ≈ 1 -2 Gyr star cluster with $[Z/Z_\odot] \approx -0.5$. All spectra are from E. Bica in Leitherer et al. (1996).



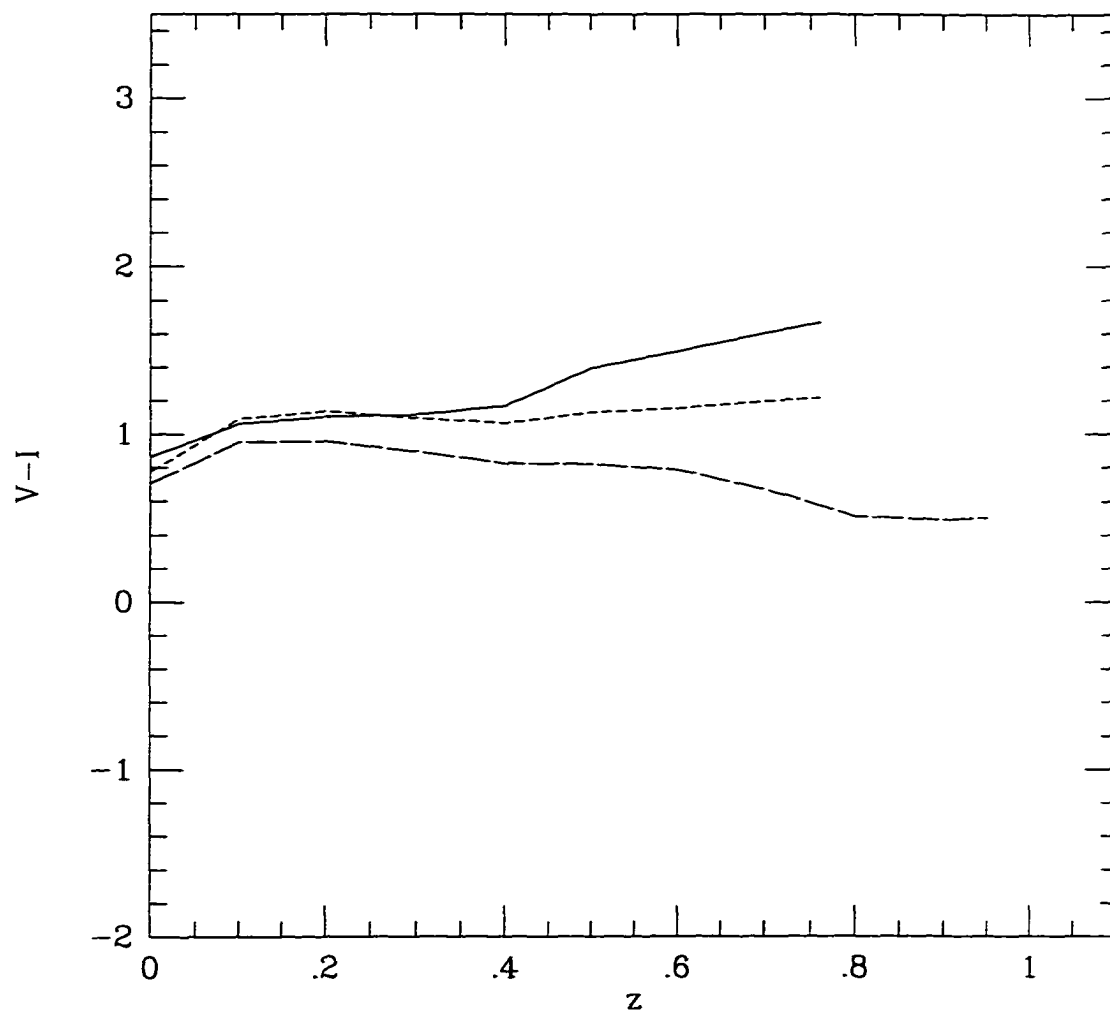


Figure 4.13 V-I colors for the 3 types of Seyfert galaxies as a function of redshift. The solid line is the Seyfert 2 color, the short dashed line is the Seyfert 1.5 and the long dashed line is the Seyfert 1.

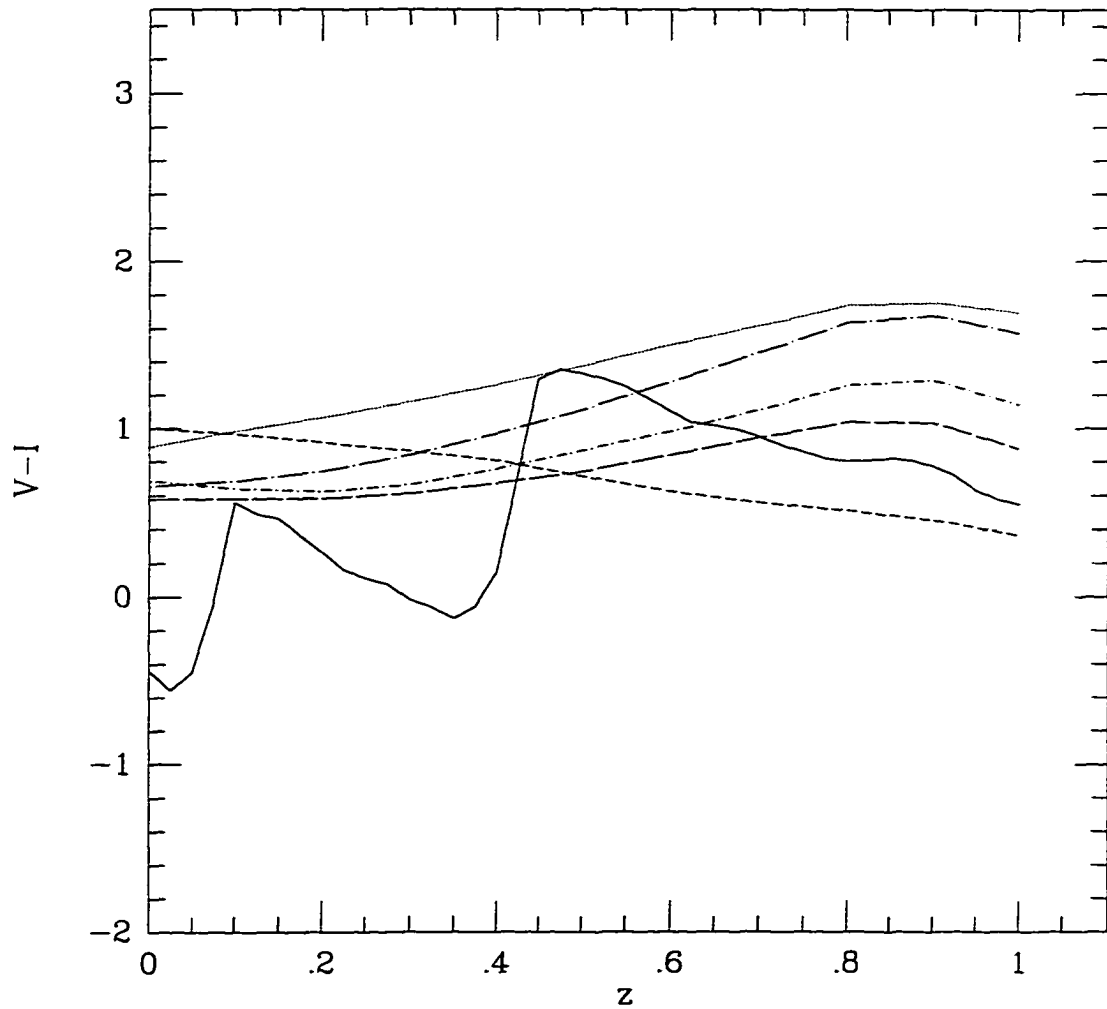


Figure 4.14 V-I colors for the various star cluster spectra shown in Figure 4.12 as a function of redshift. The solid line is the integrated HII region color, the short dashed line is the 10 Myr cluster, the long dashed line is the 25 Myr cluster, the dot-short dashed line is the 80 Myr cluster, the dot-long dashed line is the 200-500 Myr cluster, and the dotted line is the 1-2 Gyr cluster.

CHAPTER 5

THE NUMBER DENSITY AND LUMINOSITY FUNCTION FOR UNRESOLVED NUCLEI

The luminosity function of AGN as a function of redshift provides much needed information about how this population of objects changes with time. Understanding the population as a whole may allow us to understand better the physics of QSOs. In addition, accurate knowledge of the AGN LF is important for understanding their contribution to the soft X-ray background.

The bright end of the QSO LF has been well studied as a function of redshift (e.g. Hartwick & Schade 1990, and references therein). To study the faint end, Seyfert galaxies have been observed locally through spectroscopic surveys (Huchra & Burg 1992). However, these surveys tend to include only bright Seyfert nuclei that dominate the galaxy light. Fainter nuclei would not be spectroscopically selected since the host galaxy light would dilute the nuclear

emission. Morphologically, such faint nuclei can be detected if the nuclear light can be disentangled from the host galaxy. In this study we have separated the nuclear and galaxy light using 2-dimensional maximum likelihood galaxy modeling. This method allows us to study unresolved nuclear sources in galaxies out to moderate redshifts to fainter limiting magnitudes than previously observed.

Before constructing the luminosity function, we first compare the fraction of galaxies containing compact nuclei with the fraction of Seyfert galaxies determined locally and at moderate redshifts. As mentioned previously, Huchra & Burg (1992) (hereafter HB) have studied local Seyferts from the CfA redshift survey and find the percentage of galaxies containing Seyfert 1 and 2 nuclei to be $\sim 2\%$. Their study included Seyfert nuclei extending to $M_B \lesssim -17$. Maiolino & Rieke (1995) examined a sample of Seyfert galaxies closer than the CfA sample and were able to detect fainter nuclei since the nuclear spectra were less diluted by the host galaxy light. They found the percentage of Seyferts to be 5% and possibly as high as 16%. The majority of the additional objects in this study were Seyfert 2s which are underluminous in the optical with respect to type 1 Seyfert nuclei. Active nuclei were detected in this study to $M_B \lesssim -16$. From Chapter 2, we find the fraction of all galaxies in our survey containing compact nuclei to be $16 \pm 3\%$ including nuclei $\geq 3\%$ of the galaxy light corrected for incompleteness. This fraction is very similar to that found by Maiolino & Rieke for local Seyferts, although our sample includes nuclei at least a magnitude fainter in absolute magnitude.

Ho et al. (1997a) find the percentage of local galaxies containing faint Seyfert nuclei to be 11% with LINERs (low-ionization nuclear emission line regions) occupying an additional 19% of galaxies. They find the fraction of galaxies containing HII nuclei to be 42% of all galaxies. These nuclei are extremely faint

based on their emission line luminosities ($L(\text{H}\alpha) \leq 10^{40} \text{ ergs s}^{-1}$). Many of these nuclei are too faint for morphological detection as a stellar-like point source in the host galaxy and were identified based on emission lines alone. These results are intriguing as they suggest that the possible fraction of local galaxies containing low-luminosity active nuclei may be as high as 30% (including LINERS). Since optical integrated magnitudes for these AGN and HII nuclei have not been determined, we cannot directly compare the fraction of galaxies in the present study containing compact nuclei with the fraction of galaxies containing faint AGN and HII nuclei from Ho et al.

At moderate redshifts ($z \leq 0.3$), Tresse et al. (1996) have searched for evidence of nuclear activity in the Canada-France Redshift Survey (CFRS) and find that 17% of all galaxies have emission line flux ratios consistent with active nuclei galaxies. Since these objects are spectroscopically selected, this survey contains only those nuclei which dominate the host galaxy light such that their emission lines are not greatly diluted by the underlying galaxy. When they correct for possible stellar absorption of the Balmer lines due to the host galaxy, the fraction of galaxies displaying activity is 8%. Their results are somewhat inconsistent with those of Maiolino & Rieke since the fraction of higher redshift galaxies containing active nuclei identified by Tresse et al. appears to be less than that for local Seyfert nuclei. Such inconsistencies highlight the need for space density studies of LLAGN at moderate redshift.

In this chapter we address the space density of galaxies containing compact nuclei in the MDS, Groth strip and HDF by constructing luminosity functions at two different redshift slices to search for signs of possible evolution. We then compare our LFs with those of local Seyferts and local to moderate redshift

quasars.

5.1. The Upper Limit Luminosity Function for LLAGN

In Chapter 4 we selected a subsample of our compact nuclei which have colors consistent with those of Seyfert nucleus-dominated galaxies based on synthetic photometry of representative spectra. However, the colors are also consistent with intermediate aged starburst nuclei making this subsample an upper limit estimate on the number density of AGN in this survey. This subsample can be used to construct the upper limit luminosity function for faint AGN out to redshifts of $z \simeq 0.8$, providing the first look at the shape and parameters of the AGN LF in this luminosity and redshift regime.

5.1.1. LF Calculation

To calculate the luminosity function for our sample of 95 compact nuclei with colors consistent with AGN-like nuclei, we use the $1/V_A$ technique described fully in Schmidt and Green (1983) where V_A is the accessible volume in which each object can be observed. This technique allows us to calculate the space density of the compact nuclei as a function of their absolute magnitudes and redshifts. This quantity is symbolically defined as $\phi(M, z)$. To calculate absolute magnitudes from the nuclear apparent magnitudes we use the equation

$$M_B = B - 5 \log A(z) + 2.5(1 + \alpha) \log(1 + z) - 5 \log(c/H_o \times 10^6) + 5 \quad (5.1)$$

where B is the apparent magnitude, c is the speed of light in km/s, H_o is the Hubble constant in $\text{km s}^{-1} \text{Mpc}^{-1}$, and α is the spectral index defined by

$$F_\nu \propto \nu^\alpha \quad (5.2)$$

The quantity $A(z)$ is the bolometric luminosity distance defined as

$$A(z) = z \left\{ \frac{1 + z(1 - q_o)}{[(1 + 2q_o z)^{1/2} + 1 + q_o z]} \right\} \quad (5.3)$$

The term $2.5(1+\alpha)\log(1+z)$ in equation 5.1 represents the effect of the redshift on measurements through a fixed color band (i.e. the K-correction). Since we do not have apparent B magnitudes, we determine them from the apparent V magnitude and the spectral energy index, α , according to the following equation

$$B - V = \alpha 2.5 \log_{10}(\lambda_B / \lambda_V) \quad (5.4)$$

where $\lambda_B=4500\text{\AA}$ and $\lambda_V=6060\text{\AA}$ for the HST filters. We assume the width of the filter bands to be comparable. Using this equation with $\alpha=-1.0$ yields $B-V=0.32$. We use α of -1.0 or -0.5 in later calculations for direct comparison with other LFs in the literature. Based on the spectra for Seyfert-nucleus dominated galaxies used in Chapter 4, their rest frame B-V colors are 0.34, 0.50 and 0.71 for Seyfert 1, 1.5 and 2 galaxies respectively. Our choice of α for the sake of comparison may be somewhat blue for the typical object in our survey, however, the choice of magnitude bin sizes is much larger than this error in the magnitude.

The absolute magnitude of each point source in the sample is determined according to the above equations. With the absolute magnitude we determine the maximum redshift at which the point source would be observable in each of our 70 WFPC2 fields. The limiting point source magnitude per field is determined for each object by calculating its apparent magnitude had it been detected in a galaxy at the limiting galaxy magnitude of each field (see Table 2.2). This point source limiting apparent magnitude per field is based on the observed percentage of galaxy light contained within the nucleus. The maximum redshift per field is then used, in combination with the total area of the field in steradians, to determine the

comoving volume over which each object is observable in each survey field. The summation of the volumes for each field is the accessible volume for that particular object. The quantity ϕ is then determined as a function of absolute magnitude and redshift through the following summation

$$\phi(M, z)dM = \sum_{j=1}^n \frac{1}{V_a^j} \quad (5.5)$$

for $z_j \in (z_1, z_2)$ and $M_j \in (M_1, M_2)$ where $M_1 = M - dM/2$, $M_2 = M + dM/2$, $z_1 = z - dz/2$, and $z_2 = z + dz/2$. The integer j denotes individual galaxies in each absolute magnitude and redshift bin. In this way, the number density is determined for a discrete luminosity interval and a discrete redshift interval.

Because of the large errorbars in redshift for the photometrically determined objects in our sample, an additional consideration is made in determining the luminosity function. We allow each individual object to be viewed as a Gaussian distribution of itself in redshift space. To do this in the LF calculation, each point is represented as 60 points spread over $\pm 3\sigma$ of the redshift range. Each of the 60 points is weighted according to a Gaussian distribution so that the points near the central redshift are weighted highest, those near the 3σ limits are weighted lowest, and the summation of all 60 points is equal to 1.0 (see Figure 5.1). In this way, each object is spread over its appropriate luminosity range in the LF calculation. The determination of ϕ is then computed by

$$\phi(M, z)dM = \sum_{k=1}^n \frac{(Weight)}{V_a^k} \quad (5.6)$$

so that only the appropriately weighted portion of each point is considered in the number density calculation in each specific luminosity and redshift interval. The value of k represents the individual fractions of each galaxy so that n is the number of galaxies multiplied by 60, the number of divisions in redshift space over which each point is distributed.

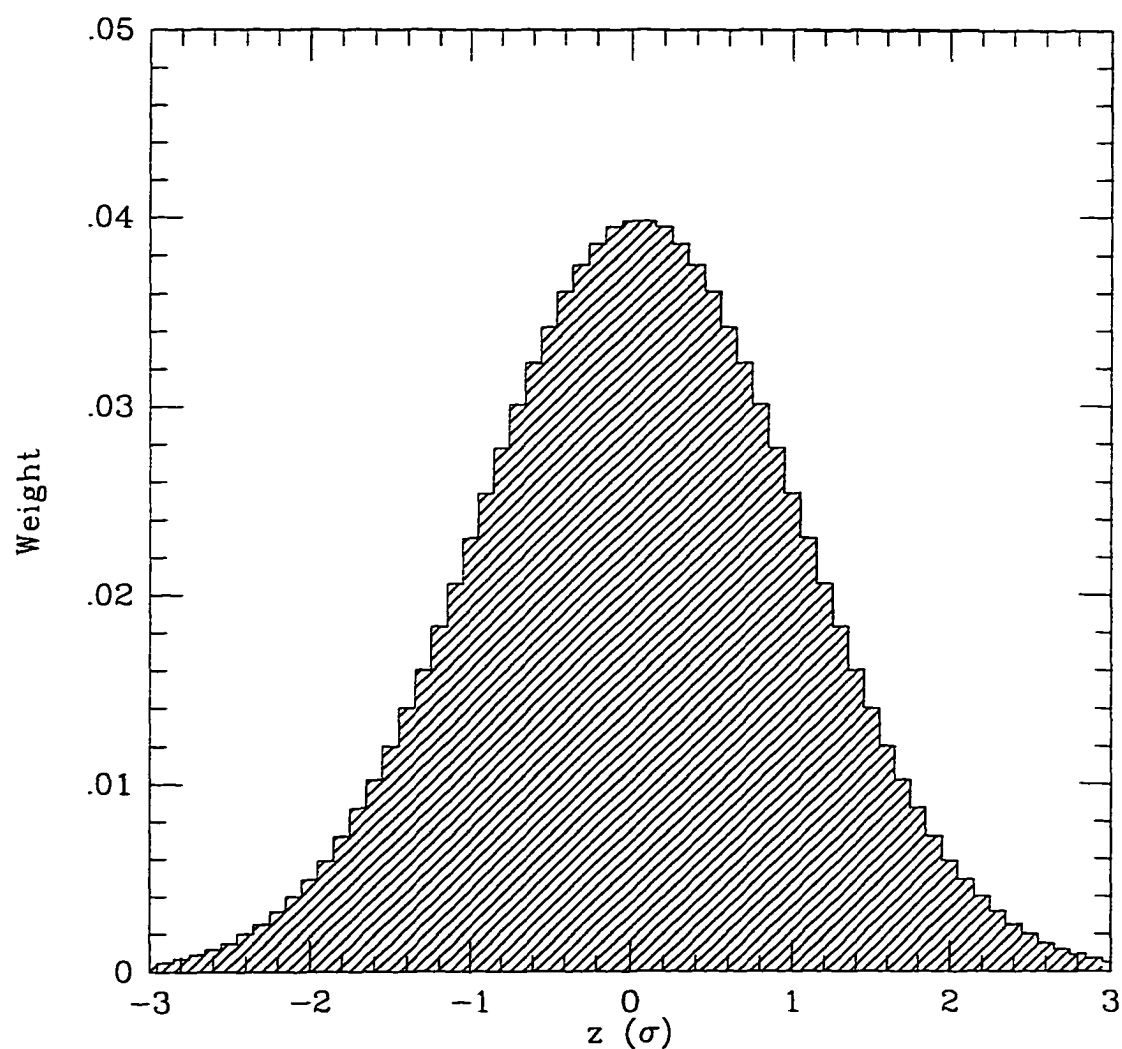


Figure 5.1 Distribution of weights as a function of σ_z for galaxies with photometrically determined redshifts. Each galaxy is treated as a distribution centered on its estimated redshift but distributed over $\pm 3\sigma$.

We also attempt to correct for incompleteness in our LF based on our analysis shown in Figure 2.15. For each point source in the survey, the level of incompleteness is determined depending on the point source-to-total luminosity ratio of the object. This factor is then multiplied with $1/V_a$ for each object in the survey so that the final LF reflects the incompleteness correction.

5.1.2. Comparison with the Local Luminosity Function for Seyferts

Figure 5.2 is the luminosity function for nuclei having colors consistent with Seyferts. Here we have plotted $\log(\phi)$ in units of $\# \text{ Mpc}^{-3} \text{ mag}^{-1}$ vs. the absolute B magnitude. The apparent V magnitudes were used to determine B magnitudes from equation 5.4. Table 5.1 provides the data used to construct this figure, including the number of data points in each bin n and the number corrected for incompleteness $n_{corrected}$. The luminosity function shown is for point sources contributing $\geq 3\%$ of the total galaxy light. Figure 5.2 is the luminosity function with $H_0=100 \text{ km s}^{-1} \text{ Mpc}^{-1}$, $q_0=0.5$ and $\alpha=-1.0$. The solid line represents the LF at $0 < z \leq 0.4$ and the dashed line represents the LF at $0.4 < z \leq 0.8$. The mean redshift of the low z bin is $\langle z \rangle = 0.31$ and for the high z bin is $\langle z \rangle = 0.57$. We compare our LF with that of HB for Seyfert 1 and 2 galaxies from the CfA redshift survey (dot-dashed line).

We first investigate the overlapping region of our LFs with that of HB. We notice that in the region of $-18.5 \geq M_B \geq -20.5$, where the LFs overlap, that the number density appears to remain constant between our LFs and theirs. Our LFs appear to be in good agreement with that of HB and maintain the same shape within the overlapping magnitude bins. In support of the number density of AGNs observed in this luminosity range, we note the X-ray findings for LLAGNs as compared with that of HB. The *Einstein* Extended Medium Sensitivity Survey

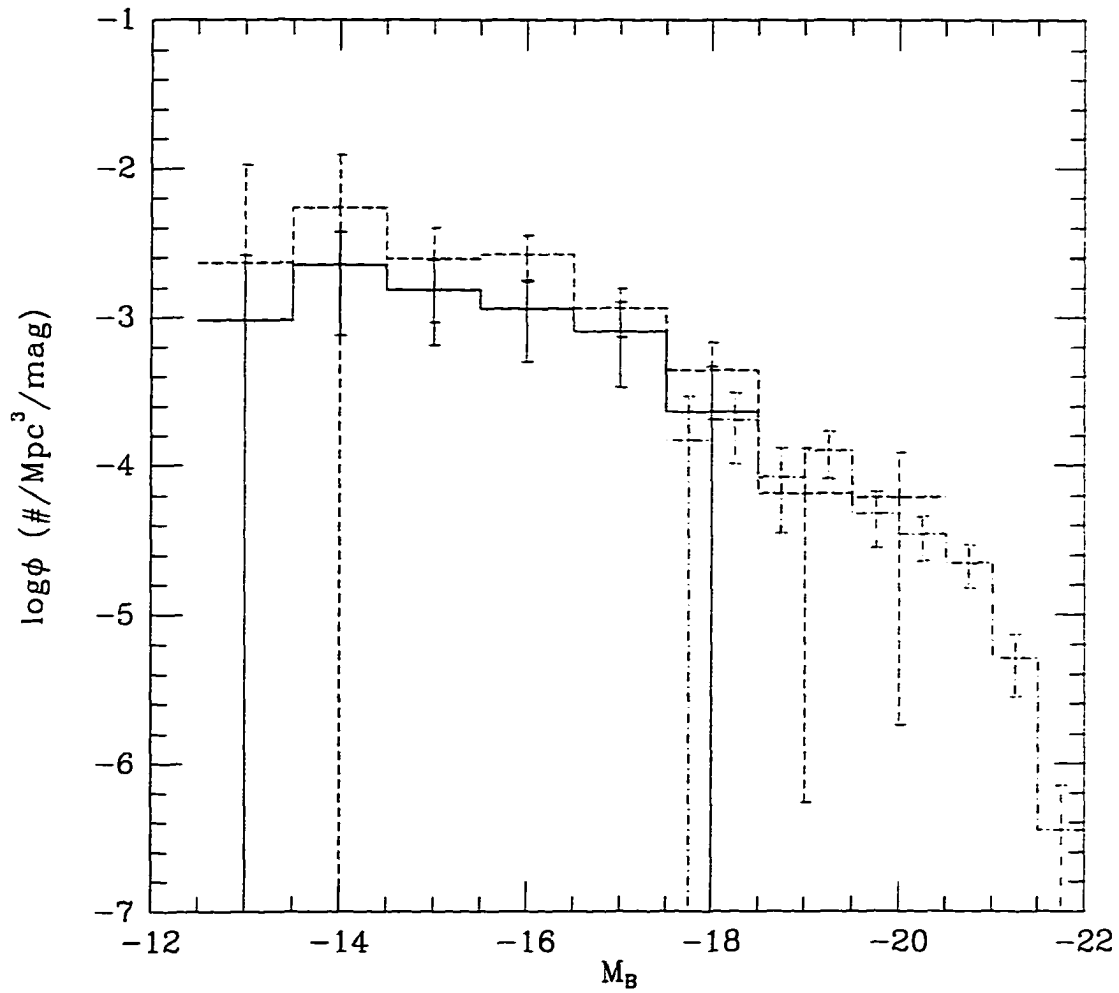


Figure 5.2 The luminosity function of compact nuclei $\geq 3\%$ of the total galaxy light. The solid line represents the LF for nuclei at $0 < z \leq 0.4$ and the dashed line is the LF at $0.4 < z \leq 0.8$. The dot-dashed line is the LF for Seyfert galaxies from the CfA redshift survey (Huchra & Burg 1992). Here we have assumed $H_0 = 100 \text{ km s}^{-1} \text{ Mpc}^{-1}$, $q_0 = 0.5$ and $\alpha = -1.0$.

(EMSS) provides an X-ray selected sample of LLAGN for which the optical luminosity function has been derived (Della Ceca et al. 1996). They used 226 broad-line AGN from this survey with measured redshifts and V magnitudes. Their LF extends to the same limiting absolute magnitude as that of HB and they find good agreement with their number density for broad-line AGNs. Here we have compared the present data with the HB LF for both Seyfert 1 and 2 type galaxies. Although the EMSS result is only for Seyfert 1 galaxies, it confirms the number density of broad line LLAGNs locally through a different selection method supporting the HB number density at faint absolute magnitudes.

To provide a more careful check on the possibility of increase or decrease between our LFs and that of HB within their overlapping luminosity range, we consider the number density of nuclei in our sample which are similar to the Seyfert nuclei of HB. Granato et al. (1993) have shown that Seyfert nuclei from the CfA survey and other Markarian Seyferts have nuclei which contribute 20% to 100% of the total galaxy light. If we limit our LF to include only our nuclei that comprise more than 20% of the galaxy light, and are therefore more like those objects included in the HB study, we find the number density to decrease by a factor of 1.25 from that shown in Figure 5.2 for LF points at $M_B = -19$ and -20 . This amount of decrease is still consistent with our number density being the same as that of HB in these luminosity bins. We can further attempt to improve the comparison by correcting for possible incompleteness in the HB data due to the observed axis ratio bias of their sample illustrated in Maiolino & Rieke (1995). Accordingly, the HB data may be incomplete by a factor of 2. Correcting their LF for this level of incompleteness and comparing with our corrected LF, the number densities at $M_B = -19$ and -20 remain the same within the errors and are consistent with no change in the number density of LLAGN over this luminosity range. A

statistical test is done by computing the density weighted $1/V_a'$ number density (discussed in the following paragraph) for our nuclei in the overlapping luminosity bins and determining if the amount of density increase is statistically significant when compared to the HB number density in the same luminosity range. This test reveals that the two datasets are consistent with no density evolution within the errors.

Focusing now on the faint end of our LFs we notice that our upper limit luminosity functions for LLAGNs appear to flatten in both the high and low redshift bins at $M_B \geq -16$. The implication of this observed flattening with regard to quasar evolution models is discussed in detail later in this chapter. We also examine the difference in number density between our LFs at the faint end. There does not appear to be evidence for a significant increase in number density between our high redshift LF and the low redshift LF within the Poisson errors. However, the high redshift LF consistently lies above the low redshift LF. This is most obvious at $M_B \geq -18$. To determine if the density increase is statistically significant, we use the $\langle V'/V_a' \rangle$ method where V_a' is the density weighted accessible volume (Schmidt & Green 1983). Since our LFs are nearly parallel, we assume luminosity independent density evolution of the form $\rho(z) = (1+z)^\beta$. The mean value of V'/V_a' is

$$\langle V'/V_a' \rangle = 0.5 \pm (12n)^{-1/2} \quad (5.7)$$

for objects distributed according to the assumed density equation. We begin our test by assuming no density evolution ($\beta=0$) which yields $\langle V'/V_a' \rangle = 0.602 \pm 0.043$. We then increase β until $\langle V'/V_a' \rangle = 0.5 \pm 0.043$. This equality is reached at $\beta=1.9$, which represents the least amount of statistically significant density evolution to describe our data at $z \leq 0.8$.

Because our data represent upper limits of the AGN LF, this apparent increase in number density at the faint end should be carefully interpreted. If our selection technique systematically includes more objects at high redshift than at low redshift, the increase may not be real. However, we have shown that the unresolved region of HST increases slowly with redshift, varying only by 250 parsecs in diameter ($H_0=75$) over the range $0.2 \lesssim z \lesssim 0.8$. One would need a significant population of galactic nuclear objects having actual sizes between 300 and 550 pc in diameter so that they would appear unresolved in the higher redshift bin but appear resolved and therefore not included in the low redshift bin. We examine the likelihood of this possibility by investigating the bulge population in spiral galaxies in our survey. Figure 5.3 shows the bulge diameter in parsecs based on the bulge half-light radius for spiral galaxies in our survey with spectroscopic redshifts (filled circles) and for galaxies with photometric redshifts (open circles). The solid line is the resolving limit of HST assuming $H_0=75$ km/s/Mpc. This diagram shows that the number of bulges does not appear to increase at small diameters. We would expect that if bulges exist in our survey below the HST resolving limit, their number density would decrease towards zero as they approach zero diameter.

A test can be performed to determine if the increased number density observed for our unresolved nuclei could be due to a population of nuclear objects which appear unresolved at high z while remaining resolved at low z . Based on the bulge distribution shown in Figure 5.3, we simply count the number of bulges that would appear unresolved if the number density of bulges in our survey remained constant down to bulge diameters of zero. In this way, we assume an upper limit number density for the small bulge population. We compare the number of bulges which would be observed in the lower redshift half of the survey as compared to the upper redshift half where we divide equally the volume of space. Equal volumes of space

are measured between $0 \leq z \leq 0.447$ and $0.447 \leq z \leq 0.8$. In this experiment, we find that the number of unresolved bulges would remain constant within the Poisson errors between the two redshift bins of equal volume. We find that the number of nuclear point sources in our survey increases by a factor of 1.65 between the low redshift and the high redshift bins which is a statistically significant number density increase within the Poisson errors. This simple test indicates that the observed increase in number density could not be due to unresolved bulge-like objects in our survey.

Another test of the number density increase is conducted by performing the $\langle V'/V_a \rangle$ calculation over a smaller range in redshift. By limiting the redshift range, we reduce any effect on the observed number density evolution caused by marginally resolved nuclear objects becoming unresolved and adding to the number density at higher z . If we limit ourselves to performing this calculation for objects observed out to $z=0.4$, we find that the least amount of density evolution necessary to describe the observations is consistent with that required to describe the data out to $z=0.8$.

For the reasons we have outlined here, we interpret the increase in number density as resulting from an actual increase in the population of LLAGNS and nuclear starburst regions at $-18 \leq M_B \leq -14$. This observation poses the following question: if we observe an increase in number density at the faint end of our LF ($M_B \leq -18$) but no increase at $M_B = -19$ to -20 as compared with HB, what are the implications for the global evolution of active nuclei? One explanation is that the population mix at the faint end is different from that at the bright end. Where we overlap with the LF of HB, our nuclei are likely to be more like the traditional Seyfert 1 galaxies. This is supported by the spectroscopic identifications of our two

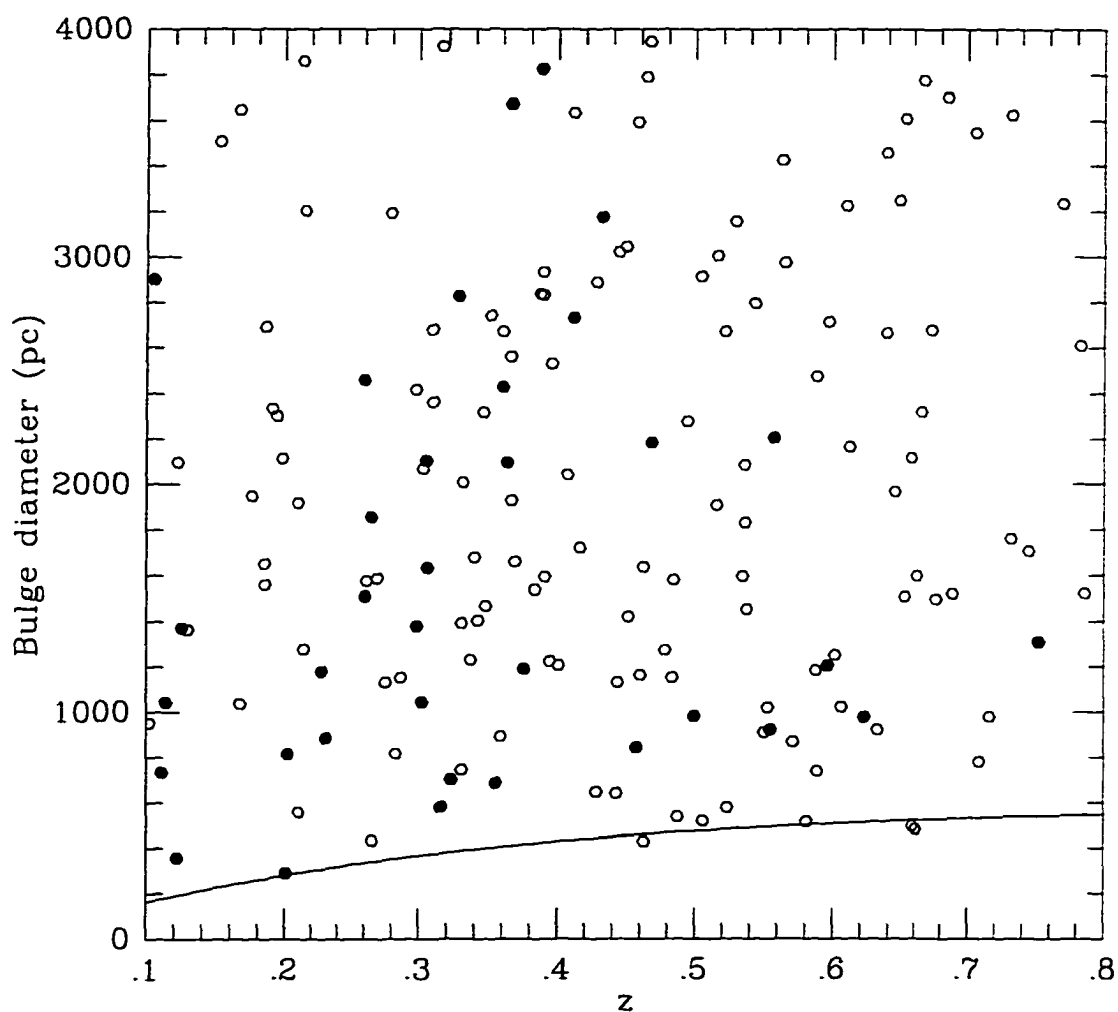


Figure 5.3 The bulge diameter in parsecs based on the bulge half-light radius for spiral galaxies in our survey with spectroscopic redshifts (filled circles) and photometric redshifts (open circles). The solid line is the resolving limit of HST assuming $H_0=75$ km/s/Mpc.

brightest nuclei. However, as we look at less luminous nuclei, we are probing a mix of fainter Seyfert 2s and LINERS. This population reveals an increase in number density with redshift out to $z \simeq 0.8$ whereas the brighter Seyfert 1 nuclei do not show any number density evolution out to this redshift. In the following section, we discuss further the implications of this scenario for comparing our observations with the intrinsically brighter QSO LFs.

5.1.3. Comparison with QSO Luminosity Functions

Figure 5.4 is the luminosity function with $H_0 = 50 \text{ km s}^{-1} \text{ Mpc}^{-1}$, $q_0 = 0.5$ and $\alpha = -0.5$. Again, the solid line represents the LF from $0 < z \leq 0.4$ and the dashed line is for $0.4 < z \leq 0.8$. Here we compare with the LF for QSO's from the compilation by Hartwick and Schade (1990) for QSO's having $0.16 < z \leq 0.4$ (solid line at higher luminosities) and $0.4 < z \leq 0.7$ (dashed line at higher luminosities). These redshift bins are roughly comparable to ours. Table 5.2 provides the data used to construct these LFs.

This figure is useful for studying how the LF at fainter magnitudes compares with the bright end and allows us to investigate the nature of the luminosity function evolution. There is some indication in this figure that the shape of the LF changes between the low and high redshift bins when we consider both the low (this study) and high (Hartwick & Schade) luminosity points. If we assume that our upper limit LFs represent LLAGNs which are of the same nature as the brighter QSOs, any change in the overall shape of the LF would argue against both pure density evolution and pure luminosity evolution for these objects. Pure density evolution of the quasar LF has been ruled out by results from a large number of quasar surveys (e.g. Cheney & Rowan-Robinson 1981). In pure density evolution, the past LF is the same in shape as the local LF but shifted to higher densities.

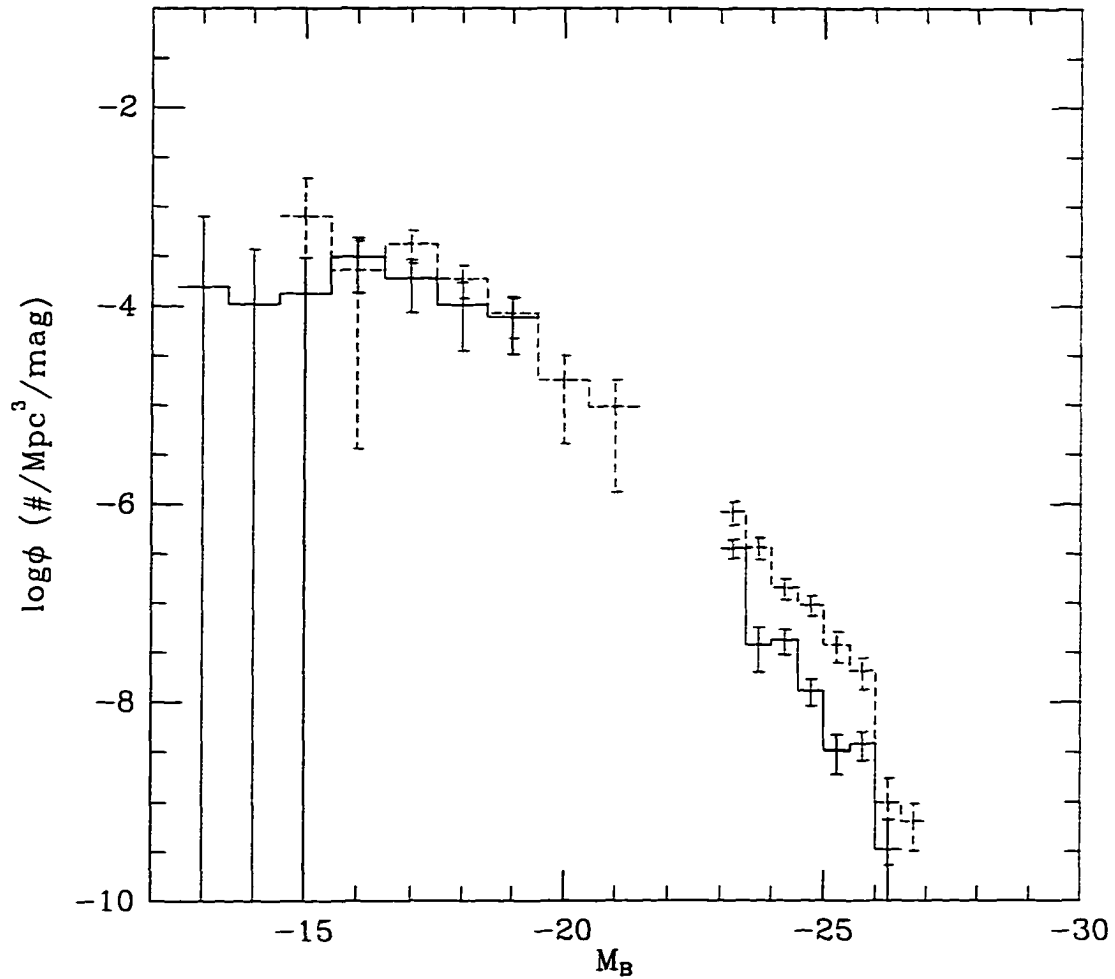


Figure 5.4 The luminosity function of compact nuclei $\geq 3\%$ of the total galaxy light. The solid line represents nuclei at $0 < z \leq 0.4$ and the dashed line is for $0.4 < z \leq 0.8$. At higher luminosities we show the LF for QSO's from the compilation by Hartwick and Schade (1990) for $0.16 < z \leq 0.4$ (solid line at $M_B \leq -22$) and $0.4 < z \leq 0.7$ (dashed line at $M_B \leq -22$). Here we have assumed $H_0 = 50 \text{ km s}^{-1} \text{ Mpc}^{-1}$, $q_0 = 0.5$ and $\alpha = -0.5$.

An overview of quasar evolution models can be found in Koo (1986). In pure luminosity evolution, a uniform shift to brighter luminosities is observed while the LF shape is preserved. Under these assumptions, the combined LFs in Figure 5.4 do not appear to favor either of these scenarios although we examine this question further below.

There have been many analytical representations for the shape of the quasar LF proposed in the literature. The double power-law model of Boyle et al. (1988) is well-constrained and has been successful at $z \lesssim 2.2$. This model can be written as

$$\phi(L, z) = \frac{\phi_*/L_z}{(L/L_z)^{\beta_l} + (L/L_z)^{\beta_h}} \quad (5.8)$$

where the redshift dependence, L_z , is

$$L_z = L_*(1+z)^{-(1+\alpha)} \exp[-(z-z_*)^2/2\sigma_*^2] \quad (5.9)$$

as in Pei (1995) where pure-luminosity evolution is assumed and α is the spectral index. In equation 5.8 β_l is the power-law index for the faint end while β_h represents the bright end. To better compare our LF with the brighter quasar LF from Harwick & Schade, we extrapolate this model, fitted to their data, to lower luminosities.

Figure 5.5a shows the LFs from Figure 5.4 with the double power-law model fit to the high luminosity data shown as the dotted line. The fitted parameters from Pei (1995) are $\beta_l = 1.64 \pm 0.18$, $\beta_h = 3.52 \pm 0.11$, $z_* = 2.75 \pm 0.05$, $\sigma_* = 0.93 \pm 0.03$, $\log(L_*/L_\odot) = 13.03 \pm 0.10$, and $\log(\phi_*/\text{Mpc}^3) = -6.05 \pm 0.15$. These parameters are the best fit to the Harwick & Schade LFs at various redshift bins. Here we have calculated the model at the median redshift for each of the two redshift bins to overlay with the LFs. Although the fit to the high luminosity LFs is very good, this model does not fit our LFs at lower luminosities. The model predicts lower number

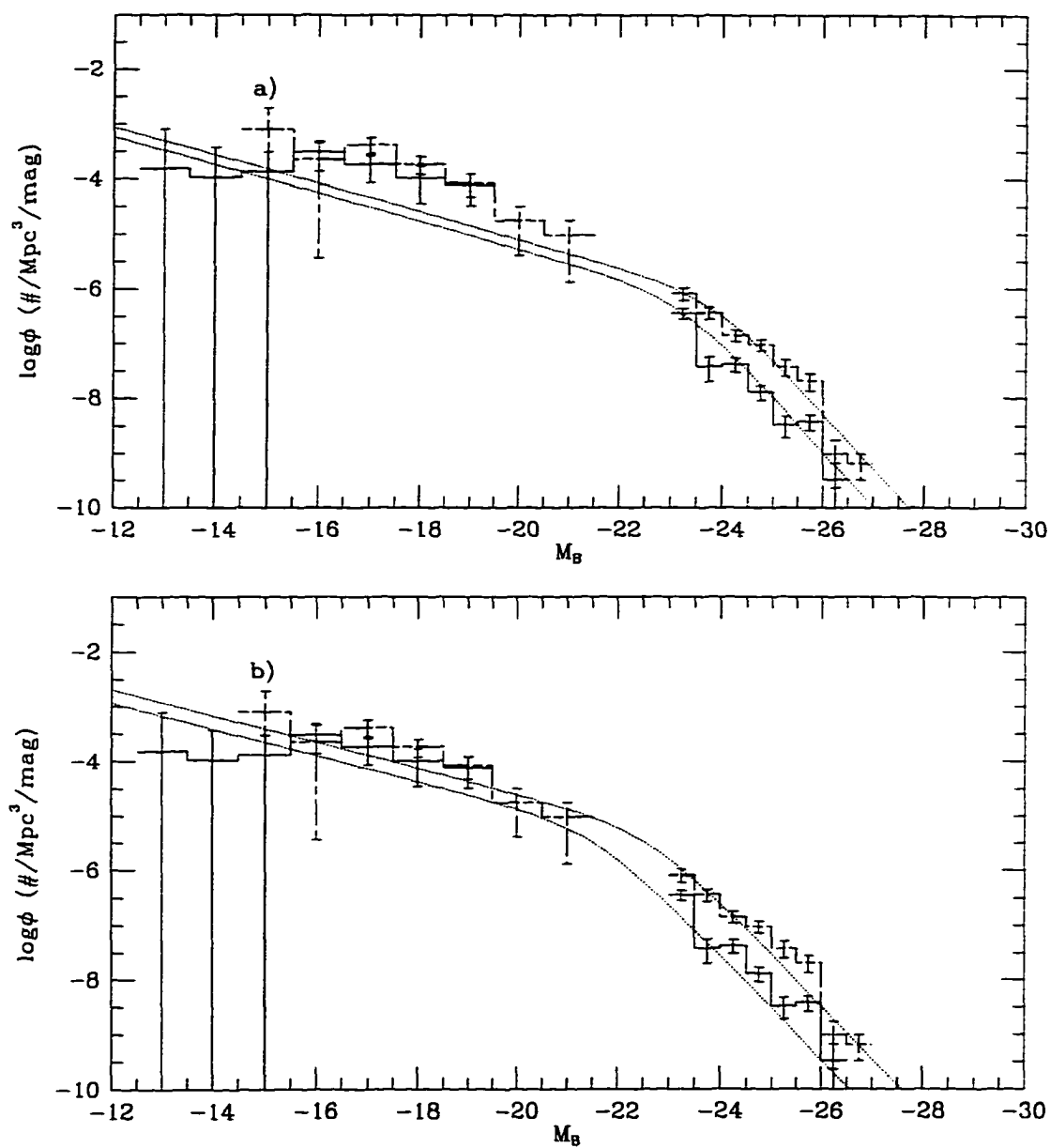


Figure 5.5 a) The double power-law model fitted to the bright quasar LFs (dotted line) using parameters from Pei (1995). b) The same model fitted to both the bright LF and the faint LF (this data). We assume $H_0=50 \text{ km s}^{-1} \text{ Mpc}^{-1}$, $q_0=0.5$ and $\alpha=-0.5$.

counts than our observations in the low redshift bin at $-19 \leq M_B \leq -16$ and in the high redshift bin at $-19 \leq M_B \leq -17$. We also note that the model predicts lower number counts than that observed by HB as inferred from the agreement in Figure 5.2 between their LF and our data over the common absolute magnitude range.

Because our luminosity function is only an upper limit on the AGN LF at moderate redshifts, it is not necessarily in disagreement with the extrapolated number counts of the model fits. As described previously, even if we assume that the nuclei in our survey are non-thermal in nature, our LF is likely to include an increased population of low-luminosity AGNs such as LINERS and faint Seyfert 2 nuclei. The extrapolated results of this model using the fitted parameters described above may be consistent with the population of faint QSOs and Seyfert 1 galaxies but may underestimate the total number of AGN including Seyfert 2s and LINERS at $M_B \geq -22$.

In Figure 5.5b we show the same LFs with the double power-law model fitted to both sets of data using χ^2 minimization. The fitted parameters are $\beta_l=1.6$, $\beta_h=3.4$, $\log(L_*/L_\odot)=12.5$ and $\log(\phi_*/\text{Mpc}^3)=-5.2$ holding z_* and σ constant at the fitted values of Pei. The flattening of the LF in the faint data is not well fit by this model. The χ^2 of the fit to this combined data set indicates a worse fit than that obtained for the bright quasar data alone in several redshift bins. We notice that the largest change in the fitted parameters occurs in the normalization and inflection point of the double power-law model and not in the slopes. Our two brightest LF bins, which are consistent with the HB local LF, largely influence the fit in this manner. If the two data sets being combined here are actually representing the same type of active nucleus, this result indicates that the double power-law model assuming pure luminosity evolution is not the best representation

of the data. The transition region between the low and high luminosity data appears to require a model with additional variables for adequate fitting of this portion of the LF.

This result leads to the following question: without considering the bright quasar data from Harwick & Schade, how well does pure luminosity evolution (PLE) model our faint LF over the redshift range to $z=0.8$? We fit a simple power-law to our low and high redshift LFs and determine the amount of PLE necessary to adequately model the data.

A power-law is fit to both the high and low redshift LFs from $-18 \lesssim M_B \lesssim -14$ of the form

$$\log\phi(z) = \text{const} + \gamma M(z) \quad (5.10)$$

where γ is the slope of the $\log\phi$ - M relation and is found to be 0.079 ± 0.066 . We find the mean increase in $\log\phi$ over this magnitude range is 0.4. This $\Delta\log\phi$ divided by γ gives the change in magnitude, $\Delta M = 5.1^{+25.7}_{-2.3}$. For pure luminosity evolution

$$\Delta M = 2.5\delta \log((1 + z_{\text{high}})/(1 + z_{\text{low}})) \quad (5.11)$$

Here, δ is the amount of PLE necessary to account for the observed density increase in a power-law parameterization in $(1+z)$. Using the mean z for each of our LF bins, we determine $\delta = 25.8^{+130.1}_{-11.6}$. This simple calculation shows that the amount of PLE necessary to account for the observed density increase is unreasonably large and unlikely to explain the observations.

The fact that our LF is only an upper limit probably does little to remedy the flatness of the faint end of the AGN LF. Any population of objects which may be included in our survey, such as intermediate aged starburst nuclei or minor merger remnants, is likely to have a luminosity function with a negative slope at the faint

end similar to that observed in the normal galaxy LF. If this is the case, subtracting an LF of this shape from our upper limit would result in further flattening of the faint end of the AGN LF.

5.2. The Number of LLAGN in Local Spiral Galaxies

In this section we address the implications the observed number density of compact nuclei in our survey has for the lifetimes of LLAGN and the fraction of present-day spiral galaxies that may host AGN of low luminosities. We first make the assumption that the observed number density increase with redshift is caused by the evolution of LLAGNs. As we will describe further in the following section, we assume a Gaussian density evolution equation for these objects consistent with the observed mild density evolution to $z=0.8$ but turning over at $z=2.3$ (see equation 5.16). At their peak density at $z=2.3$, the total number of unresolved nuclei is $5.9 \times 10^{-3} \text{ Mpc}^{-3} \text{ mag}^{-1}$ with $H_0=100 \text{ km s}^{-1} \text{ Mpc}^{-1}$. If our sample consists entirely of LLAGNs, what fraction of present-day galaxies are likely to have contained an LLAGN at some point in their lives? Typically our nuclei are found in spiral galaxies with absolute magnitudes in the range $-20.5 \leq M_B \leq -18.5$. Using the LF of Marzke et al. (1994) for spiral galaxies, the number of local spirals in this absolute magnitude range is 9×10^{-3} per Mpc^3 . This result implies that almost all present-day spiral galaxies contain LLAGN with absolute magnitudes of $M_B \simeq -16$, some of which may now be dormant. The total number density at $z=1.0$, which requires less extrapolation of our observations, indicates that $\sim 40\%$ of present-day spiral galaxies contain LLAGN in this magnitude range. If we assume the observed luminosity of these objects is due to disk accretion onto a black hole, we can determine if the amount of matter necessary to fuel an AGN of

this luminosity over a Hubble time is plausible. We convert the absolute magnitude to bolometric luminosity based on $L_{bol}/L_B = 11.8 \pm 4.3$ for quasars from Elvis et al. (1994). An order of magnitude approximation for the implied \dot{M} is given by

$$\dot{M} \sim L_{bol}(10^{-9} M_{\odot}/yr)/(10^{37} ergs/s) \quad (5.12)$$

from Shapiro & Teukolsky (1983). For nuclei with $M_B = -16$, $\dot{M} = 1.6 \times 10^{27}$ kg/yr. After 15 Gyr, the object accretes $\sim 10^7 M_{\odot}$, comparable to the mass of the black hole, which is a reasonable amount of matter for accretion. This result has interesting implications on the search for AGN in local galaxy nuclei.

5.3. Implications For the X-Ray Source Surface Density

Quasars have long been known as strong X-ray emitters and statistically significant samples have been selected through X-ray surveys (e.g. Giacconi et al. 1979). How quasars and their low-luminosity counterparts contribute to the diffuse X-ray background has been a question of interest for some time. In particular, low-luminosity AGNs are considered good candidates for explaining the origin of the soft X-ray background (0.2 - 4.0 keV).

Schmidt and Green (1986) derived the contribution of LLAGNs ($M_B > -23$) to be 29% of the observed background at 2 keV assuming no evolution in the number density. They note that any substantial evolution would dramatically increase this value. Other studies indicate that 30% to 90% of the background at 2 keV originates from AGNs (Boyle et al 1993) but with the brightest AGN making up 30%. Could the rest of the soft background be comprised of LLAGN?

We calculate the likely contribution of the compact nuclei in our survey to the X-ray background based on assumptions about the X-ray nature of the nuclei. Let

us assume that the X-ray flux of our nuclei is most like that for fainter AGN such as Seyfert 2s and LINERS. From the *Einstein Observatory* Imaging Proportional Counter (IPC), soft X-ray spectra for 22 Seyfert 2s and some LINERS in the range of 0.2 to 4.0 keV have been obtained (Krupe et al. 1990) and the X-ray luminosity for these objects is $10^{42 \pm 0.72}$ erg s⁻¹. In order for these galaxies to be spectroscopically classified as Seyfert 2s or LINERS, the nucleus must contribute a large fraction of the total galaxy light. From the CfA redshift survey, we know that spectroscopically selected Seyferts have nuclei contributing between 20% and ~100% of the total galaxy light (Granato et al. 1993). Because our nuclei are roughly an order of magnitude fainter, we assume their X-ray flux is also an order of magnitude fainter and is likely to be closer to $1 \times 10^{41 \pm 0.72}$ erg s⁻¹.

We first assume that the LFs we observe consist entirely of LLAGN and that the mild evolution in the number density observed for these objects over the absolute magnitude range $-18 \lesssim M_B \lesssim -14$ represents evolution in the LLAGN number density with redshift. Since the LF is relatively parallel over this magnitude range in both redshift bins, we allow the number density to be independent of luminosity for these objects where

$$\log \phi = 1.9 \log(z + 1) - 4.09 \quad (5.13)$$

for $H_0 = 50$ km s⁻¹ Mpc⁻¹, $q_0 = 0.5$ and $\alpha = -0.5$ and where ϕ is in units of Mpc⁻³ mag⁻¹.

To determine the total X-ray flux for these objects, we integrate the number density $\phi(z)$ multiplied by the X-ray flux out to z_{max} .

$$I_{Tot} = \int_0^{z_{max}} \phi(z) \frac{L_x}{4\pi A^2(z)} \frac{dV}{dz} dz \quad (5.14)$$

where I_{Tot} is the total X-ray flux from the point source nuclei. The volume element

is defined in Avni (1978) as

$$dV/dz = \omega(c/H_o)A^2(z)(1+z)^{-3}(1+2q_0z)^{-0.5} \quad (5.15)$$

We assume a Gaussian form for the number density evolution consistent with the mild evolution observed out to $z=0.8$ (equation 5.13) but reaching a maximum near $z=2.3$, the apparent peak in the quasar number density from Schmidt, Schneider & Gunn (1991).

$$\phi(z) = 1.03 \times 10^{-3}(1+z)^{-0.5} \exp(-(z-2.3)^2/2) \quad (5.16)$$

in units of $\text{Mpc}^{-3} \text{ mag}^{-1}$. The integration out to $z_{\text{max}}=4.0$ over 4 magnitude bins ($-18 \leq M_B \leq -14$) yields a total X-ray flux of $10^{-8.84 \pm 0.72} \text{ ergs s}^{-1} \text{ cm}^{-2} \text{ sr}^{-1}$ for the 0.2 - 4.0 keV range.

A recent measurement of the X-ray background using ROSAT (Chen, Fabian & Gendreau 1997) found an intensity of $1.46 \times 10^{-8} \text{ ergs s}^{-1} \text{ cm}^{-2} \text{ sr}^{-1}$ in the 1 - 2 keV range. Hasinger et al. (1993) find an X-ray background intensity of $1.25 \times 10^{-8} \text{ ergs s}^{-1} \text{ cm}^{-2} \text{ sr}^{-1}$ for this energy range. To convert between the measured energy ranges for comparison, we assume a power-law X-ray spectral index of $\alpha_x = -0.5$ based on *Einstein Observatory* IPC observations of low luminosity AGNs consisting primarily of Seyfert 2s and LINERS (Krupe et al. 1990). The conversion factor from the 0.2 - 4.0 keV to the 1 - 2 keV range is 0.267. Assuming an X-ray background intensity of 1.36×10^{-8} for 1 - 2 keV (an average of the two measured values), our nuclei between $-18 \leq M_B \leq -14$ contribute $3^{+12}_{-2}\%$ of the X-ray background.

We also calculate the contribution of these nuclei to the X-ray background using an optical-to-X-ray flux conversion from ROSAT. Based on 283 AGN from the ROSAT All-Sky Survey (Bade et al. 1995), the median $\log(f_x/f_B)$ is 0.55 with

a range of $\sim\pm 1$. The ROSAT energy range is 0.1 - 2.4 keV. We convert our M_B magnitude to X-ray luminosity using this ratio and sum the total X-ray luminosity per absolute magnitude bin over the range $-18 \leq M_B \leq -14$. This total L_x is then used in the integral in equation 5.14 to determine the total X-ray intensity for the nuclei in our sample. Using this conversion, we find the X-ray intensity of our nuclei to be $10^{-7.91 \pm 1}$ ergs s $^{-1}$ cm $^{-2}$ sr $^{-1}$. This corresponds to a mean contribution of 30% of the X-ray background intensity at 1 - 2 keV although the uncertainty in the optical-to-X-ray flux allows for the total X-ray intensity to exceed the soft X-ray background.

Because we do not have actual X-ray flux measurements for the galaxies in our sample, these estimates of their contribution to the soft X-ray background are based on assumptions about the X-ray nature of these objects. Although we cannot say with certainty what their true contribution is, these results suggest that LLAGN may contribute a significant portion of the soft X-ray background if the X-ray-to-optical flux scales accordingly at faint optical magnitudes. Further study of the X-ray properties of faint AGN would provide tighter constraints on their likely contribution to the diffuse X-ray background.

Table 5.1. Luminosity Functions ($H_o=100$, $q_o=0.5$ and $\alpha=-1.0$)

M_B	ϕ	n	$n_{corrected}$	ϕ	n	$n_{corrected}$
	$0 < z \leq 0.4$			$0.4 < z \leq 0.8$		
-13.0	-3.02	0.33	1.20	-2.64	0.08	0.31
-14.0	-2.65	2.26	6.13	-2.26	0.63	2.44
-15.0	-2.81	3.01	9.92	-2.61	2.58	7.51
-16.0	-2.94	3.17	9.10	-2.58	8.79	21.43
-17.0	-3.09	2.96	6.55	-2.94	7.63	17.22
-18.0	-3.64	0.99	1.90	-3.35	3.50	5.46
-19.0				-4.18	1.02	1.54
-20.0				-4.21	1.06	1.61

Table 5.2. Luminosity Functions ($H_o=50$, $q_o=0.5$ and $\alpha=-0.5$)

M_B	ϕ	n	$n_{corrected}$	ϕ	n	$n_{corrected}$
	$0 < z \leq 0.4$			$0.4 < z \leq 0.8$		
-13.0	-3.81	0.06	0.21			
-14.0	-3.98	0.16	0.58			
-15.0	-3.87	0.64	2.27	-3.10	0.50	1.94
-16.0	-3.51	3.23	9.40	-3.64	1.03	3.68
-17.0	-3.73	3.47	11.12	-3.38	7.55	19.76
-18.0	-3.99	2.33	6.65	-3.73	7.93	18.87
-19.0	-4.11	2.97	5.02	-4.07	5.24	8.69
-20.0				-4.75	1.68	2.55
-21.0				-5.02	1.34	2.04

CHAPTER 6

CONCLUSIONS

The main purpose of this study is to understand the space density and properties of active galaxies to $z \simeq 0.8$. We have investigated the frequency and nature of unresolved nuclei in galaxies at moderate redshift as indicators of nuclear activity such as AGN or starbursts. Below we summarize the main results and conclusions from this study. We also discuss future projects to be carried out based on this survey data which will help to answer additional questions about the nature of these objects.

6.1. Summary of Results

We have morphologically selected compact nuclei galaxies from HST WFPC2 V (F606W) and I(F814W) images based on maximum likelihood fitting of the galaxy light profile to identify all major components of the galaxy; exponential disk, $r^{-1/4}$ bulge, and nuclear point source. Incompleteness levels for this type of selection have been determined based on Monte-Carlo simulations of the fitting procedure using real galaxies with superimposed nuclear components. We detected 101

galaxies containing unresolved nuclear components comprising $\geq 1\%$ of the total galaxy light. In our survey of 1033 galaxies at $I \lesssim 21.5$, the fraction containing an unresolved nuclear component greater than 3% of the total galaxy light is $16 \pm 3\%$ corrected for incompleteness. The fraction of galaxies containing an unresolved nuclear component greater than 5% of the total galaxy light is $9 \pm 1\%$.

To determine the number density of the compact nuclei galaxies we must know the redshifts of the galaxies in our sample. Spectroscopic redshifts were obtained at the Kitt Peak 4-meter telescope for 29 of these galaxies with 6 additional redshifts taken from the literature for galaxies in the Groth Survey Strip and HDF. A few of the galaxies in the sample contain nuclei comprising ~ 30 to 50% of the galaxy light and displayed spectral features indicative of Seyfert 1 and 2 AGN. Most of the galaxies, however, contain nuclei comprising less than 20% of the galaxy light. Therefore the spectra display spectral features of the host galaxy and cannot be used to classify the nucleus. Redshifts were photometrically estimated for the remainder of our sample based upon a large database of MDS galaxies for which redshifts, magnitudes, and V-I colors were known. Empirical relationships among these characteristics allow us to estimate redshifts for the host galaxies in our sample to accuracies of $\sigma_z = 0.1$ to $z = 0.8$.

The compact nuclei appear to favor host galaxies with bulges contributing less than 50% of the galaxy light. The majority of hosts have small bulges (less than 20% of the galaxy light) consistent with late-type spiral galaxies. The distribution of host galaxies is similar to that found by Ho et al. (1997a) for local dwarf Seyfert nuclei but is also consistent with that of local starbursting galaxies (Balzano 1983). If our sample consists of moderate redshift starburst and AGN, we detect no evidence of evolution of the dominant host galaxy types for these objects to $z \simeq 0.8$.

Compared to the entire sample of survey galaxies, the host galaxies of compact nuclei have smaller half-light radii. Very few of the large, faint galaxies in the survey contain compact nuclei. This may be a result of low surface brightness galaxies being stable against the growth of bar instabilities which may help fuel nuclear activity. Concerning the colors of the host galaxies, they are generally like those of other morphologically similar galaxies in the field with a slight tendency to be bluer. This result agrees with findings for local AGN host galaxies. We also note that compact nuclei avoid host galaxies with low disk axis ratios ($(b/a) \lesssim 0.4$) although to a much lesser degree than spectroscopically selected samples of Seyferts. This slight effect may be caused by obscuration in a flattened disk parallel to the plane of the host galaxy or by the main disk containing dust extending into the galaxy center.

We determine the absolute magnitude range of our host galaxies using the spectroscopic and photometric redshifts. The distribution peaks at $M_B \simeq -21.3$ with $H_0 = 50$ km/s/Mpc which is very similar to that for local Seyfert hosts. The distribution of absolute magnitudes for the hosts is similar to that for local LLAGN and HII nuclei hosts found by Ho et al. (1997a and 1997b).

The V-I colors of the nuclei can be used to help determine their nature by comparing them with the colors of Seyfert nuclei and other stellar populations of various ages. Using spectra from the literature, we calculated synthetic colors for typical Seyfert 1, 1.5 and 2 galaxies dominated by the nucleus as well as HII nuclei and intermediate aged stellar populations as proxies for possible starburst nuclei or minor merger remnants in our sample. Most of the nuclei have colors consistent with Seyfert nuclei and also consistent with intermediate aged star clusters. A small number have colors too blue to be Seyferts but are consistent with young or

intermediate aged star clusters and are likely to be starburst nuclei.

The subsample of our objects having colors consistent with those of Seyfert nucleus-dominated galaxies as well as intermediate aged starburst nuclei represents an upper limit estimate on the number density of AGN in our survey. This subsample is used to construct the upper limit luminosity function for faint AGN out to redshifts of $z \simeq 0.8$, providing the first look at the shape and parameters of the AGN LF in this luminosity and redshift regime. We find that our upper limit LF compares well with that for Seyferts in the CfA redshift survey (Huchra & Burg 1992) with no evidence for an increase in the number density over their common magnitude range. However, we detect a mild increase in the number density of compact nuclei between our low ($\langle z \rangle = 0.31$) and high ($\langle z \rangle = 0.57$) redshift LFs of the form $\phi \propto (1+z)^{1.9}$ for nuclei at $-18 \lesssim M_B \lesssim -14$ ($H_0 = 50$ km/s/Mpc). The mild number density evolution at the faint end of our LFs could be the result of an increase in the fraction of Seyfert 2 nuclei at LINERS in this luminosity range.

Both the low and high redshift LFs for our data appear to flatten at $M_B \geq -16$. When compared with the bright quasar LFs from Harwick & Schade (1990), the overall shape of the LF appears to change from low to high redshift arguing against pure density and pure luminosity evolution if our LFs represent the intrinsically fainter counterparts of QSOs. However, this apparent change in shape may be caused in part by the possibility that our fainter LFs contain a greater fraction of Seyfert 2 nuclei and LINERS. The flatness of our LF at these faint magnitudes and the increase in number density is inconsistent with pure luminosity evolution within our observations. Additionally, we find the number density of our nuclei combined with the observed mild evolution indicates that almost all present-day spiral galaxies could host LLAGN either active or dormant.

We calculate the likely contribution of the compact nuclei in our survey to the X-ray background based on assumptions about the X-ray nature of the nuclei. Assuming the X-ray flux of our nuclei to be similar to that of Seyfert 2s and LINERS and that optical flux scales with X-ray flux, we estimate these nuclei in the range $-18 \leq M_B \leq -14$ can contribute up to 15% of the soft X-ray background at 1 to 2 keV. Using an X-ray-to-optical flux ratio for AGN from the ROSAT All-Sky Survey, these nuclei could contribute as little as a few percent of the soft X-ray background but the large uncertainty in the applied ratio would allow their total X-ray flux to exceed the soft X-ray background intensity. Further study of the X-ray properties of faint AGN is needed to provide tighter constraints on their likely contribution to the diffuse X-ray background.

6.2. Future Work

The results of this study provide the first look at the population of LLAGNs at moderate redshifts. Many additional questions can be studied with this dataset to understand better the processes that create and maintain nuclear activity in galaxies. In the cases of both AGN and starbursts, mechanisms are required within the host galaxy to provide fuel for the nuclear activity. Many such mechanisms have been proposed such as bars, galaxy-galaxy interactions, and other morphological disturbances. These types of disturbances have been well studied in local groups of galaxies giving only the current picture of how host galaxy morphology relates to nuclear activity. It is likely that some morphological disturbances, after initiating nuclear activity, become relaxed over time and are less easily observable. This could explain the lack of a bar/AGN connection and the small numbers of galaxy neighbors and interactions observed among local Seyferts. Studying a population

of active galaxies at earlier epochs will help us understand how such fueling mechanisms evolve on a global scale over several gigayears.

The residuals from our fitting algorithm can be quantitatively examined for evidence of bars, rings and other disk asymmetries which indicate a nuclear fueling mechanism. Of particular interest is the presence of bars at earlier epochs in galaxies having nuclear activity. The theoretical models of Friedli & Benz (1993) predict that once a bar has channeled enough of the galaxy's mass into the central few hundred parsecs of the galaxy, it will dissolve on approximately gigayear timescales. By determining the frequency of bars in AGN/starburst hosts to $z \simeq 0.8$, we can trace the global evolution of bars in initiating nuclear activity. If a higher frequency of bars is detected at high z while decreasing towards lower z , the typical duration of a bar in an active galaxy as well as the likely formation epoch can be estimated. This scenario is consistent with the lack of a bar/AGN connection observed locally (McLeod & Rieke 1995; Ho et al. 1996c). If the bar frequency remains constant with z , bars might be forming at a rate close to the rate at which they dissolve. Another globally interesting question can be answered by studying the control sample of field galaxies. Since many galaxies may have experienced episodes of rapid star formation, tracing the evolution of bars and other asymmetries in the control sample will help us understand when and how these perturbations have affected the general population of galaxies. We can also determine how the presence of a bar affects the AGN/starburst luminosity. Closely related to bars, galaxy rings can be studied as well. These might be indicators that a bar exists or recently existed within the galaxy (Shlosman et al. 1990).

Studying the incidence of close pairs and interactions among AGN/starburst host galaxies will also reveal information about how the fueling mechanisms of

active nuclei evolve. Gravitationally induced perturbations to normal galaxies may provide the initiative for active nucleus fueling. An increase in the number of hosts having nearby neighbor galaxies at moderate redshifts will indicate at what epoch gravitationally induced perturbations most efficiently initiated nuclear activity. It will also be possible to study the relationship between the mass or luminosity of the neighbor galaxy and the luminosity of the active nucleus. The limiting magnitude for detecting galaxies in most WFPC2 parallel images is ~ 2 magnitudes below that for the fitted galaxies. This allows us to search over a large range in magnitude for active galaxy neighbors so that faint as well as bright companions can be detected.

In order to more directly compare the results of this survey to local and moderate redshift spectroscopic surveys (e.g. Tresse et al. 1996; Ho et al. 1997a), the morphologies of these survey galaxies must be examined in the same way as our HST imaged galaxies. Such a study will bring to light the differences and biases in these survey techniques. High resolution ground-based images for a sample of local low-luminosity Seyfert galaxies would allow us to study the nuclear regions and determine the fraction in which the AGN can be morphologically detected. Likewise, HST images of many fields included in the CFHT spectroscopic survey are being obtained and will be available through the archive in less than a year. The fitting techniques described here can be applied to this data set to determine the number of galaxies containing morphological evidence of an AGN nucleus. The results of these studies will allow for a more direct comparison of the number density of local AGNs to more distant ones in this and the CFHT surveys.

REFERENCES

- Avni, Y. 1978 *A&A*, 63, L13
- Bade, N., Fink, H. H., Engels, D., Voges, W., Hagen, H.-J., Wisotzki, L. & Reimers, D. 1995, *A&AS*, 110, 469
- Balzano, V. A. 1983, *ApJ*, 268, 602
- Boroson, T. 1981, *ApJS*, 46, 177
- Boyle, B. J., Griffiths, R. E., Shanks, T., Stewart, G. C. & Georgantopoulos, I. 1993, *MNRAS*, 260, 49
- Boyle, B. J., Shanks, T. & Peterson, B. A. 1988, *MNRAS*, 235, 935
- Bruzual, A. G. & Charlot, S. 1993, *ApJ*, 405, 5
- Cohen, J. G., Cowie, L. L., Hogg, D. W., Songaila, A., Blandford, R., Hu, E. M. & Shopbell, P. 1996, *ApJ*, 471L, 5
- Chen, L.-W., Fabian, A. C. & Gendreau, K. C. 1997, *MNRAS*, 285, 449
- Cheng, F. Z., Danese, L., De Zotti, G. & Franchesini, A. 1985, *MNRAS*, 212, 857
- Cheney, J. E. & Rowan-Robinson, M. 1981, *MNRAS*, 195, 497
- Christensen, C. G. 1975, *AJ*, 80, 282
- Della Ceca, R., Zamorani, G., Maccacaro, T., Setti, G. & Wolter, A. 1996, *ApJ*, 465, 650
- DeVeney, J., Massey, P. & Sarajedini, V. 1994, 'Multi-Slits at Kitt Peak: A Manual for Designing and Using Entrance Masks for Low/Moderate-Resolution Spectroscopy', Kitt Peak National Observatory
- Elvis, M., Soltan A. & Keel, W. C. 1984, *ApJ* 283, 479
- Elvis, M., Wilkes, B. J., McDowell, J. C., Green, R. F., Bechtold, J., Willner, S. P., Oey, M. S., Polomski, E. & Cutri, R. 1994, *ApJS*, 95, 1.
- Friedli, D. & Benz, W. 1993, *A&A*, 268, 65
- Giacconi, R. et al. 1979, *ApJ*, 234, L1
- Granato, G. L., Zitelli, V., Bonoli, F., Danese, L., Bonoli, C. & Delpino, F. 1993, *ApJS*, 89, 35
- Griffiths, R. E. et al. 1994, *ApJ* 437, 67
- Gronwall, C. & Koo, D. C. 1995, *ApJ*, 440, L1
- Groth, E. J. et al. 1997, in preparation
- Hartwick, F. D. A. & Schade, D. 1990, *ARA&A*, 28, 437
- Hassinger, G., Burg, R., Giacconi, R., Hartner, G., Schmidt, M., Trumper, J. & Zamorani, G. 1993, *A&A*, 275, 1

- Hibbard, J. E., Guhathakurta, P., van Gorkom, J. H. & Schweizer, F. 1994, *AJ*, 107, 67
- Ho, L. C., Filippenko, A. & Sargent, W. L. W. 1997a, *ApJ*, in press
- Ho, L. C., Filippenko, A. & Sargent, W. L. W. 1997b, *ApJ*, in press
- Ho, L. C., Filippenko, A. & Sargent, W. L. W. 1997b, *ApJ*, in press
- Huchra, J. & Burg, R. 1992, *ApJ*, 393, 90
- Im, M., Griffiths, R. E., Ratnatunga, K. U. & Sarajedini, V. L. 1996, *ApJ*, 461L, 79
- Kalikov, M., Kuneva, I., Tsvetanov, Z. & Strigachev, A. 1993, *A&AS*, 98, 165
- Keel, W. C. 1980, *AJ*, 85, 198
- Kennicutt, R. C. 1992, *ApJS*, 79, 255
- Koo, D. C. 1986, in *Structure and Evolution of Galactic Nuclei*, eds. G. Guiricín et al., p. 317
- Koo, D. C. et al. 1996, *ApJ*, 469, 535
- Koratkar, A., Deustua, S. E., Heckman, T., Filippenko, A. V., Ho, L. C. & Rao, M. 1995, *ApJ* 440, 132
- Kotilainen, J. K. & Ward, M. J. 1994, *MNRAS*, 266, 953
- Kruper, J. S., Urry, C. M. & Canizares, C. R. 1990, *ApJS*, 74, 347
- Lauer, T. R., Ajhar, E. A., Byun, Y.-I., Dressler, A., Faber, S. M., Gillmair, C., Kormendy, J., Richstone, D. & Tremaine, S. 1995, *AJ*, 110, 2622
- Lawrence, A. & Elvis, M. 1982, *ApJ*, 256, 410
- Leitherer, C. et al. 1996, *PASP*, 108, 996
- Nelson, C. H., MacKenty, J. W., Simkin, S. M. & Griffiths, R. E. 1996, *ApJ*, 466, 713
- McArthur, B., Jefferys, W. & McCartney, J. 1994, *BAAS*, 18, 2804
- McLeod, K. K. & Rieke, G. H. 1995, *ApJ*, 441, 96
- Maiolino, R. & Rieke, G. H. 1995, *ApJ*, 454, 95
- Mihos, J. C., McGaugh, S. S. & de Blok, W. J. G. 1997 *ApJ*, 477, L79
- Mutz, S. B. et al. 1994, *ApJL* 434, L55
- Pei, Y. C. 1995, *ApJ*, 438, 623
- Ratnatunga, K. U., Griffiths, R. E. & Ostrander E. J. 1997, *ApJ*, in press
- Ratnatunga, K. U., Griffiths, R. E., Neuschaefer, L. W. & Ostrander E. J. 1995, in *Proc. HST Calibration Workshop II*, eds. A. Koratkar & C. Leitherer, p. 351-359

- Ratnatunga, K. U., Griffiths, R. E., Casertano, S., Neuschaefer, L. W. & Wyckoff, E. W. 1994, AJ, 108, 2362
- Ratnatunga, K. U. & Casertano, S. 1991, AJ, 101, 1075
- Schweizer, F. 1996, AJ, 111, 109
- Schmidt, M. & Green, R. F. 1983, ApJ, 269, 352
- Schmidt, M. & Green, R. F. 1986, ApJ, 305, 68
- Schmidt, M., Schneider D. P. & Gunn, J. E. 1991, in "The Space Distribution of Quasars", Proceedings of the Workshop, Victoria, Canada, ed. D. Crampton, p. 109
- Shlosman, I., Begelman, M. C. & Frank, J. 1990, Nature, 345, 679
- Shapiro, S. L. & Teukolsky, S. A. 1983, in "Black Holes, White Dwarfs, and Neutron Stars: The Physics of Compact Objects", John Wiley & Sons, Inc.
- Tresse, L., Rola, C., Hammer, F., Stasinska, G., Le Fevre, O., Lilly, S. J. & Crampton, D. 1996, MNRAS, 281, 847
- Veilleux, S. & Osterbrock, D. E. 1987, ApJS, 63, 295
- Weedman, D. W., Feldman, F. R., Balzano, V. A., Ramsey, L. W., Sramek, R. A. & Wu, C.-C. 1981, ApJ, 248, 105
- Williams, R. E. 1996, AJ, 112, 1335
- Yee, H. K. 1983, ApJ, 272, 473